Scholte Waves in Seabed Mapping

THESIS FOR THE DEGREE
MASTER OF SCIENCE

IN

MARINE MEASUREMENT SYSTEMS
ACOUSTICS

BY

ERIK LARSEN

DEPARTMENT OF PHYSICS AND TECHNOLOGY
UNIVERSITY OF BERGEN

DECEMBER 2020

Remember to look up at the stars and not down at your feet. Try to make sense of what you see and wonder about what makes the universe exist. Be curious. And however difficult life may seem, there is always something you can do and succeed at. It matters that you don't just give up.

- Prof. Stephen Hawking

Acknowledgment

The work presented in this thesis was done at University of Bergen, Faculty of Mathematics and Natural Sciences, Department of Physics and Technology, Norway. Most of the work was carried out in the period from January 2020 to end of December 2020.

I am very thankful to my supervisor, Prof. Per Lunde from Department of Physics and Technology, and co-supervisor, Prof. Tor Arne Johansen from Department of Earth Science, for accepting me as their master's student. I thank you both for invaluable help during the work, for introducing me to the physics behind acoustics and seismo-acoustics, for valuable knowledge, comments, criticism and support during this study. It has been a pleasure doing my very best to adopt your expertise in acoustics and seismo-acoustics.

I also want to thank Senior Engineer Bent Ole Ruud at the Department of Earth Science, for invaluable help and instructions when much urgent programming assistance, as well as theoretical understanding, was needed. I thank you especially for assisting me to understand the DEM, OASES and Seismic Unix packages. Additionally, I want to thank all friends I have got during my study at University of Bergen, especially my close friends from my Bachelor's degree in Nanotechnology, as well as friends from the Integrated Master's in Ocean Technology - none mentioned, none forgotten. You have made the discussions of science and the escapism from study well worth studying at UiB.

Finally, I am greatly in debt to my family and my beloved girlfriend, Cathrine, for patience, encouragement, support and care during my studies. I would never have accomplished my studies in such manner without your trusted support.

Erik Larsen
December 21, 2020
Bergen, Norway

Abstract

With the growing demand for renewable energy solutions in the world, floating windmills are said to be very effective and environmental friendly for ensuring future's energy demands. Hence, robust methods for evaluating the mechanical properties of seabed sediments, e.g. for mooring and stability of offshore installations, will be necessary. Knowledge about the elastic properties of the near-surface seabed, how the seabed changes its elastic properties based on water filling and how to measure the elastic properties of the seabed may be important. Additionally, methods for determining the mechanical properties of the seabed sediments may be important to understand how noise and vibrations from moored floating windmills spread along the seabed, and potentially leaking into the ocean.

In this thesis, the main objective is to present and model surface acoustic Scholte waves propagating at the fluid-solid interface. We use the rock physics based differential effective medium (DEM) model to investigate how the elastic properties of water filled silicates change as introduced to water inclusions in incremental manners. Then, we model the acoustic wavefields (i.e. negative pressure or vertical particle velocity) for an environmental model given in Johansen et.al. [1, table 2], added a solid sea ice layer on top. The wavefields are modeled using the wavenumber integration method Ocean Acoustic and Seismic Exploration Synthesis (OASES), which calculates the depth-dependent Green's function for a selected number of frequencies and determines the transfer function at any receiver position by evaluation the wavenumber integral in cylindrical coordinates.

The modeled wavefields are then compared to results from a seismic experiment conducted in Van Mijenfjorden, Svalbard in 2018. Due to aliasing effects, increasing resolution in the frequency-wavenumber domain may be important for group- and phase velocity determinations. Hence, a small study of the impact of reducing the receiver intervals, holding the total array length constant, is done.

Results from this study illustrates that the v_p/v_s-ratio of water filled silicates are orders of magnitude higher than more compact sediments, i.e. water filled silicates looses its shear strength as water inclusions are added. Seismic survey in shallow water show prominent Scholte wave data when using an airgun submerged to water at 4 meter depth, measuring the response at the seabed.

Contents

List of Abbreviations

Some abbreviations used in this master project are listed here.

Acoustics	
P-wave	Compressional (or primary) wave
S-wave	Shear (or secondary) wave
SH-wave	Shear horizontal wave
SV-wave	Shear vertical wave
DEM	Differential Effective Medium
OASES	Ocean Acoustic and Seismic Exploration Synthesis
SAFARI	Seismo-Acoustic Fast Field Algorithm for Range-Independent Environments
OASP	2-D Wideband Transfer Function module
PP	Pulse Post-processor
SU	CWP/SU: Seismic Un*x
CWP	Center for Wave Phenomena
SEG	Society of Exploration Geophysicists
SUSPECFK	F-K Fourier spectrum of data set
SUPHASEVEL	Multi-mode phase velocity dispersion map computed from shot record(s)
offset	Distance from source to receiver

this page is left blank by intention

Chapter 1

Introduction

1.1 Background and Motivation

With the growing demand for renewable energy solutions globally, floating windmills are said to be very effective and environmental friendly for ensuring future energy demands [2]. Hence, robust methods for evaluating the mechanical properties of seabed sediments, e.g. for mooring and stability of offshore installations, will be necessary. By utilizing the physical properties of the evanescent-, low-frequent-, surface-, acoustic- Scholte waves, one can map the near-subsurface seabed by measuring the Scholte phase- and group velocities [3], and based on an inversion model, tune rock physics models to determine the sediments' composition and porosity [1]. Additionally, methods for measuring the seabed sediments' mechanical properties may be essential to understand how noise and vibrations from moored floating windmills spread along the seabed and potentially leaking into the ocean.

In Arctic regions, one can measure the seabed sediments' mechanical properties on floating sea ice [4, 5, 1]. An advantage of using the floating sea ice is that practical operations such as submerging measurement instruments onto the seabed in straight lines are handy. However, the harsh Arctic climate can be challenging for the operating personnel. Many authors, e.g. [6], [7, 8], [9], [10] and [1], have demonstrated the use of Scholte waves for evaluating the mechanical properties of the seabed based on inversion methods. The seabed's mechanical properties heavily rely on the geological processes at the time of sediment deposition and the subsequent mechanical compaction [1]. This relates to sediment composition, porosity, granular structure, and shape and roughness of sediment grains in geological terms. Hence, knowledge about the sediment's effective elastic properties as a function of water-filled porosity could be of interest to determine the shear stiffness of water-filled porous rocks.

Using the wavenumber integration method OASES, a method for modeling the wavefield at the seabed is presented. This method is verified to be gentle to the marine aquatic life, e.g. to true seals [11], which may have their habitat in such Arctic areas. Due to the low shear wave

velocities in Arctic sediments, spatial aliasing effects are challenging. Hence, optimal survey design should be considered to avoid spatial aliasing effects by ensuring narrow enough receiver intervals and long enough receiver arrays.

The phase velocity of Scholte waves, e.g. given by Vinh [12], is highly dependent on the pressure wave velocity of the fluid(s) and the shear wave velocity of the solid(s), close to and at fluid-solid interfaces. Hence, Scholte waves can be used to sample the elastic properties of near-surface sediments [1]. By inverting measured Scholte wave data (e.g. by measured Scholte waves' phase- and group velocities), a model of the shear velocity depth profile can be constructed, which could be used to estimate the sediment composition with tuning rock physics models. Rock physics models, e.g. differential effective medium (DEM) models, can then be used to model the macro elasticity of multi-phased compositions as a function of water-filled porosity. Wavenumber integration methods, e.g. OASES [13, 14, 15], could then be used to model the response of the Scholte waves (e.g. dispersion relation, group- and phase velocities, etc.) in an environmental model with estimated compressional (or pressure)- and shear wave velocities. The DEM model could then be used to make new multi-phased media representative of the estimated compressional and shear-wave velocities. This process of estimating the shear velocities using inversion could then continue until a satisfactory environmental model exist.

In this thesis, the effective mechanical properties of some common Arctic water-filled porous minerals are analyzed by the DEM model based on a theory of elastic moduli by Kuster & Toksöz [16]. Then some modeling of Scholte wave group- and phase-velocities calculated at the seabed is presented, using the wavenumber integration method OASES-OASP for a representative environmental model given in [1, table 2], added a relatively thin floating ice layer on top. This was done since it can be shown that for shallow water seismic, i.e. large wavelengths and thin water layer compared to the skin depth, Scholte waves generated at the seabed could possibly be recorded by geophones placed on top of thin floating sea ice. Hence, in chapter 5, when defining the representative environmental model for the study area, we place a relatively thin ice layer on top of the water layer, with parameters given in [5]. Further, in chapter 5, we analyze the amplitudes (e.g. pressure and vertical particle velocities) from seismic shot gathers calculated both at the seabed and on top of floating ice. In chapter 6, we present results from measuring the amplitudes both at the seabed (using four component ocean-bottom nodes (trilobites)) and on top of floating sea ice (using three component geophones).

An additional section with modeling of ice flexural waves is included to show the effect of conducting seismic surveys on floating sea ice. Next, measured Scholte waves are presented from a seismic experiment conducted in 2018 in Van Mijenfjorden, Svalbard. Due to aliasing effects in the measured datasets, an optimal receiver interval, based on frequency-wavenumber spectra for different receiver intervals and holding the total line fixed, is suggested for measuring Scholte waves in the study area.

1.2 Limitations

In this master project, we have used two modeling techniques and three datasets to deal with the objectives. The first model is a DEM model based on the theory of Kuster & Toksöz [16]. This model is used to calculate the dynamic elastic moduli and average density of multi-phase media, incorporated the effect of pore interactions. The second model, the wavenumber integration technique *Ocean Acoustic and Seismic Exploration Synthesis* (OASES) [13, 14, 15], is used to model the seismo-acoustic propagation of airguns inducing acoustic waves in horizontally stratified environments in cylindrical coordinates. Third, seismic datasets used in this master project, are measured by four component (4C) ocean bottom-nodes (OBN) - one hydrophone and three geophones - and three component geophones placed in floating sea ice. One shot gather at two specific shot locations will be processed and presented in this text.

The DEM model by Kuster & Toksöz [16] is limited to i) isotropic, linear and elastic media, ii) dilute concentrations of inclusions, and iii) an assumption of idealized ellipsoidal inclusion shapes. Additionally, the model is limited to incident waves with wavelengths much larger than the inclusions' size and neglecting multiple scattering effects [16]. This model is an inclusion based technique, where one phase acts as the host medium, and the inclusion phase is gradually introduced in incremental manners [17]. The specific DEM model used in our calculations relate, but is not limited to, the bulk modulus K, shear modulus μ, compressional velocity v_p, shear velocity v_s, density ρ and the v_p/v_s-ratio as a function of porosity for the multi-phase media. The pore geometry of the inclusions is set to oblate spheroids (ellipsoidal shapes) for simplicity.

OASES, or specifically the *OASES-OASP: 2-D Wideband Transfer Functions* module, is an implementation of the wavenumber integration technique based on the depth-separated Helmholtz equation in cylindrical coordinates [18]. It calculates the depth-dependent Green's function for a selected number of frequencies and determines the transfer function at any receiver position by evaluating the wavenumber integral [15]. The resulting frequency response between source and receiver is outputted for each frequency and receiver pairs based on a specified horizontally stratified environmental model. The method assumes constant compressional (pressure for fluids)- and shear-wave velocities (m/s), densities (g/cm^3) and attenuation (dB/λ[(1)]) for each horizontal layer. For simplicity, we assume constant 0.1 dB/λ attenuation for all layers (except for the air upper half-space which is 0.0). The OASES-OASP procedure requires many frequencies, which are controlled by an OASES-integrated automatic wavenumber sampling regime. Other details regarding the OASES-OASP module and its input environmental models will be described in further details in chapter 2 and chapter 5.

When presenting the synthetic and measured seismograms, they are plotted as offset (m)

[(1)] It is unclear from Jensen [18] and the OASES manual [15] what the attenuation (dB/λ) is relative to.

vs. time (s), i.e. as wiggles in seismograms. The wiggles represent relative amplitudes, e.g. relative particle velocity or pressure differentials, from point-receiver pairs, calculated in OASES-OASP or measured by receiver instruments. Some typical seismograms encountered in shallow-water Arctic experiments are given in figure 1.1.

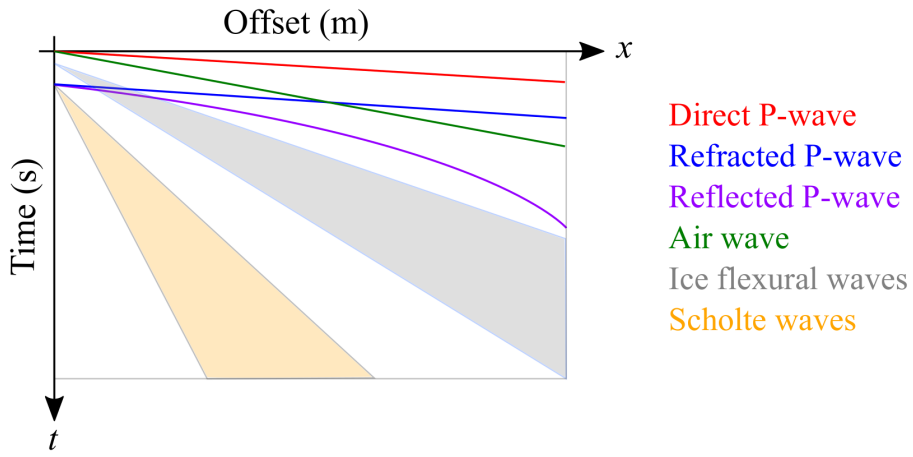

Figure 1.1: Qualitative illustration of a typical shot gather seismogram obtained in shallow-water Arctic seismic experiments on floating sea ice. The wave phenomena indicated are body waves (direct-, refracted- and reflected P-waves), airwave (also called bubble pulse induced by the airgun source), and surface waves (ice flexural- and Scholte waves). Other induced waves may also be present in seismic seismograms. Not all of the presented waves may be present in every seismogram obtained from shallow-water Arctic seismic experiments on floating sea ice. The waves present in seismograms are highly dependent on the data processing techniques used, the characteristics, geology, geometry, etc., of the seismic experiment. Modified from [19].

The representative shot gather in figure 1.1 shows some typical wave phenomena observed in seismograms for shallow-water Arctic seismic experiments on floating sea ice. Depending on the offset and time axes' scaling, the obtained seismograms might alter accordingly; hence, the axes are not quantified in the figure. The surface waves' characteristics in these seismograms are of main interest in this master project, e.g. the Scholte- and ice flexural waves, which seem to have these relatively broad "fan-shaped" signatures (yellow and gray). High presence of these surface waves are common in seismic records from arctic seismic experiments on floating sea ice [4, 5, 1].

Based on the space and time-dependent seismograms, these traces are Fourier transformed into the frequency-wavenumber ($f-k$) and frequency-phase velocity ($f-v_{ph}$) domains, which might yield additional information about the wavenumbers and phase velocities of the waves observed in the seismograms. Other properties, such as surface roughness estimations and tilted layers, will not be considered in this master project.

The seismic experiment relevant for this master project is the blue line in figure 1.2, also called the *Svea 2018* seismic experiment.

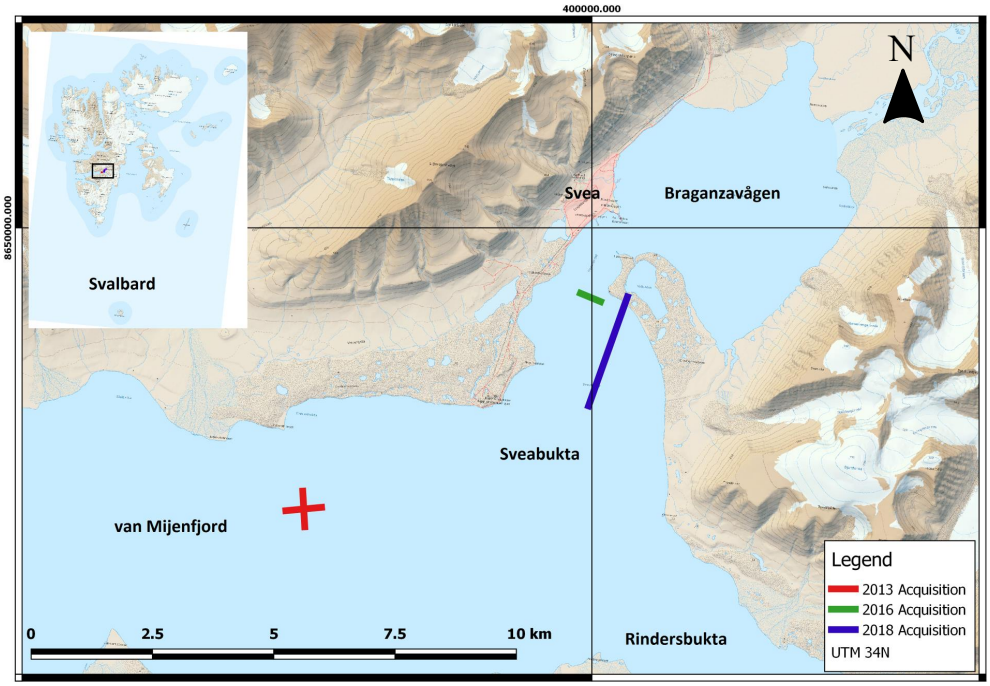

Figure 1.2: Topographic map of the study area, with indications of three seismic exploration experiments conducted in 2013, 2016 and 2018. The seismic data from the 2D seismic line in the 2018 experiment (blue) is to be analyzed in greater details, also called the ”Svea 2018” seismic experiment. Modified from [5].

As we see from figure 1.2, the Svea 2018 seismic line is the longest compared to the 2013 and 2016 seismic lines. The total spread of the Svea 2018 seismic experiment was 2.4 km long. The ice thickness in the Svea 2018 experiment was reported to vary between 20 and 40 cm, and the water depths varied between 0 to 50 m [5]. The shots were done in a *downstream* orientation, meaning the shots were fired from northeast to southwest according to figure 1.2. Both airguns and detonating cords were used as seismic sources in the Svea 2018 experiment. The main purpose of this experiment was to "explore methods for suppressing noise at shorter wavelengths" [20], using dense spacing of shots and receivers. Additionally, the Svea 2018 seismic line includes some shots on land, i.e. detonating cord shots at the Credner Moraine, a moraine separating Braganzavågen and Sveabukta, see figure 1.2.

Three master's thesis has been written using some of the seismic data from this area, e.g. Jensen [21] who studied flexural wave noise generated by the sea ice, Stemland [19] who studied the survey geometry and impact on pinnipeds from seismic acquisition, and Furland [22] who studied seismic wave propagation in frozen and partly frozen surfaces. The dataset from the Svea 2018 experiment has not been analyzed in detail by the Geophysics group at UiB, which is to be done here for two shot positions.

Several scientific papers have also been published, based on data from the three experiments indicated in figure 1.2, e.g. Stemland et.al. [11], Johansen et.al. [4], Johansen et.al. [5] and Johansen & Ruud [1]. There was also conducted an seismic experiment in 2017 (not indicated in figure 1.2), located west to, and in parallel with, the Svea 2018 experiment [4].

The datasets acquired in Svea 2018 also include some data measured using explosives as seismic source, i.e. exploding detonating cords placed on top of the sea ice. These detonating cord datasets will not be presented because detonating cords are often much more wideband and uncontrollable sources than the airgun sources [5]. An initial intention with this master project was to see if we could measure Scholte waves in water when detonating a detonating cord on land, i.e. at the Credner Moraine. The hypothesis was that by allowing ground surface waves (e.g. leaky Rayleigh waves) to propagate into seawater, these waves could be converted to Scholte waves detectable by submerged hydrophones and/or ocean-bottom nodes (OBN) measurement devices. This phenomenon was not detected; hence we will not present any detonating cord data. Another argument for not presenting the detonating cord datasets is that airgun sources facilitate more to generate low-frequency seismic energy than detonating cords [4, 5]. When processing the shot gathers, we apply processing methods such as gain control, trace balancing based on the traces' RMS or mean values, and bandpass filtering.

Other shot gathers from the Svea 2018 seismic experiment could be of interest to process and analyze. Nevertheless, we limit ourselves to three specific shot gathers, limiting the extent of this project and being more targeted towards mapping seabeds using Scholte waves.

1.3 Objectives

The main objective of this master thesis is to present modeled and measured Scholte waves in space-time, frequency-wavenumber and frequency-phase velocity domains, from calculated and measured amplitudes at, or close to, fluid-solid interfaces - with special emphasis on the physics behind. The measured data was gathered in Van Mijenfjorden, Svalbard in late February/beginning of March 2018, by students and technical staff attending the M.Sc./PhD student course: *AG335/835: Seismic Arctic Exploration (10 ETCS)*, arranged by the University Centre in Svalbard (UNIS).

Another objective in this master project is to suggest a more suitable measurement setup for measuring Scholte waves, with special emphasis on avoiding aliasing effects from slowly propagating Scholte waves. This will be done by modeling in OASES, where optimization of the receiver intervals will be analyzed in relation to the Nyquist wavenumber criterion. Some representative shot gathers, frequency-wavenumber- and frequency-phase velocity spectra for some receiver intervals will be presented and discussed.

1.4 Outline

The outline of this thesis is:

Chapter 1 present the motivation and objectives of this master project.

Chapter 2 present some theory needed to understand the wavenumber integration method OASES and Scholte waves in fluid-solid spaces.

Chapter 3 present some geological data about common minerals found in and around Van Mijenfjorden, Svalbard, and present the theory behind the rock physics model; differential effective medium (DEM) by Kuster & Toksöz [16] - including a description of the input files to this model. Last, some numerical examples of calculated macro elastic properties for some silicate-water mixes will be presented.

Chapter 4 present the experimental setup and methods used in the Svea 2018 seismic experiment. A short section about the seismic signal processing used will also be presented, followed by a section describing the plotting of the processed data using the CWP/SU package [23].

Chapter 5 present a description of the input files to the OASES-OASP module. Then, some numerical examples of using OASES-OASP for horizontally stratified environments - including some numerical results using OASES-OASP with three different receiver arrays - with the environmental model given in Johansen & Ruud [1], will be presented. The receiver arrays used in OASES-OASP, are based on the specific receiver configuration used for the Svea 2018 Arctic seismic experiment.

Chapter 6 present and discuss the processed experimental shot gathers from the Svea 2018 seismic experiment.

Chapter 7 overall discussion.

Chapter 8 conclusion and recommendations for further work

Appendices include scripts, codes, input files, source and receiver instrumentation data used in this thesis. We have tried to thoroughly comment, and include all scripts and codes necessary for others to recreate the results.

Chapter 2

Theory

This chapter will present the basic theory for Scholte waves, mainly based on theory found in Jensen et.al. [18, ch. 2 and 4]. For consistency, to distinguish vectors from scalars, we try to indicate vectors using underlines, e.g. $\underline{u}$ is a vector, and u_x is a scalar.

2.1 The lossless linear wave equations in fluids and solids

Acoustic waves in fluids (e.g. gases and liquids) follow the laws of fluid mechanics [24, ch. 5]. If we assume lossless, small amplitudes, and constant (or slowly variable) density in a fluid, the lossless linear wave equation for complex sound pressure in the fluid, p, can be given as in [24], as in equation (2.1),

$$\left(\nabla^2 - \frac{1}{v_p^2}\frac{\partial^2}{\partial t^2}\right) p(\underline{r}, t) = 0 \tag{2.1}$$

where v_p is the thermodynamic sound velocity for sound propagation in fluids, which can be defined as in [24], as in equation (2.2),

$$v_p \equiv \sqrt{\frac{K_f}{\rho_0}} = \sqrt{\left(\frac{\partial P_f}{\partial \rho_f}\right)_{\rho_0}} \tag{2.2}$$

where K_f is the adiabatic bulk modulus, ρ_0 is the ambient density, P_f is the pressure amplitude and $\rho_f = \rho_{0,f} + \rho'_f$, where ρ'_f is the acoustic density, of the fluid. In Cartesian coordinates we can write $\underline{r} = (x, y, z)$, where $\underline{r}$ denotes the radial vector.

The wave equations in solids can be described by the *particle displacement vector*, $\underline{u} = (u_x, u_y, u_z)$, using the *Helmholtz method* [25]. We can use the *Helmholtz scalar function*, ϕ, for longitudinal displacements, and the *Helmholtz vector function*, $\underline{\psi} = (\psi_x, \psi_y, \psi_z)$, for particle displacements, having the property, $\underline{u} = \nabla\phi + \nabla \times \underline{\psi}$ [26]. This yields the two similar

wave equations (2.3) and (2.4),

$$\left(\nabla^2 - \frac{1}{c_p^2}\frac{\partial^2}{\partial t^2}\right)\phi(\underline{r},t) = 0 \tag{2.3}$$

$$\left(\nabla^2 - \frac{1}{c_s^2}\frac{\partial^2}{\partial t^2}\right)\underline{\psi}(\underline{r},t) = 0 \tag{2.4}$$

for longitudinal and shear waves[(1)], respectively. The two wave equations (2.3) and (2.4) are independent of each other, which imply that they propagate independently of each other in an unbounded (infinite) solid medium [26]. When boundaries are introduced, these waves interact and produce new waves. In an isotropic, homogeneous, elastic solid medium, the longitudinal wave velocity, c_p, and the shear wave velocity, c_s, can be defined as in [26], given in equations (2.5) and (2.6),

$$c_p \equiv \sqrt{\frac{\lambda_s + 2\mu_s}{\rho_s}} = \sqrt{\frac{K_s + \frac{4}{3}\mu_s}{\rho_s}} \tag{2.5}$$

$$c_s \equiv \sqrt{\frac{\mu_s}{\rho_s}} \tag{2.6}$$

where λ_s and μ_s are the Lamé constants for the solid, K_s is the bulk modulus (also called the *incompressibility*) of the solid, and ρ_s is the density of the solid.

The wave equation for the y-component of the vertical particle displacement potential, ψ_y, can be given as in equation (2.7),

$$\left(\nabla^2 - \frac{1}{c_s^2}\frac{\partial^2}{\partial t^2}\right)\psi_y(\underline{r},t) = 0 \tag{2.7}$$

which is the displacement potential related to shear vertical waves in solids [27, p. 5.61].

In the wave equations (2.1), (2.3), (2.4) and (2.7), ∇ is the so-called *Laplacian operator*, which is dependent on the choice of coordinate system. As we will see later, will boundary conditions restrict the choice of coordinate system [18, p. 84]. For example will *cylindrical coordinates* be more facilitated in horizontally stratified environments.

For $r > 0$ in a cylindrical coordinate system, i.e. with *radial vector*, $\underline{r} = (r, \varphi, z)$, we can define the Laplacian operator given in [18, p. 74], as in equation (2.8),

[(1)] Lohne et.al. [26] writes that equation (2.4) relates to shear vertical (SV) waves, whereas [27, p. 5.61] writes that since $\underline{\psi} = (\psi_x, \psi_y, \psi_z)$ is a vector, for plane waves in Cartesian coordinates, only the ψ_y is related to shear vertical waves, whereas ψ_x and ψ_z are related to shear horizontal waves. Therefore, to avoid misconceptions, we specify that for plane waves in Cartesian coordinates, only ψ_y is related to shear vertical waves, given in equation (2.7).

$$\nabla^2 = \frac{1}{r}\frac{\partial}{\partial r} r \frac{\partial}{\partial r} + \frac{1}{r^2}\frac{\partial^2}{\partial \varphi^2} + \frac{\partial^2}{\partial z^2} \tag{2.8}$$

where r is the perpendicular distance from the z-axis to the field point, and φ is the *azimuth angle*.

2.1.1 Source representation

Natural or artificial phenomena produce underwater sound through forced mass injections [18, p. 69]. In the wave equations (2.1), (2.3), (2.4) and (2.7), the force terms were neglected when introducing the mass conservation equation needed to derive the homogeneous wave equations (see derivating in for example [24, ch. 5]). The force terms may be introduced to the homogeneous wave equations (2.1), (2.3), (2.4) and (2.7). This result in the *inhomogeneous wave equations*, which for sound pressure in water, $p(\underline{r}, t)$, is given in equation (2.9),

$$\left(\nabla^2 - \frac{1}{v_p^2}\frac{\partial^2}{\partial t^2}\right) p(\underline{r}, t) = f(\underline{r}, t) \tag{2.9}$$

and for longitudinal displacement in solid, $\phi(\underline{r}, t)$, is given in equation (2.10),

$$\left(\nabla^2 - \frac{1}{c_p^2}\frac{\partial^2}{\partial t^2}\right) \phi(\underline{r}, t) = f(\underline{r}, t) \tag{2.10}$$

and for vertical particle displacement potential in solid, $\psi_y(\underline{r}, t)$, given in [18, p. 69], as in equation (2.11),

$$\left(\nabla^2 - \frac{1}{c_s^2}\frac{\partial^2}{\partial t^2}\right) \psi_y(\underline{r}, t) = f(\underline{r}, t). \tag{2.11}$$

The force terms, $f(\underline{r}, t)$, in equations (2.9), (2.10) and (2.11), represent the volume injection as a function of space and time. We will come back to an expression for the force term corresponding to a simple point source in cylindrical coordinates later on.

2.2 Solution to the wave equations

With associated boundary and radiation conditions, different methods are used to solve for the *full-waveform* equation (2.11) (or equivalently for pressure or particle velocity). In Jensen et.al. [18, ch. 3-6] the numerical *ray method*, *wavenumber integration technique*, *normal mode* and *parabolic equations* are discussed. Jensen et.al. [18, p. 70] writes that the major difference between the various techniques is the mathematical manipulation of equation (2.11) applied before the actual implementation of the solution, and the form of the wave

equation used.

2.2.1 The Helmholtz equation

Jensen et.al. [18, p.71] states that in equation (2.11), the coefficients to the two differential operators are independent of time, so the dimension of the wave equation can be reduced to three by use of the frequency-time *Fourier transform pair*. The *Fourier transform* and the *inverse Fourier transform* for a function f, are given in Jensen et.al. [18, p. 71]. In equations (2.12) and (2.13) are the Fourier transform pairs given as function of the vertical particle displacement potential,

$$\psi_y(t) = \frac{1}{2\pi}\int_{-\infty}^{\infty} \Psi_y(\omega) e^{-i\omega t} d\omega \tag{2.12}$$

$$\Psi_y(\omega) = \int_{-\infty}^{\infty} \psi_y(t) e^{i\omega t} dt \tag{2.13}$$

where i is the imaginary unit, having the property $i = \sqrt{-1}$, and Ψ_y denotes the frequency representation of ψ_y. The frequency-time Fourier transform pair lead to the frequency-domain wave equation, or *Helmholtz equation*. Using equation (2.12) in equation (2.11), we get the Helmholtz equation [18, p. 71] for the vertical particle displacement potential as in equation (2.14),

$$\left[\nabla^2 + k^2(\underline{r})\right] \Psi_y(\underline{r},\omega) = f(\underline{r},\omega) \tag{2.14}$$

where $k(\underline{r})$ is the so-called *medium wavenumber* at frequency $\omega = 2\pi f$, defined as in equation (2.15),

$$k(\underline{r}) = \frac{\omega}{v(\underline{r})}. \tag{2.15}$$

Note that the right side i equation (2.14), i.e. the force term, is also Fourier transformed and is now dependent of angular frequency, $\omega = 2\pi f$.

Jensen et.al. [18] states that for numerical wavenumber integration methods in general, the Helmholtz equation forms the theoretical basis since "many ocean acoustic applications are narrow band by nature" [18, p. 71]. Nevertheless, the simplification (i.e. reduction in dimension of the partial differential equation) is achieved at the cost of having to evaluate the inverse Fourier transform, which for vertical particle displacement potential is given in equation (2.12).

2.2.2 Layered media and waveguides

For heterogeneous media, the sound speed and density vary in one or more space coordinates. In the ocean environment, the sound speed varies more or less continuously in the water column. However, for the seabed and the sub-bottom interfaces between different geological layers, the medium properties "abruptly" [18, p. 83] change. The heterogeneity of the seabed and sub-bottom interfaces result in discrete discontinuities in the medium properties [18, p. 83], hence the linear wave equations (2.1), (2.3) and (2.7) are not valid at the discontinuity itself, and the problem has to be formulated using boundary conditions [18, p. 83].

In table 2.1 are some important boundary conditions typically encountered in Arctic seismic experiments, given in Jensen et.al. [18] and Johansen et.al. [4] as in table 2.1. From table

Table 2.1: Boundary conditions for various types of interfaces, where "=" means the physical parameter must be continuous over the interface, "−" means the vanishing conditions and "0" means that the physical parameter is not involved in the boundary condition. The physical parameters $(u_r, u_z, \sigma_{rz}, \sigma_{zz})$ for are defined in chapter 2.5. Modified from [4, table 2].

Interface type	Physical parameter			
	u_r	u_z	σ_{rz}	σ_{zz}
Fluid-vacuum	0	0	0	−
Fluid-fluid	0	=	0	=
Fluid-solid	0	=	−	=
Solid-vacuum	0	0	−	−
Solid-solid	=	=	=	=

2.1, we see that depending on interface type, different boundary conditions apply to different physical parameters, with physical parameters defined in chapter 2.5 for homogeneous, isotropic elastic media. For example at a fluid-solid interface, we see that the vertical particle displacement, u_z, and the normal stress, σ_{zz}, must be continuous across the interface. However, the radial stress, σ_{rz}, is vanishing, and the horizontal particle displacement, u_r, is not involved at fluid-solid interfaces. At such fluid-solid interfaces, we find Scholte waves first described by Scholte [28]. Later, Vinh [12] have derived an exact formulae for the velocity of Scholte waves in fluid-solid halfspaces, using the complex function method (see also [29, 30, 31]).

For a simplified discrete model of the ocean environment, we can assume that we divide the ocean environment into plane, parallel interfaces, where all layers are assumed homogeneous [18, p. 83]. This allows for changes in density to be handled by the appropriate boundary conditions between regions of constant density, which at the boundaries require *continuity of pressure* and *continuity of displacement (or velocity)* [18, p. 69]. Such a horizontally layered medium of water-seabed-bedrock (lower halfspace) is illustrated in figure

2.1[(2)]

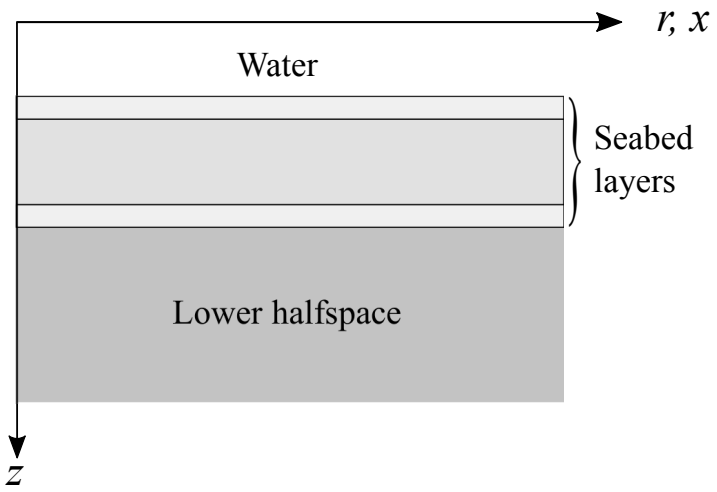

Figure 2.1: Horizontally stratified environment, consisting of a water layer on top, some homogeneous seabed layers (i.e. sediments) and a lower homogeneous halfspace (i.e. rock bottom). Modified after [18, p. 83].

For horizontally stratified waveguides, the properties only depend on the depth z. And for range-independent horizontally stratified waveguides, the Helmholtz equation (2.14) takes the form given in [18, p. 84], as in equation (2.16),

$$\left[\nabla^2 + k^2(z)\right]\psi_y(\underline{r}) = f(\underline{r}) \tag{2.16}$$

In this master thesis, the wavenumber integration method (*OASES-OASP*) is used, which in general is based on solving the *depth-separated Helmholtz equation* in cylindrical coordinates [4], by calculating the *depth-dependent Green's function* for a selected number of frequencies [15].

2.3 Integral transform techniques - point source in range-independent environment

For a situation with a simple point source (i.e. the radius, a, of the spherical point source is small compared to the acoustic wavelength, i.e. $ka << 1$ [18, p. 76]) in a range-dependent environment of stratified homogeneous layers, the acoustic field only varies with depth z and the horizontal range r away from the source. In such cases, the most straightforward

[(2)]In figure 2.1 the simplified model of the ocean is presented with no ice layer floating on top of the water layer, which we normally will encounter in Arctic seismic explorations in wintertime. This was done to be consistent with the derivation in [18], although the ice layer can be modeled as a solid medium floating on top of the water layer [15, 18, 5]. As we will see later, for shallow water seismic, e.g. large wavelengths and thin water layers compared to the skin depth, Scholte waves generated at the seabed could be recorded by geophones placed on top of thin floating sea ice [1].

coordinate system choice is cylindrical [18, p. 86], with the vertical z-axis passing through the point source at depth z_s and the radial r-axis being parallel to the interfaces $m-1$ and m, as illustrated in figure 2.2.

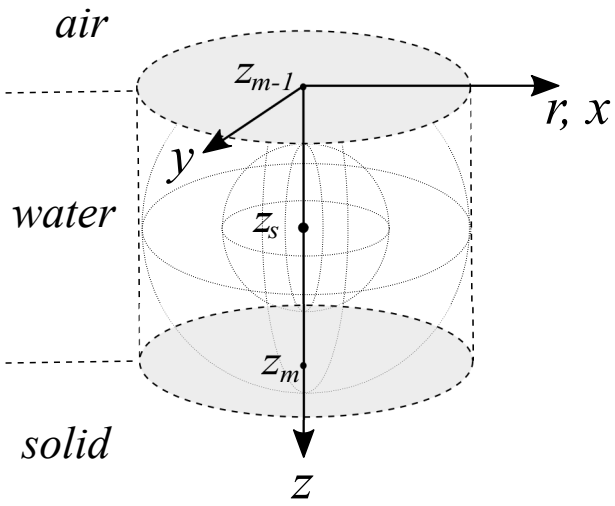

Figure 2.2: Three layered environmental model (air-water-solid) in cylindrical coordinates ($\underline{r} = (r, \varphi, z)$) in the three dimensional Euclidean space, with an omnidirectional point source located at depth z_s on the z-axis. z_{m-1} represents the depth at interface $m-1$ (e.g. water-air interface) and z_m represents the depth at interface m (e.g. water-solid interface). r is the radial axis. Note that the figure yields for omnidirectional point source in water, and the azimuth angle φ is not included.

We can now integrate the Helmholtz equation (2.16) with the Laplace operator given in equation (2.8), with respect to the azimuth angle, φ. Then we can apply the *Hankel transform pair* given in [18, p. 86], as in equations (2.18) and (2.17) for the vertical particle displacement potential,

$$\psi_y(r,z) = \int_0^\infty \Psi_y(k_r,z) J_0(k_r r) k_r \, dk_r \tag{2.17}$$

$$\Psi_y(k_r,z) = \int_0^\infty \psi_y(r,z) J_0(k_r r) r \, dr \tag{2.18}$$

where $J_0(k_r r)$ is the *zeroth order Bessel function* and Ψ_y denotes the Hankel transformed ψ_y.

When using the Hankel transform in equation (2.17), the resulting field is decomposed into conical waves [18, p. 87]. The zeroth-order Bessel function can be defined as in [18, p. 87], as in equation (2.19),

$$J_0(k_r r) = \frac{1}{2}\left[H_0^{(1)}(k_r r) + H_0^{(2)}(k_r r) \right] \tag{2.19}$$

where $H_0^{(1)}(k_r r)$ is the *zeroth order Hankel function of first kind* and $H_0^{(2)}(k_r r)$ is the *zeroth order Hankel function of second kind*, associated with outward and inward propagating waves,

respectively [32].

The *depth-separated Helmholtz equation* in cylindrical coordinates can then be given as in [18, p. 86], as in equation (2.20),

$$\left[\frac{\partial^2}{\partial z^2} + (k^2 - k_r^2)\right] \Psi_y(k_r, z) = S_\omega \frac{\delta(z - z_s)}{2\pi} \tag{2.20}$$

where $k_r = \omega / v_r$ is the *horizontal wavenumber* with *horizontal phase velocity*, v_r, and $\delta(z - z_s)$ is the *dirac delta function* with argument $(z - z_s)$, where z_s is the depth position of the source. Mathematically can the dirac delta function be defined as in [33, Appendix A], as for argument $(z - z_s)$ is given in equations (2.21) and (2.22),

$$\delta(z - z_s) = 0 \qquad \texttt{if } z \neq z_z \tag{2.21}$$

$$\int_{-\infty}^{\infty} \delta(z - z_s) dz = 1 \tag{2.22}$$

In terms of particle displacement potential, Jensen et.al. [18, p. 82] define the source strength, S_ω, in equation (2.20) as in equation (2.23),

$$S_\omega = -\frac{4\pi}{\rho\omega^2} \tag{2.23}$$

which we see is dependent on the angular frequency of the source. For a source with angular frequency ω, which produces a pressure amplitude of 1 Pa at $r = 1$ m away from the source, this source strength has unit $\mathrm{m^3 s^2/kg}$ or $\mathrm{m^2/Pa}$ according to Jensent et.al. [18, p. 82].

To solve for the depth-separated Helmholtz equation in equation (2.20), we can now use the Fourier transform of the *Green's theorem* on the form given in [18, p. 85], as in equation (2.24),

$$\Psi(k_r, z) = -S_\omega G_\omega(k_r, z, z_s) \tag{2.24}$$

where $G_\omega(k_r, z, z_s)$ is the so-called *depth-dependent Green's function*, which must satisfy the same boundary conditions as $\Psi(k_r, z)$ to hold. Since $G_\omega(k_r, z, z_s)$ is the Fourier transform of the general Green's function, it has the form given in [18, p. 85], as in equation (2.25),

$$G_\omega(k_r, z, z_s) = g_\omega(k_r, z, z_s) + H_\omega(k_r, z) \tag{2.25}$$

where $g_\omega(k_r, z, z_s)$ is the Fourier transform of the *free-field Green's function*, satisfying the inhomogeneous Helmholtz equation given in [18, p. 85], as in equation (2.26),

$$\left[\frac{\partial^2}{\partial z^2} + (k^2 - k_r^2)\right] g_\omega(k_r, z, z_s) = -\frac{\delta(z - z_s)}{2\pi} \tag{2.26}$$

and $H_\omega(k_r, z)$ in equation (2.25) satisfies the homogeneous Helmholtz equation given in equation (2.27),

$$\left[\frac{\partial^2}{\partial z^2} + (k^2 - k_r^2)\right] H_\omega(k_r, z) = 0. \tag{2.27}$$

Equations (2.24) and (2.25) express the total solution of the "superposition of the field" [18, p. 85], produced by the source in an infinite medium and a homogeneous solution, which must satisfy the boundary conditions.

Jensen et.al. [18, p. 84] writes that since the boundary conditions for equation (2.16) are independent of the horizontal coordinates, they can be Fourier (i.e. Hankel-) transformed. It can then be shown that this results in that the solution is now obtained by determining the homogeneous solution $H_\omega(k_r, z)$, which superimposed on the free-field Green's function $g_\omega(k_r, z, z_s)$, satisfies the same boundary conditions [18, p. 85]. The total spatial solutions then follows by evaluating the inverse Hankel transform given in equation (2.18).

2.4 Point source in fluid halfspace

If we place an omnidirectional point source in a homogeneous fluid in cylindrical coordinates, as in figure 2.2, the solution to the homogeneous equation is of the form as in [18, p. 87], given in equation (2.28),

$$H_\omega(k_r, z) = A^+(k_r)e^{ik_z z} + A^-(k_r)e^{-ik_z z} \tag{2.28}$$

where A^+ and A^- are constant which must be determined by boundary conditions, and k_z is the vertical wavenumber, defined as in equation (2.29),

$$k_z^2 = k^2 - k_r^2. \tag{2.29}$$

Jensen et.al. [18] writes that since the Hankel transform in equation (2.17) must be evaluated over a "semi-infinite wavenumber domain" [18, p. 87], we can therefore define the roots in equation (2.29), as in equation (2.30),

$$k_z = \begin{cases} \sqrt{k^2 - k_r^2}\,, & k_r \leqslant k \\ i\sqrt{k_r^2 - k^2}\,, & k_r > k \end{cases} \tag{2.30}$$

If $z \to \infty$, the first term in the homogeneous equation (2.28) $\left(\texttt{i.e. } A^+(k_r)e^{ik_z z}\right)$ corresponds to downward propagating waves for $k_r < k$, and exponentially decaying waves for $k_r > k$ [18, p. 88]. Jensen et.al. [18, p. 88] further states that this first term can be eliminated for $z \to -\infty$ "due to the radiation condition for all values of k_r" [18, p. 88]. And likewise, the second term

can be eliminated for $z \to +\infty$.

Consequently, the *radiation condition* require the homogeneous solutions to be on the form as in [18, p. 88], given in equation (2.31),

$$H_\omega(k_r, z) = \begin{cases} A^+(k_r)e^{ik_z z}, & z \to +\infty \\ A^-(k_r)e^{-ik_z z}, & z \to -\infty \end{cases} \tag{2.31}$$

The inhomogeneous free-field Green's function in equation (2.26) will now be solved. Except for at source depth $z = z_s$, the Green's function satisfies the homogeneous equation [18, p. 88], with solutions similar to equation (2.31). If we consider symmetry for the field with respect to $z = z_s$, we get the solution given in [18, p. 88], as in equation (2.32),

$$g_\omega(k_r, z, z_s) = \begin{cases} A(k_r)e^{ik_z(z-z_s)}, & z \geqslant z_s \\ A(k_r)e^{-ik_z(z-z_s)}, & z \leqslant z_s \end{cases} \tag{2.32}$$

and we can write the total solution as in equation (2.33),

$$g_\omega(k_r, z, z_s) = A(k_r)e^{ik_z|z-z_s|} \tag{2.33}$$

The amplitude $A(k_r)$ in equation (2.33) we can calculate from integrating equation (2.20) over a small interval close to the source depth z_s, i.e. $[z_s - \epsilon, z_s + \epsilon]$ for small $\epsilon > 0$, and insert the result in the derivative of equation (2.33) [18, p. 88]. We then get the solution for the amplitude $A(k_r)$ given in [18, p. 88], see equation (2.34),

$$A(k_r) = -\frac{1}{i4\pi k_z} \tag{2.34}$$

which inserted into equation (2.33) yields equation (2.35),

$$g_\omega(k_r, z, z_s) = -\frac{e^{ik_z|z-z_s|}}{i4\pi k_z} \tag{2.35}$$

The point source Green's function in an infinite medium can be obtained as the inverse Hankel transform of the free-field depth-dependent Green's function in equation (2.35), to obtain the result given in equation (2.36),

$$g_\omega(r, z, z_s) = \frac{i}{4\pi}\int_0^\infty \frac{e^{ik_z|z-z_s|}}{k_z} J_0(k_r r)\, k_r\, dk_r \tag{2.36}$$

Equation (2.36) is known as the *Sommerfeld-Weyl integral* [18, p. 89]. This equation composes the point source field into conical waves, which propagate cylindrically in the horizontal direction. At the medium wavenumber, $k_r = k$, the Green's function (2.36) has a so-called *square root singularity*, where the magnitude of the function is independent of the

receiver depth for $k_r \leqslant k$. This singularity can be avoided by computing the wavenumber kernel along a "contour displaced into the complex plane by an amount given in equation (4.115)", see [18, p. 270]. This ensures a numerically stable integration of equation (2.36).

For the wavenumber spectrum $k_r \leqslant k$ in equation (2.36), it corresponds to waves propagating in the vertical direction due to the purely imaginary argument of the exponential function in equation (2.35), and it is referred to as the *radiating spectrum* [18, p. 89]. For $k_r > k$, the vertical wavenumber k_z is imaginary and the magnitude becomes exponentially decaying with depth, and it is called the *evanescent spectrum* [18, p. 89].

2.5 Displacements and stresses of horizontally stratified elastic solid layers

Assume horizontally stratified layered solid environment with layers $m = (1,2,3,...,m,m+1,N)$, separated by interfaces $m = (1,2,3,...,m,N-1)$, as in figure 2.3. For a homogeneous,

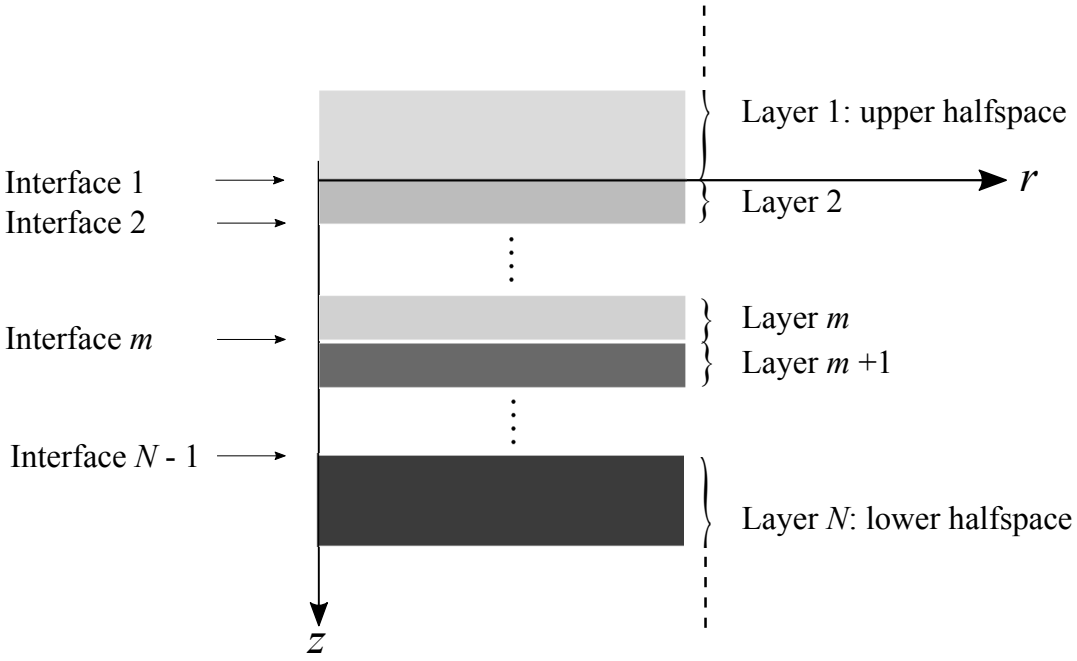

Figure 2.3: Horizontally stratified layered solid environment in cylindrical coordinate system. Modified after [18, p.235].

isotropic elastic solid layer m with Lamé constants λ_s and μ_s, and density ρ_s, it can be shown [34, ch. 2] that *the equation of motion* is satisfied if the particle displacements are expressed

in terms of scalar potentials $\{\phi_m, \psi_{y,m}\}$[3], as in equations (2.37) and (2.38),

$$u_{r,m}(r,z) = \frac{\partial}{\partial r}\phi_m(r,z) + \frac{\partial^2}{\partial r \partial z}\psi_{y,m}(r,z) \tag{2.37}$$

$$u_{z,m}(r,z) = \frac{\partial}{\partial z}\phi_m(r,z) - \frac{1}{r}\frac{\partial}{\partial r}r\frac{\partial}{\partial r}\psi_{y,m}(r,z) \tag{2.38}$$

for layer $m = 1,2,3,..,m,m+1,N$. In equation (2.37), $u_{r,m}(r,z)$ is the *radial particle displacement* and in equation (2.38), $u_{z,m}(r,z)$ is the *vertical particle displacement* for fields produced by omnidirectional point sources in solid layer m. In the absence of sources, the potentials satisfy the uncoupled, homogeneous Helmholtz equations given in [18, p. 240], as in equations (2.39) and (2.40),

$$\left[\nabla^2 + k_m^2\right]\phi_m(r,z) = 0 \tag{2.39}$$

$$\left[\nabla^2 + \kappa_m^2\right]\psi_{y,m}(r,z) = 0 \tag{2.40}$$

where $k_m = \omega/c_{p,m}$ and $\kappa_m = \omega/v_{s,m}$ are the wavenumbers corresponding to compressional and shear velocities in solid layer m, respectively. The compressional and shear velocities in solid layer m defined in [18, p. 240], can be defined as in equations (2.41) and (2.42),

$$c_{p,m} = \sqrt{\frac{\lambda_{s,m} + 2\mu_{s,m}}{\rho_{s,m}}} = \sqrt{\frac{K_{s,m} + \frac{4}{3}\mu_{s,m}}{\rho_{s,m}}} \tag{2.41}$$

$$v_{s,m} = \sqrt{\frac{\mu_{s,m}}{\rho_{s,m}}} \tag{2.42}$$

where $K_{s,m} = (\lambda_{s,m} + 2\mu_{s,m}/3)$ in equation (2.41) is the *bulk modulus* of the solid in layer m.

Both $\phi_m(r,z)$ and $\psi_{y,m}(r,z)$ in equations (2.39) and (2.40), are on the form as equation (2.20), and can therefore be depth separated [18, p. 240]. As for the case of homogeneous fluid (see for example [18, ch. 4.2.2]), the constant wave speed in the solid layer also lead to simple exponential functions in depth for solid layer m. Consequently, by using the Hankel transform (given in equation (2.17)), the potentials have the integral representations for angular frequency ω given in [18, p. 240], as in equations (2.43) and (2.44)[4],

[3] As commented for in equation (2.4) in chapter 2.1, Jensen et.al. [18] do not differ between ψ, $\underline{\psi}$ and ψ_y, ref. equations (2.37) and (2.38), which is done here.

[4] In equation (2.44), Jensen et.al. [18] compensates for the fact that the shear potential has one more spatial derivative than the compressional potential, by multiplication with the factor ${k_r}^{-1}$, which comes from making the dimension of the (yet unknown) amplitudes $A^{\pm}$ and $B^{\pm}$ identical [18, p. 241]. We have commented on this, and we stick with describing for ψ_y.

$$\phi_m(r,z) = \int_0^\infty \left[A_m^- e^{-ik_{z,m}z} + A_m^+ e^{ik_{z,m}z} \right] J_0(k_{r,m}r) k_{r,m} dk_r \tag{2.43}$$

$$\psi_{y,m}(r,z) = \int_0^\infty \left[B_m^- e^{-i\kappa_{z,m}z} + B_m^+ e^{i\kappa_{z,m}z} \right] J_0(k_{r,m}r) k_{r,m} dk_r \tag{2.44}$$

with their respective vertical wavenumbers given in equations (2.45) and (2.46),

$$k_{z,m} = \sqrt{k_m^2 - k_{r,m}^2} \tag{2.45}$$

$$\kappa_{z,m} = \sqrt{\kappa_m^2 - k_{r,m}^2} \tag{2.46}$$

where A_m^- and B_m^- in equations (2.43) and (2.44) represent longitudinal and shear waves' amplitudes with decreasing z-value in layer m, and A_m^+ and B_m^+ represent longitudinal and shear waves' amplitudes with increasing z-value in layer m. We will now treat the rest of this section without the and "m" subscripts, for easier notations, which follow the notation given in [18, ch. 4]. This means that we treat each layer m by its own, with longitudinal wavenumber $k = \sqrt{k^2 - k_r^2}$ and shear wavenumber $\kappa = \sqrt{\kappa^2 - k_r^2}$.

It can be shown [18, p. 241], that from inserting the integral representations in equations (2.43) and (2.44), into the displacement equations (2.37) and (2.38), we get the integral representations for the radial displacement given in [18, p. 241], as in equation (2.47),

$$\begin{aligned} u_r(r,z) = \int_0^\infty \Big\{ & -k_r A^- e^{-ik_z z} - k_r A^+ e^{ik_z z} \\ & + i\kappa_z B^- e^{-i\kappa_z z} - i\kappa_z B^+ e^{i\kappa_z z} \Big\} J_1(k_r r) k_r dk_r \end{aligned} \tag{2.47}$$

and for the vertical particle displacement given in [18, p. 241], as in equation (2.48),

$$\begin{aligned} u_z(r,z) = \int_0^\infty \Big\{ & -ik_z A^- e^{-ik_z z} + ik_z A^+ e^{ik_z z} \\ & + k_r B^- e^{-i\kappa_z z} + k_r B^+ e^{i\kappa_z z} \Big\} J_0(k_r r) k_r dk_r. \end{aligned} \tag{2.48}$$

From combining the results for the integral displacements in equations (2.47) and (2.48) with Hooke's law[5], we get expressions for normal stress, σ_{zz}[6], given in [18, p. 241], as in equation (2.49),

[5] It may be an important notice that the Hooke's law used here, is limited to isotropic, homogeneous, fully elastic solid media [26].

[6] In equation 4.38 in [18, p. 241], the exponential for B^+ is written as '$e^i i\kappa_z z$', which we assume is a spelling mistake. Hence we write '$e^{i\kappa_z z}$' in equation (2.49) instead.

$$\begin{aligned}\sigma_{zz}(r,z) &= \left(\lambda+2\mu\right)\frac{\partial u_z}{\partial z}+\lambda\frac{\partial u_r}{\partial r}\\ &= \mu\int_0^\infty\left\{\left(2k_r^2-\kappa_m^2\right)\left[A^-e^{-ik_zz}+A^+e^{ik_zz}\right]\right.\\ &\qquad\left.-2ik_r\kappa_z\left[B^-e^{-i\kappa_zz}-B^+e^{i\kappa_zz}\right]\right\}J_0(k_rr)k_rdk_r\end{aligned}\tag{2.49}$$

and shear stress, σ_{rz}, given in [18, p. 241], as in equation (2.50),

$$\begin{aligned}\sigma_{rz}(r,z) &= \mu\left(\frac{\partial u_r}{\partial z}+\frac{\partial u_z}{\partial z}\right)\\ &= \mu\int_0^\infty\left\{2ik_rk_z\left[A^-e^{-ik_zz}-A^+e^{ik_zz}\right]\right.\\ &\qquad\left.-\left(2k_r^2-\kappa_m^2\right)\left[B^-e^{-i\kappa_zz}+B^+e^{i\kappa_zz}\right]\right\}J_1(k_rr)k_rdk_r\end{aligned}\tag{2.50}$$

Harkrider [35] presents several integral representations for sources which might exist in an elastic medium. For a compressional point source, only the compressional potential ϕ is involved, with the integral representation given in [18, p. 241], as in equation (2.51)

$$\widehat{\phi}(r,z)=\frac{S_\omega}{4\pi}\int_0^\infty\frac{e^{ik_z|z-z_s|}}{ik_z}J_0(k_rr)k_rdk_r.\tag{2.51}$$

The corresponding displacement and stresses follow from equation (2.37) and equation (2.38) combined with Hooke's law [18, p. 241], given in [18, pp. 241–242], as in equations (2.52), (2.53), (2.54) and (2.55),

$$\widehat{u}_r(r,z)=-\frac{S_\omega}{4\pi}\int_0^\infty\frac{k_re^{ik_z|z-z_s|}}{ik_z}J_1(k_rr)k_rdk_r,\tag{2.52}$$

$$\widehat{u}_z(r,z)=\frac{S_\omega}{4\pi}\int_0^\infty\operatorname{sign}(z-z_s)e^{ik_z|z-z_s|}J_0(k_rr)k_rdk_r,\tag{2.53}$$

$$\widehat{\sigma}_{zz}(r,z)=\frac{S_\omega\mu}{4\pi}\int_0^\infty\left(2k_r^2-\kappa_m^2\right)\frac{e^{ik_z|z-z_s|}}{ik_z}J_0(k_rr)k_rdk_r,\tag{2.54}$$

$$\widehat{\sigma}_{rz}(r,z)=-\frac{S_\omega\mu}{4\pi}\int_0^\infty2k\operatorname{sign}(z-z_s)e^{ik_z|z-z_s|}J_1(k_rr)k_rdk_r.\tag{2.55}$$

As we see from equations (2.52), (2.53), (2.54) and (2.55), all the equations are dependent on the frequency dependent source strength S_ω. And for the vertical particle displacement in equation (2.53) and the tangential stress in equation (2.55), the *sign-function*[7] is intro-

[7] It is not clear how Jensen et.al. [18] define the sign-function here. For angular frequency ω, [33] defines the

duced.

2.6 Reflection and transmission - an omnidirectional point source in fluid halfspace

Consider the simple model of homogeneous fluid-seabed halfspaces in cylindrical coordinates, separated by the radial r-axis, where the seabed is approximated to be a fluid. Let an omnidirectional point source with source strength, S_ω, located at z_s on the z-axis in the water halfspace, as in figure 2.4. We can then express the wavenumber kernel for the field

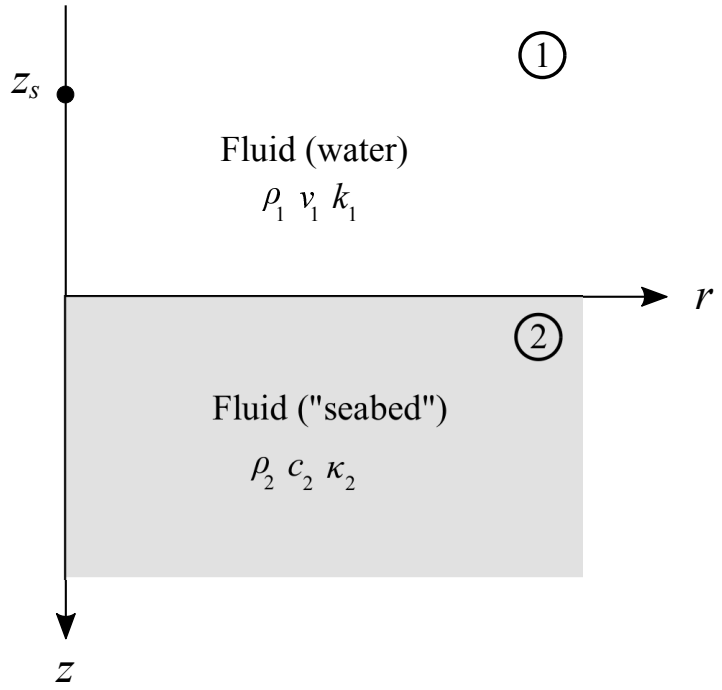

Figure 2.4: Two halfspaces (1 and 2) in cylindrical coordinates with angular symmetry, i.e. $\underline{r} = (r,z)$. Halfspace 1: fluid (water) halfspace with density ρ_1, medium velocity v_1 and medium wavenumber $k_1 = \omega/v_1$. Halfspace 2: fluid ("seabed") halfspace with density ρ_2, medium velocity c_2 and medium wavenumber κ_2. A point source with source strength, S_ω, is located on the z-axis in halfspace 1 at z_s. Modified from [18, fig. 2.8].

in terms of the Green's function in equation (2.24), satisfying the boundary conditions for fluid-fluid interface in table 2.1, with the depth-dependent Green's function ($G_\omega(k_r,z,z_s)$) in equation (2.25) as a superposition of the free-field Green's function ($g_\omega(k_r,z,z_s)$) in equation (2.35) for the point source, and the homogeneous solution to equation (2.27) [18, p. 93].

From the radiation condition in equation (2.31), the homogeneous solution in the upper

sign-function as: $\text{sign}(\omega) = \begin{cases} 1\,, & \omega > 0 \\ 0\,, & \omega = 0 \\ -1\,, & \omega < 0 \end{cases}$. Hence for $z, z_s \geqslant 0$; $\text{sign}(z - z_s) = \begin{cases} 1\,, & z > z_s \\ 0\,, & z = z_s \\ -1\,, & z < z_s \end{cases}$ may be defined by substituting for ω.

halfspace with wavenumber $k_1 = \omega/v_1$ and density ρ_1, is given in [18, p. 94], as in equation (2.56),

$$H_{\omega,1}(k_r, z) = A_1^-(k_r)e^{-ik_{z,1}r} \tag{2.56}$$

For the lower fluid halfspace with wavenumber $\kappa_2 = \omega/c_2$ and density ρ_2, the radiation condition results in equation (2.57),

$$H_{\omega,2}(k_r, z) = A_2^+(k_r)e^{i\kappa_{z,2}z} \tag{2.57}$$

where $k_{z,1}$ and $\kappa_{z,2}$ are the vertical z-wavenumbers for the two media, respectively. To yield the total Green's function in the upper halfspace, the free-field Green's function in equation (2.58) must hold [18, p. 77],

$$g_\omega(r, r_0) = \frac{e^{ik|r-r_0|}}{4\pi|r-r_0|} \tag{2.58}$$

where r_0 is the radial position of the point source. The amplitudes A_1^- and A_2^+ for the homogeneous solutions in equations (2.56) and (2.57), can now be determined by boundary conditions.

The first boundary condition for fluid-fluid interface, *continuity of vertical particle displacements at the boundary*, can in wavenumber space be expressed [18, p. 94] as in equation (2.59),

$$\frac{\partial\Psi_1(k_r, z)}{\partial z} = \frac{\partial\Psi_2(k_r, z)}{\partial z}, \qquad z = 0. \tag{2.59}$$

By replacing $\Psi_i(k_r, z)$, $i = 1, 2$, with the Green's functions (defined in equation (2.25)), inserting for the two homogeneous solutions (2.56) and (2.57), and include the free-field depth-dependent Green's function given in equation (2.35), for $z = 0$ we obtain [18, p. 94] the solution in equation (2.60),

$$\kappa_{z,2}A_2^+(k_r) + k_{z,1}A_1^-(k_r) = k_{z,1}g_{\omega,1}(k_r, 0, z_s) \tag{2.60}$$

The second boundary condition for fluid-fluid interface, *continuity of pressure at the boundary*, results in [18, p. 94] equation (2.61).

$$\rho_1\Psi_1(k_r, z) = \rho_2\Psi_2(k_r, z), \qquad z = 0. \tag{2.61}$$

By inserting the result in equation (2.61) to the Green's function for the two media, for $z = 0$ [18, p. 94] we get equation (2.62),

$$\rho_2 A_2^+ - \rho_1 A_1^- = \rho_1 g_{\omega,1}(k_r, 0, z_s). \tag{2.62}$$

From the solutions in equations (2.60) and (2.62), the amplitude for longitudinal waves' amplitudes with decreasing z-value in layer 1, can be defined [18, p. 94] as in equation (2.63),

$$A_1^- = \frac{\rho_2 k_{z,1} - \rho_1 \kappa_{z,2}}{\rho_2 k_{z,1} + \rho_1 \kappa_{z,2}} g_{\omega,1}(k_r, 0, z_s) \tag{2.63}$$

and for the amplitude for longitudinal waves' amplitudes with decreasing z-value in layer 2, can be defined [18, p. 94] as in equation (2.64),

$$A_2^+ = \frac{2\rho_1 k_{z,1}}{\rho_2 k_{z,1} + \rho_1 \kappa_{z,2}} g_{\omega,1}(k_r, 0, z_s) \tag{2.64}$$

From equations (2.63) and (2.64), the reflection coefficient, R, and the transmission coefficient, T, can be directly seen. Jensen et.al. [18] states that

> Since the wavenumber representation in a Cartesian coordinate system represents a decomposition into plane-wave solutions, $g_\omega(k_r, 0, z)$ represents the complex amplitude at $z = 0$ of plane waves incident from above, and A_1^- and A_2^+ represent the amplitudes of the reflected and transmitted plane waves, respectively. Therefore, the fractions in (ref. equation (2.63)) and (ref. equation (2.64)) are directly the reflection coefficient R and transmission coefficient T for the displacement potential,
>
> Jensen et.al. [18, p. 95]

The reflection coefficient, R, and the transmission coefficient, T, for displacement potentials, can therefore be defined [18, p. 95] as in equations (2.65) and (2.66), respectively,

$$R = \frac{\rho_2 k_{z,1} - \rho_1 \kappa_{z,2}}{\rho_2 k_{z,1} + \rho_1 \kappa_{z,2}} \tag{2.65}$$

and

$$T = \frac{2\rho_1 k_{z,1}}{\rho_2 k_{z,1} + \rho_1 \kappa_{z,2}} \tag{2.66}$$

From equations (2.65) and (2.66), if halfspace 1 and 2 are identical, i.e. $k_1 = \kappa_2$ and $\rho_1 = \rho_2$, then $R = 0$ and $T = 0$, as expected. If the upper halfspace medium is fluid and the lower medium is vacuum (also called free surface), i.e. for $\rho_2 = 0$ and letting $\kappa_2 = \omega / c_2 \to \infty$, then $R = -1$ and $T = 0$. For other media relevant for ocean seismic, Jensen et.al. [18] states that we distinguish between *hard seabed*, $c_2 > v_1$ and *soft seabed*, $c_2 < v_1$ [18, p. 95].

2.6.1 Reflection coefficient for hard seabed

If we consider *hard seabed*, the seabed wavenumber is smaller than of water, i.e. $\kappa_2 < k_1$. Three different spectral regimes for the horizontal wavenumber space are therefore of interest [18, pp. 95-97], also shown in figure 2.5,

- $k_r < \kappa_2$: waves propagating vertically in both media and energy will be transmitted into the bottom: $|R| < 1$.
- $\kappa_2 < k_r < k_1$: waves are propagating in the upper halfspace (water), but are evanescent in the lower halfspace (seabed): $|R| = 1$.
- $k_1 < k_r$: waves are evanescent in both media: $|R| < 1$.

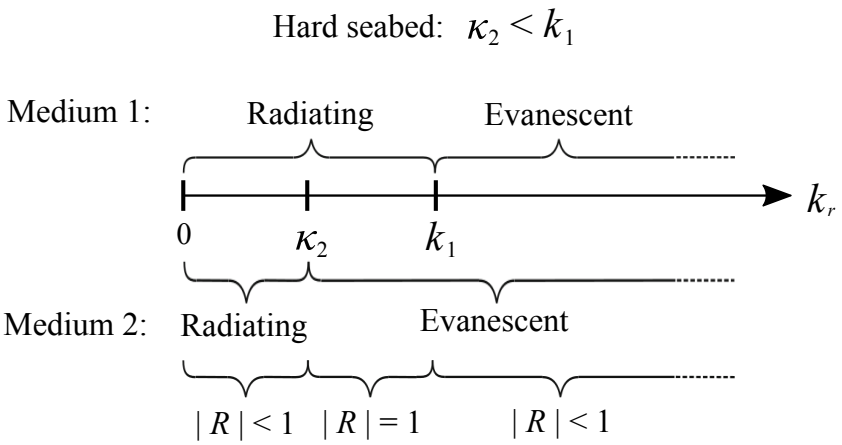

Figure 2.5: Spectral domain for hard seabed, $\kappa_2 < k_1$. Modified from [18, p. 96].

Jensen et.al. [18] states that for the three regimes of interest, the transmission coefficient will always be non-vanishing, i.e. $T > 0$. This is explained by the fact that "there will exist a non-vanishing evanescent field in the bottom (ref. seabed), a feature which becomes significant for multilayered bottoms" [18, p. 96]. Jensen et.al. [18] also notices that for the simple halfspace problem, as in figure 2.4, the reflection and transmission coefficients are independent of angular frequency ω [18, p. 96].

2.6.2 Reflection coefficient for soft seabed

If we consider *soft seabed*, the seabed wavenumber is larger than of water, i.e. $\kappa_2 > k_1$. The three different regimes of interest are [18, pp. 97-98], also shown in figure 2.6,

- $k_r < k_1$: waves are propagating vertically in both media and energy will be transmitted into the bottom: $|R| < 1$.

- $k_1 < k_r < \kappa_2$: waves are evanescent in the upper halfspace (water), but propagating in the lower halfspace (seabed): $|R| = 1$.
- $\kappa_2 < k_r$: waves are evanescent in depth in both media: $|R| < 1$.

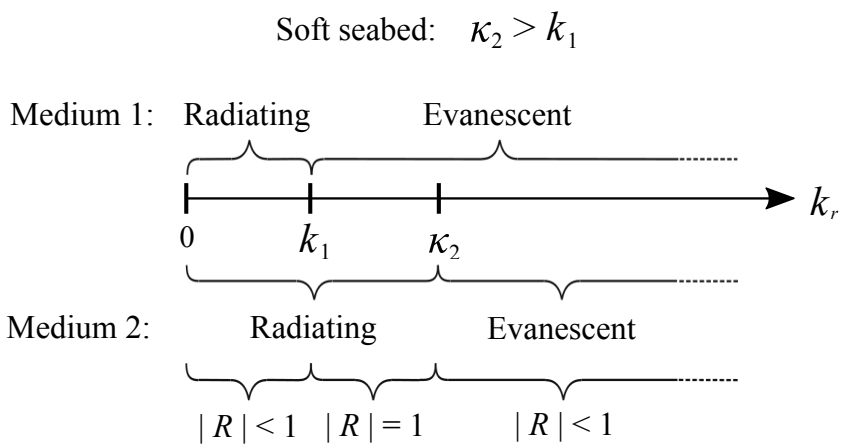

Figure 2.6: Spectral domain for soft seabed, $\kappa_2 > k_1$. Modified from [18, p. 97].

The reflection coefficient can be defined in terms of magnitude and phase [18, p. 96], as in equation (2.67),

$$R(\theta) = |R(\theta)|e^{-i\phi(\theta)} \tag{2.67}$$

where ϕ is a phase angle and θ is the *grazing angle of incidence*, defined as $\theta = \arccos(k_r/k_1)$, which only makes sense for $k_{z,1}$ real. But for evanescent waves, the grazing angle passes the so-called *critical angle*, defined as $\theta_c = \arccos(\kappa_2/k_1)$, and the transmitted angle become complex. Hence, defining the reflection coefficient with angles (which must be real to make sense), should be avoided when investigating evanescent waves.

2.7 Stratified and depth-dependent air-water-seabed layered model in cylindrical coordinates; pressure and particle velocity equations for evanescent waves in water

2.7.1 Pressure equations in the water layer

In a stratified depth-dependent air-water-seabed layered model in cylindrical coordinates (as in figure 2.7), only pressure waves can exist in the water layer [1]. In the seabed (which could be approximated as a solid), both compressional-, shear vertical- and shear horizontal waves may exist. This complicates the mathematical derivation, since we have to consider

interactions at boundaries where several boundary conditions must yield simultaneously at three different interfaces.

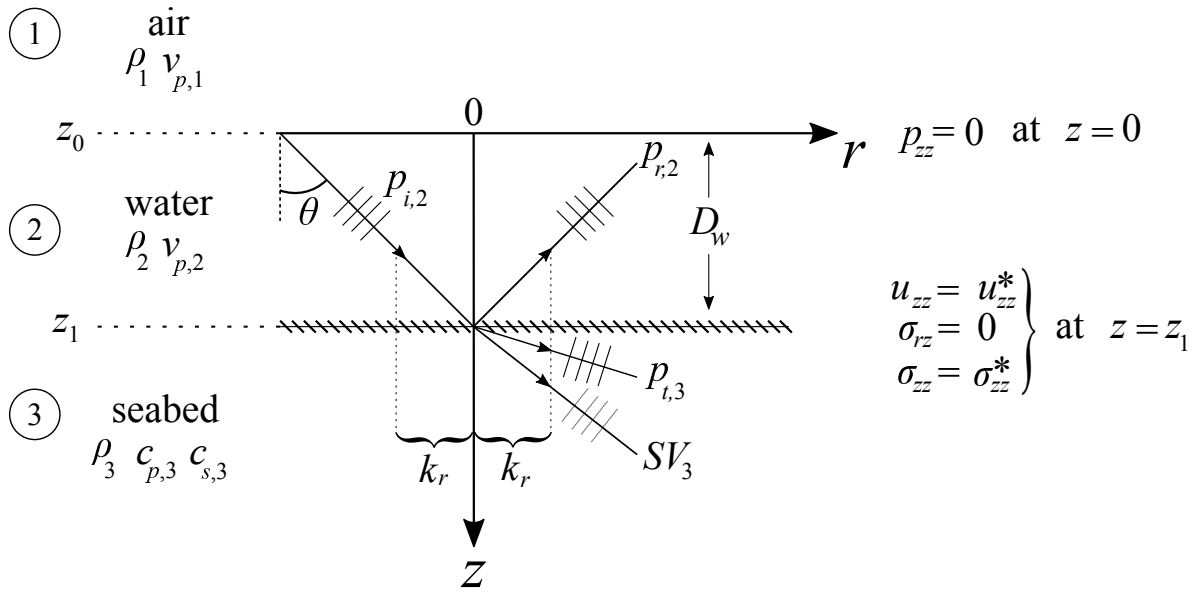

Figure 2.7: Air-water-seabed layered model in cylindrical coordinates, with angular symmetry, i.e. $\varphi = 1$, $\underline{r} = (r, z)$. The incident plane pressure wave in layer 2, $p_{i,2}$, hit a water-seabed interface at depth $z = z_1$ with boundary conditions for fluid-solid interfaces. The incident plane wave can then be reflected to a plane pressure wave propagating in layer 2, $p_{r,2}$, and/or transmitted to two waves; one compressional wave, $p_{t,3}$, and one shear vertical wave, SV_3, both propagating in layer 3. The reflected plane pressure wave can then hit the water-air interface at $z = z_0 = 0$ with boundary conditions for fluid-vacuum interfaces. Layer 1 (air): density, ρ_1, and pressure phase velocity, $v_{p,1}$. Layer 2 (water): density, ρ_2, pressure phase velocity, $v_{p,2}$, and water thickness, D_w. Layer 3 (seabed): density, ρ_3, compressional phase velocity, $c_{p,3}$, and shear vertical phase velocity, $c_{s,3}$. $z = z_0$ is the depth at the water-air interface and $z = z_1$ is the depth at the water-seabed interface. θ is the incident angle from the vertical, and k_r is the horizontal wavenumber. With inspiration from [36] and [27, pp. 5.56–5.70b].

Ignoring the seabed (3) in figure 2.7, the pressure wave in water, p_2, can be associated with the sum of two plane pressure waves; one propagating downwards, $p_{i,2}$, and one propagating upwards, $p_{r,2}$, [1] as in equation (2.68),

$$p_2 = p_{i,2} + p_{r,2}. \tag{2.68}$$

The downward propagating plane pressure wave could be expressed as a plane wave solution given in equation (2.69),

$$p_{i,2} = A_d e^{i(k_r r + k_{z,2} z - \omega t)} \tag{2.69}$$

and the upward propagating plane pressure wave could be expressed as a plane wave solution given in equation (2.70),

$$p_{r,2} = A_u e^{i(k_r r - k_{z,2} z - \omega t)}. \tag{2.70}$$

The resulting total pressure in water, could then be given as the sum of the two plane waves, given in equation (2.71),

$$p_2 = A_d e^{i(k_r r + k_{z,2} z - \omega t)} + A_u e^{i(k_r r - k_{z,2} z - \omega t)}. \tag{2.71}$$

which is in consistent with the derivation given in [1]. As we see in equation (2.71), the total pressure is defined using the radial- and vertical wavenumbers i water, k_r and $k_{z,2}$, respectively. Since the shear horizontal waves do not couple with the compressional- and the shear vertical waves for our boundary conditions [36] [1], we leave out the shear horizontal waves here. It can be shown that for plane pressure waves fluid-solid interfaces, using the respective boundary conditions yield that the horizontal wavenumbers are equal [27, pp. 5.67].

For a plane wavefront with incident angle, θ, from the vertical, we can apply basic trigonometry in figure 2.7 to define the radial wavenumber i water given in equation (2.72),

$$k_r = \frac{\omega}{v_r} \sin\theta \tag{2.72}$$

and the vertical wavenumber in water given in equation (2.73),

$$k_{z,2} = \frac{\omega}{v_{z,2}} \cos\theta \tag{2.73}$$

where the water wavenumber (i.e. the *dispersion relation*) in water is defined in equation (2.74),

$$k^2 = \left(\frac{\omega}{v}\right)^2 \equiv k_r^2 + k_{z,2}^2. \tag{2.74}$$

By inserting for equations (2.72) and (2.73) into equation (2.71), we get an expression for the total plane pressure wave in water, based on trigonometry, given in equation (2.75),

$$\begin{aligned} p_2\left(\theta, v_{z,2}, z\right) &= A_d e^{i\omega\left(\frac{\sin\theta}{v_r} r + \frac{\cos\theta}{v_{z,2}} z - t\right)} + A_u e^{i\omega\left(\frac{\sin\theta}{v_r} r - \frac{\cos\theta}{v_{z,2}} z - t\right)} \\ &= \left[A_d e^{i\omega\frac{\cos\theta}{v_{z,2}} z} + A_u e^{-i\omega\frac{\cos\theta}{v_{z,2}} z}\right] e^{i\left(\omega\frac{\sin\theta}{v_r} r - \omega t\right)} \end{aligned} \tag{2.75}$$

We can then insert again for equations (2.72) and (2.73), into equation (2.75) and get the equation for the total plane pressure wave in water, based on the horizontal- and vertical wavenumber components, given in equation (2.76),

$$p_2\left(k_{z,2}, z\right) = \left[A_d e^{ik_{z,2} z} + A_u e^{-ik_{z,2} z}\right] e^{i(k_r r - \omega t)} \tag{2.76}$$

The vertical wavenumber, $k_z = \pm\sqrt{k^2 - k_r^2}$, is defined in equation (2.29) for two conditions, resulting in *propagating*- and *evanescent modes* [37, ch. 2.9]. Using equation (2.29) for $k_r \leqslant k$ (i.e. resulting in propagating modes), we can use equation (2.76) to define the plane pressure wave equation for propagating waves in water, $p_{p,2}$, given in equation (2.77),

$$p_{p,2}(k_r, z) = \left[A_d e^{i\sqrt{k^2-k_r^2}z} + A_u e^{-i\sqrt{k^2-k_r^2}z} \right] e^{i(k_r r - \omega t)}, \qquad k_r \leqslant k \tag{2.77}$$

And, by using equation (2.29) for $k_r > k$ (i.e. resulting in evanescent modes), we can use equation (2.76) to define the plane pressure wave equation for evanescent waves in water, $p_{e,2}$, given in equation (2.78),

$$p_{e,2}(k_r, z) = \left[A_d e^{-\sqrt{k_r^2-k^2}z} + A_u e^{\sqrt{k_r^2-k^2}z} \right] e^{i(k_r r - \omega t)}, \qquad k_r > k \tag{2.78}$$

From equations (2.77) and (2.78), we see that the total pressures for both propagating and evanescent waves in water are still sums of two plane waves; one propagating upwards, and one propagating downwards, both with opposite z-values.

The surface condition for the fluid-vacuum (i.e. water-air) boundary, could be found in table 2.1. The surface condition for fluid-vacuum boundaries yields $p = 0$ at $z = 0$ [1]. Applying this boundary condition to equations (2.77) and (2.78), yield that the amplitudes for the two respective plane waves must satisfy the condition given in equation (2.79),

$$A_u = -A_d. \tag{2.79}$$

Johansen & Ruud [1] states that by analyzing Scholte waves in water, the vertical wavenumber, $k_{z,2} = \omega / v_{z,2}$, is complex since the shear wave velocity is much less than the pressure velocity in water. Consequently, only the pressure wave equation for evanescent plane waves in equation (2.78), resulting in equation (2.80) is of interest [1].

By inserting for the condition in equation (2.79) into equation (2.78), we get the pressure wave equation for plane evanescent waves in water given in equation (2.80),

$$\begin{aligned} p_{e,2}(k_r, z) &= A_d \left[e^{-\sqrt{k_r^2-k^2}z} - e^{\sqrt{k_r^2-k^2}z} \right] e^{i(k_r r - \omega t)}, \qquad k_r > k \\ &= -2A_d \sinh\left(\sqrt{k_r^2 - k^2}\, z \right) e^{i(k_r r - \omega t)} \\ &= 2A_d \sinh\left(-\sqrt{k_r^2 - k^2}\, z \right) e^{i(k_r r - \omega t)} \\ &= \left| p_{e,2}(k_r, z) \right| e^{i(k_r r - \omega t)} \end{aligned} \tag{2.80}$$

for amplitudes given by the radial- (k_r) and water (k) wavenumbers.

We see from equations (2.80) that the pressure amplitudes for evanescent plane waves could be described either by exponentials, or sine, or hyperbolic sine functions, e.g. having the properties given in [38, ch. 3.6] as $i\sin(x) = \sinh(ix)$ and $\sinh(-x) = -\sinh(x)$. We also see that the total pressure for the evanescent plane waves in water are the sum of pressures from two evanescent plane waves; one decaying upwards and one decaying downwards.

2.7.2 Vertical particle velocity equations in water

The vertical particle velocity in water, $v_{z,2}$, can be computed from the pressure relation given in [5], as in equation (2.81),

$$v_z = \frac{1}{i\omega\rho_2}\frac{\partial p_2}{\partial z}. \tag{2.81}$$

where ρ_2 is the density of water ($\rho_2 \approx 1030$ kg/m^3). Inserting for the boundary condition in equation (2.79) into equation (2.76), and differentiate the result with dz, we can use equation (2.81) to get the equation for vertical particle velocity in water, given as function of the vertical wavenumber, $k_{z,2}$, in equation (2.82),

$$\begin{aligned} v_{z,2}\big(k_{z,2},z\big) &= \frac{k_{z,2}}{\omega\rho_2}A_d\left[e^{ik_{z,2}z} + e^{-ik_{z,2}z}\right]e^{i(k_r r-\omega t)} \\ &= \frac{k_{z,2}}{\omega\rho_2}2A_d\cos(k_{z,2}z)e^{i(k_r r-\omega t)} \\ &= \left|v_{z,2}\big(k_{z,2},z\big)\right|e^{i(k_r r-\omega t)} \end{aligned} \tag{2.82}$$

By inserting for the vertical wavenumber for evanescent conditions, $k_{z,2} = i\sqrt{k_r^2 - k^2}$, we get the equation for vertical particle velocity in water for evanescent waves, given as function of the horizontal wavenumber, k_r, in equation (2.83),

$$\begin{aligned} v_{z,e}\big(k_r,z\big) &= i\frac{\sqrt{k_r^2-k^2}}{\omega\rho_2}A_d\left[e^{-\sqrt{k_r^2-k^2}z} + e^{\sqrt{k_r^2-k^2}z}\right]e^{i(k_r r-\omega t)}, \qquad k_r > k \\ &= i\frac{\sqrt{k_r^2-k^2}}{\omega\rho_2}2A_d\cosh\left(\sqrt{k_r^2-k^2}z\right)e^{i(k_r r-\omega t)} \\ &= \left|v_{z,e}(k_r,k)\right|e^{i(k_r r-\omega t)} \end{aligned} \tag{2.83}$$

By comparing equation (2.83) to the corresponding expression for plane evanescent pressure waves in water, given in equation (2.80), we note a 90° phase difference between the pressure and the vertical particle velocity for evanescent plane waves in water.

2.8 Surface acoustic Scholte waves

Zhu & Popovics [39] state that surface acoustic Scholte waves always exist for any combination of fluid-solid interfaces. Vinh [12] has deduced that if Scholte waves exists, then it is unique, "and for any given parameters of the solid and the fluid, a Scholte wave is always possible" [12]. Foti et.al. [40] states that for Scholte waves propagating along the boundary separating a fluid and a solid in a 2D two-layered case, most of the energy travel at the fluid-solid interface. For instance, is this behavior similar to Rayleigh waves at the solid-vacuum interface and Stonely waves at the solid-solid interface [41]. Taking this into account, we have shown in equation (2.80) that for plane evanescent Scholte waves, the pressure amplitudes decay exponentially with distance from the seabed. Moreover, Johansen et.al. [1] states that in shallow waters, the resulting amplitudes are modulated by interference with the surface.

Along the seabed, where an interface separates a fluid and a solid, two types of guided waves may exist, i.e. Leaky Rayleigh and Scholte waves. While Scholte waves may always exist, Leaky Rayleigh waves may only occur when the shear velocity of the seabed ($c_{s,3}$) is larger than the acoustic velocity in water ($v_{p,2}$) [4]. In our experiments, the upper seabed sediments are very loose, which implies that $c_{s,3} << v_{p,2}$, and we only need to consider the phase velocity of the Scholte wave (v_{Sc}) [1].

By assuming an isotropic elastic solid occupying a lower halfspace, and a non-viscous fluid occupy the upper halfspace, [12] have deduced an expression for the phase velocity of the Scholte wave, given in equation (2.84),

$$r\,x^2\sqrt{1-\beta x}+(2-x)^2\sqrt{1-\beta^* x}-4\sqrt{1-x}\sqrt{1-\beta x}\sqrt{1-\beta^* x}=0 \tag{2.84}$$

where

$$x=\frac{v_{Sc}^2}{c_{s,3}^2},\quad \beta=\frac{c_{s,3}^2}{c_{p,3}^2},\quad \beta^*=\frac{c_{s,3}^2}{v_{p,2}^2},\quad r=\frac{\rho_2}{\rho_3} \tag{2.85}$$

In equation (2.85), $c_{p,3}$ is the compressional velocity of the sediment, and ρ_2 and ρ_3 are the densities of water and sediment, respectively. Inserting for x, β, β^* and r in equation (2.85) into equation (2.84) yields the equation (2.86),

$$\begin{aligned}\frac{\rho_2}{\rho_3}\left(\frac{v_{Sc}}{c_{s,3}}\right)^2\sqrt{1-\left(\frac{v_{Sc}}{c_{p,3}}\right)^2}+\left(2-\left(\frac{v_{Sc}}{c_{s,3}}\right)^2\right)^2\sqrt{1-\left(\frac{v_{Sc}}{c_{p,3}}\right)^2}\\ -4\sqrt{1-\left(\frac{v_{Sc}}{c_{s,3}}\right)^2}\sqrt{1-\left(\frac{v_{Sc}}{c_{p,3}}\right)^2}\sqrt{1-\left(\frac{v_{Sc}}{v_{p,2}}\right)^2}=0\end{aligned} \tag{2.86}$$

From equation (2.86), we see that by knowing the mechanical parameters; ρ_2, ρ_3, $c_{s,3}$, $c_{p,3}$ and $v_{p,2}$, we can solve for the phase velocity of the Scholte wave v_{Sc}. For example by inserting for $\rho_2 = 1030$ kg/m^3, $\rho_3 = 1217$ kg/m^3, $c_{s,3} = 44$ m/s, $c_{p,3} = 1600$ m/s and $v_{p,2} = 1500$ m/s (as

in layers 4 and 5 in table 5.1) into equation (2.86), we calculate the phase velocity of the Scholte wave $v_{Sc} \approx 35.6$ m/s (calculated using [42]). Johansen et.al. [4] states that often, $v_{Sc} = 0.9\ c_{s,3}$ is a good approximation, which in our example of $v_{s,3} = 44$ m/s, would yield: $v_{Sc} = 0.9 \cdot 44$ m/s $= 39.6$ m/s; a deviation of 4 m/s from the calculated Scholte wave velocity using equation (2.86).

2.8.1 Skin depth

In analogy to the *radial slowness*, which can be defined as $p = 1/v_r$ [1], the *skin depth* can be defined as in equation (2.87),

$$\delta = \frac{1}{\omega p} = \frac{1}{k_r} = \frac{v_r}{\omega} \tag{2.87}$$

for radial wavenumber, k_r, or radial phase velocity, v_r, where $k_r = \omega / v_r$. For evanescent waves, the skin depth can describe the variation with depth at which the wave's amplitude is reduced by a factor $e^{-1} \approx 0.37$. For instance, for a Scholte wave with frequency 4 Hz and radial phase velocity 100 m/s, the skin depth is about 4.0 m [1]. This means that for a Scholte wave in deep water, the amplitude (e.g. pressure, displacement, or particle velocity) will at 4.0 m above the seabed decay exponentially upwards and be reduced by 37 % of the amplitude at the seabed [1]. For the same Scholte wave frequency of 4 Hz, with phase velocity 150 m/s, the skin depth is about 6.0 m.

Johansen & Ruud [1, fig. 3] have demonstrated the depth dependence of pressure and vertical particle velocity motion as a function of normalized skin depth in a water layer with phase velocity much lower than the acoustic velocity in water. They find that for depths less than the skin depth,

> the total pressure increases almost linearly with depth, while for depth larger than two times the skin depth, the 'surface reflection' can be ignored and the water layer can be considered as a halfspace with regard to Scholte wave propagation.
>
> Johansen & Ruud [1, p. 52].

This means that if we are to consider the water layer as a halfspace, by using equation (2.87) with $D_w > 2\delta$ and water thicknesses $D_{w,1} = 19.1$ m and $D_{w,2} = 31.2$ m (used when modeling in OASES in chapter 5), the radial wavenumbers should therefore be larger than $k_{r,1} > 0.105$ rad/m and $k_{r,2} > 0.064$ rad/m, respectively. [1] also note that

> the two P waves add constructively for particle motion at the free surface while the pressure waves cancel out. Thus, it is possible to record the Scholte waves

> with vertical geophones placed at the surface of a thin ice layer, (...). For water depths much less than the skin depth, we note that the depth dependence is almost constant. Therefore, a thin water layer (compared to skin depth) can be ignored when considering vertical particle velocity or displacement, and the wave could rather be called a Rayleigh wave. However, one must keep in mind that the skin depth is a frequency-dependent variable (inversely proportional to both frequency and horizontal slowness, which may also vary with frequency), so that the effect of a water layer will become more noticeable as the frequency increases.
>
> Johansen & Ruud [1, pp. 51–52]

This means that for shallow water seismic, e.g. large wavelengths and thin water layers compared to the skin depth, Scholte waves generated at the seabed could be recorded by geophones placed on top of thin floating sea ice.

2.9 Group and phase velocity

When analyzing dispersive surface waves, the concept of phase and group velocity is helpful. We follow a description from Pujol [33], chapter 7.6.2, on a general approach to the theory behind phase and group velocity.

Assume $\omega = \omega(k)$, where $k = \omega / v_{ph} = 2\pi f / v_{ph}$ is the radial wavenumber with phase velocity v_{ph} and frequency f. We now let $f(r,t)$ describe an infinite superposition of outward propagating plane waves given in [33, p. 217], as in equation (2.88),

$$f(r,t) = \frac{1}{2\pi} \int_{-\infty}^{\infty} A(k) e^{i(\omega(k)t - k_r r)} dk \tag{2.88}$$

with arbitrary amplitudes $A(k)$. Now, we assume that for small $\delta k > 0$, $A(k)$[8] is zero everywhere except at the interval $(k - \delta k < k < k + \delta k)$. This could be interpreted as superimposing an infinite number of waves with very similar wavenumbers and arbitrary amplitudes, which for instance results in a narrow band in the k-domain, but broad in the r-domain [33, p. 217].

$\omega(k)$ can then be approximated using the first order Taylor expansion of $k \equiv \delta k + (k - \delta k)$, and where $\omega = \delta\omega + (\omega - \delta\omega)$. It can then be shown that the phase in equation (2.88) can be written as in [33, p. 217], as in equation (2.89),

$$\omega(k)t - kr \approx \delta\omega\ t - \delta k\ r + \left(\left. \frac{d\omega}{dk} \right|_{k=\delta k} t - r \right)(k - \delta k). \tag{2.89}$$

[8] In Pujol [33, p. 217], Pujol writes $\omega(k)$ instead of $A(k)$. If $\omega(k)$ is zero everywhere except for that small interval $(k - \delta k < k < k + \delta k)$, then only a small window of the dispersion relation is non-zero. We think Pujol means that $f(x,t)$ is zero everywhere except at that small interval. Hence this might be a typo in [33]. This is also commented in a master thesis by Jensen [21].

Because $\delta\omega$ and δk are constants, $f(r,t)$ can be written as in [33, p. 217], as in equation (2.90),

$$f(r,t) = \frac{1}{2\pi}\int_{\delta k-\delta k^*}^{\delta k+\delta k^*} A(k)e^{i(k-\delta k)\left(\frac{d\omega}{dk}\Big|_{k=\delta k}\ t-r\right)}e^{i\left(\frac{d\omega}{dk}\Big|_{k=\delta k}\ t-\delta k\ r\right)}dk \tag{2.90}$$

Pujol [33] writes that the result in equation (2.90) can be seen as a superposition of a "common harmonic wave" [33, p. 217], which for constant phase $\left(\text{i.e.: } \frac{d\omega}{dk}\big|_{k=\delta k}\ t-r = \texttt{constant}\right)$ travels with *group velocity*, U, as in equation (2.91),

$$U = \frac{dr}{dt} = \left.\frac{d\omega}{dk}\right|_{k=\delta k} \tag{2.91}$$

For inversion analysis, we are interested in knowing the *phase velocity*, v_{ph}, of the wave. See for example Johansen et.al. [1] who did an inversion, among others, based on measured group- and phase velocities. Park et.al. [43] have derived a method for calculating the phase velocity of a wave. It is based on separation of variables, where Fourier transforming $f(r,t)$ into $F(r,\omega)$, we can write $F(r,\omega)$ as in equation (2.92),

$$F(r,\omega) = P(r,\omega)A(r,\omega) \tag{2.92}$$

where $P(r,\omega)$ and $A(r,\omega)$ are the phase and amplitude spectra of $F(r,\omega)$, respectively. Park et.al. [43] writes further that since each frequency component in $U(r,\omega)$ is "completely separated form other frequencies and the arrival time information is preserved in phase spectrum" [43, p. 1], then $P(r,\omega)$ contains all the information about dispersion properties and $A(r,\omega)$ contains information about "all other properties such as attenuation and spherical divergence" [43, p. 1]. Hence $F(r,\omega)$ can be written as in [43], as in equation (2.93),

$$F(r,\omega) = e^{-i\Phi r}A(r,\omega), \tag{2.93}$$

where Φ is given in equation (2.94),

$$\Phi = \frac{\omega}{v_{ph}} \tag{2.94}$$

as the wavenumber with angular frequency ω and phase velocity v_{ph}. Park [43] then introduces an integral given as in equation (2.95),

$$\begin{aligned} V(\omega,\phi) &= \int e^{i\phi r}\left[\frac{F(r,\omega)}{|F(r,\omega)|}\right]dr \\ &= \int e^{-i(\Phi-\phi)r}\left[\frac{A(r,\omega)}{|A(r,\omega)|}\right]dr \end{aligned} \tag{2.95}$$

which Park [43] says could be thought of as the "summing over offset of wavefields of a fre-

quency after applying offset-dependent phase shift determined for an assumed phase velocity" [43, p. 2], given as in equation (2.96)[9],

$$v_{ph} = \frac{\omega}{\phi} \tag{2.96}$$

In figure 2.8 is an illustration of a carrier wave traveling with phase velocity, v_{ph}, modulated by a wave traveling with group velocity, U. When we later present the shot gathers, i.e. ampli-

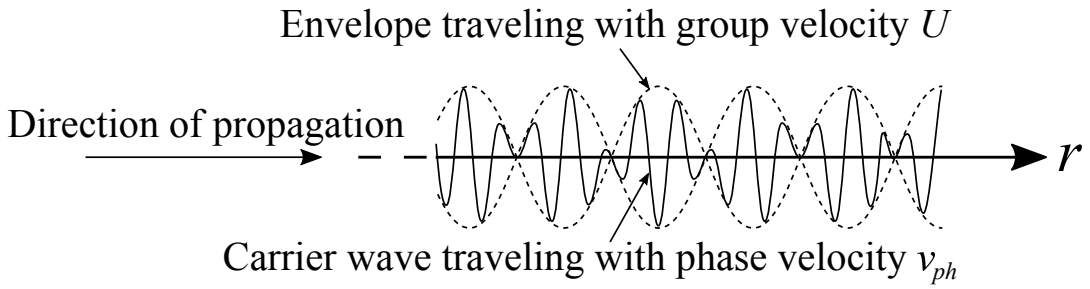

Figure 2.8: Illustration of phase and group velocity when two plane waves traveling in x-direction, interfering due to their differences in angular frequency and wavenumber. The "envelope" (stippled line) travel with group velocity U and the carrier wave (solid line) propagate with phase velocity v. Modified from [21].

tudes for modeled and measured pressure and vertical displacements in the $(r-t)$ domain, we can calculate the slope of the amplitudes in the shot gathers. And by using the relation in equation (2.8), we can calculate the group velocity of the amplitude wave based on the slope. Alternatively, we can use the theory by Park et.al. [43] to calculate the amplitudes as function of frequency, f, and phase velocity, v_{ph}, i.e. the dispersion curve.

2.10 Aliasing in seismic records

By sampling a seismic wave in space and time, both temporal and spatial aliasing effects might occur. Assume a receiver configuration in the (r,z)-plane where we have two receivers, A and B, located on the r-axis and separated in space by $\Delta r > 0$. Next, we assume a monochromatic plane wave with wavelength, λ, propagating towards A and B with incident angle, θ, from the normal, as in figure 2.9. Using trigonometry, we can define the r-component of the wavelength, $\lambda_x = \lambda / \sin(\theta)$, given in equation (2.97),

$$\Delta r = \frac{\lambda_r}{2} = \frac{\pi}{k_r} \tag{2.97}$$

[9] Unfortunately, I do not understand the rest of the derivation in Park et.al. [43], hence I decided not to try to describe an expression for the dispersion curve, noted as "$I(\omega, v_{ph})$" in [43]. By reading the SUPHASEVEL code in [44], did not help either. I think I struggle to understand how $V(\omega,\phi)$ is derived in equation (2.95), and I think more study would be needed to understand this.

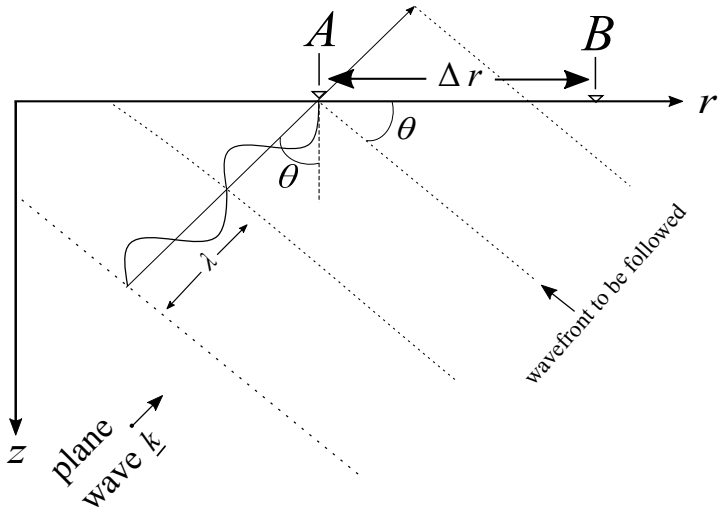

Figure 2.9: Incident monochromatic plane wave with wavelength, λ, wavenumber, $\underline{k}$, and incident angle, θ, from the normal in the (r,z)-plane. Two receivers, A and B, are placed on the r-axis with spacing Δr. We follow the wavefront indicated with an arrow, named "wavefront of interest". With inspiration from [45] and handwritten notes by professor Per Lunde (UiB).

where $k_r = 2\pi/\lambda_r$ is the r-components of the plane wave's wavenumber, $\underline{k}$. The *Nyquist criterion*, given in equation (2.98),

$$\Delta r \geqslant \frac{\lambda_r^{min}}{2} \tag{2.98}$$

where λ_r^{min} is the minimum radial wavelength of the incoming wave, we can use to define the so-called radial *Nyquist wavenumber*, $k_{r,Ny}$ [45], as in equation (2.99),

$$k_{r,Ny} = \frac{\pi}{\Delta r} \tag{2.99}$$

which for radial wavenumbers larger than $k_{r,Ny}$ are spatially aliased. From equation (2.98), we can see that to avoid spatially aliasing effects when measuring Scholte waves, one can design the measurement setup with narrow enough receiver intervals.

In the $(f-k_r)$ domain, at an interval $-k_{r,Ny} \leqslant 0 \leqslant k_{r,Ny}$, spatial aliasing effects result in amplitudes being "wrapped" onto negative wavenumbers [46]. However, Foti et.al. [46] deduce that for surface waves, in the end of the shot gathers, all the energy travels in the positive direction and is associated to positive wavenumbers. Hence, Foti et.al. [46] state that in the $(f-k_r)$ domain, it is possible to recover the aliased information laying in the interval $-k_{r,Ny} \leqslant 0$, by "horizontal unwrapping" to the interval $k_{r,Ny} \leqslant 2k_{r,Ny}$, "without introducing additional noise" [46].

To avoiding temporal aliasing effects in seismic shot gathers, we can use the *Nyquist sampling theorem*, given in equation (2.100),

$$\Delta t \leqslant (\Delta t)_{max} = \frac{T_{min}}{2} = \frac{1}{2f_{max}} \tag{2.100}$$

where Δt is the time between each sampled wave, T_{min} is the minimum period of the wave and f_{max} is the maximum frequency of the wave. For waves with frequency components larger than f_{max}, the waves are temporally aliased. Hence, one should choose a large enough sampling rate to avoid temporal aliasing effects when observation of Scholte waves is of interest.

Chapter 3

Modeling elastic properties of seabed sediments – Differential effective medium (DEM) model

When modeling elastic properties of seabed sediments, one method is the use the so-called *differential effective medium* (DEM) model. The DEM model is a ”thought experiment” [47, p. 205] based on calculating the effective elastic properties of multi-phase media, by incrementally adding inclusion of one phase to a matrix phase [47, ch. 4.9]. For a homogeneous host medium, also called the matrix phase, a water inclusion could be defined as an inhomogeneity embedded in the homogeneous host medium [48]. Johansen [48] states that the effective elastic parameters of such multi-phase medium can be defined as *macro elasticity*, meaning the elastic properties measured over a representative volume of the effective medium.

We will use DEM model based on theory of effective moduli by Kuster & Toksöz [16], to model the macro elastic properties of different water filled silicates. The code for calculating the effective moduli is made by Prof. Tor Arne Johansen (UiB), see appendix A. The DEM code in appendix A, computes the bulk- and shear moduli of the effective medium, by incrementally introducing uniformly-shaped water inclusions to a host medium, e.g. a porous host mineral with water filled pores. Some knowledge about common minerals found in the area of interest might be useful, so that the DEM models are as representative as possible for the actual study area. Next we will present some of the geological compositions and minerals found in and around Van Mijenfjorden, Svalbard.

3.1 Common minerals found in and around Van Mijenfjorden, Svalbard

At Svalbard, the Norwegian Polar institute has made a map of the bedrock geology (see figure 3.1), based on geological studies, seismic surveys, outcrops, well log data, etc., [49]. We see from figure 3.1, that the geology at Svalbard is fairly complex, with vast diversity in geological compositions. In the study area, indicated as a black rectangle in figure 3.1, the discovered geological periods are Paleogene and Neogene (yellow), formed approximately 66 - 2.6 million years ago, and Middle Jurassic - Early Cretaceous (light blue), formed approximately 174.1 - 100.5 million years ago. [50] reported on the composition of sediments in Van Mijenfjorden, and [51] discovered that most of the fjord is located within Paleogene sedimentary bedrock of various types of sandstones (e.g. quartz sandstones), siltstones, shales, coals and coal pebbels. Based on these findings, we chose to model the macro elastic properties using DEM [16], based on water filling some porous silicates with mechanical properties presented in table 3.1,

Table 3.1: Mechanical properties of water and some silicates; clay, silt, quartz sandstone and quartz with clay, composites likely to be found in the area of Van Mijenfjorden, Svalbard [51, 50].

Constituents	Bulk mod. (GPa)	Shear mod. (GPa)	Density (kg/m^3)	v_p (m/s)	v_s (m/s)	References*
Liquid						
Water	2.318	-	1030	1500	-	
Silicates						
Clay	21.0	7.0	2500	3483	1673	a
Silt	37.0	44.0	2650	6008	4075	a
Quartz sandstone	36.6	45.0	2650	6040	4120	b, c, d, e
Quartz with clay (Han)	39.0	33.0	2650	5590	3520	f, e

*a: [1]; b: [52]; c: [53];
d: [54]; e: [47]; f: [55].

The bulk modulus of water, K_w, in table 3.1, is calculated assuming sound pressure velocity in water, $v_{p,w} = 1500$ m/s, and water density, $\rho_w = 1030$ kg/m^3. By using equation (2.2), we can calculate for the water bulk modulus given in equation (3.1),

$$K_w = v_{p,w}^2 \cdot \rho_w = (1500 \text{ m/s})^2 \cdot 1030 \text{ kg/m}^3 = 2.318 \text{ GPa} \tag{3.1}$$

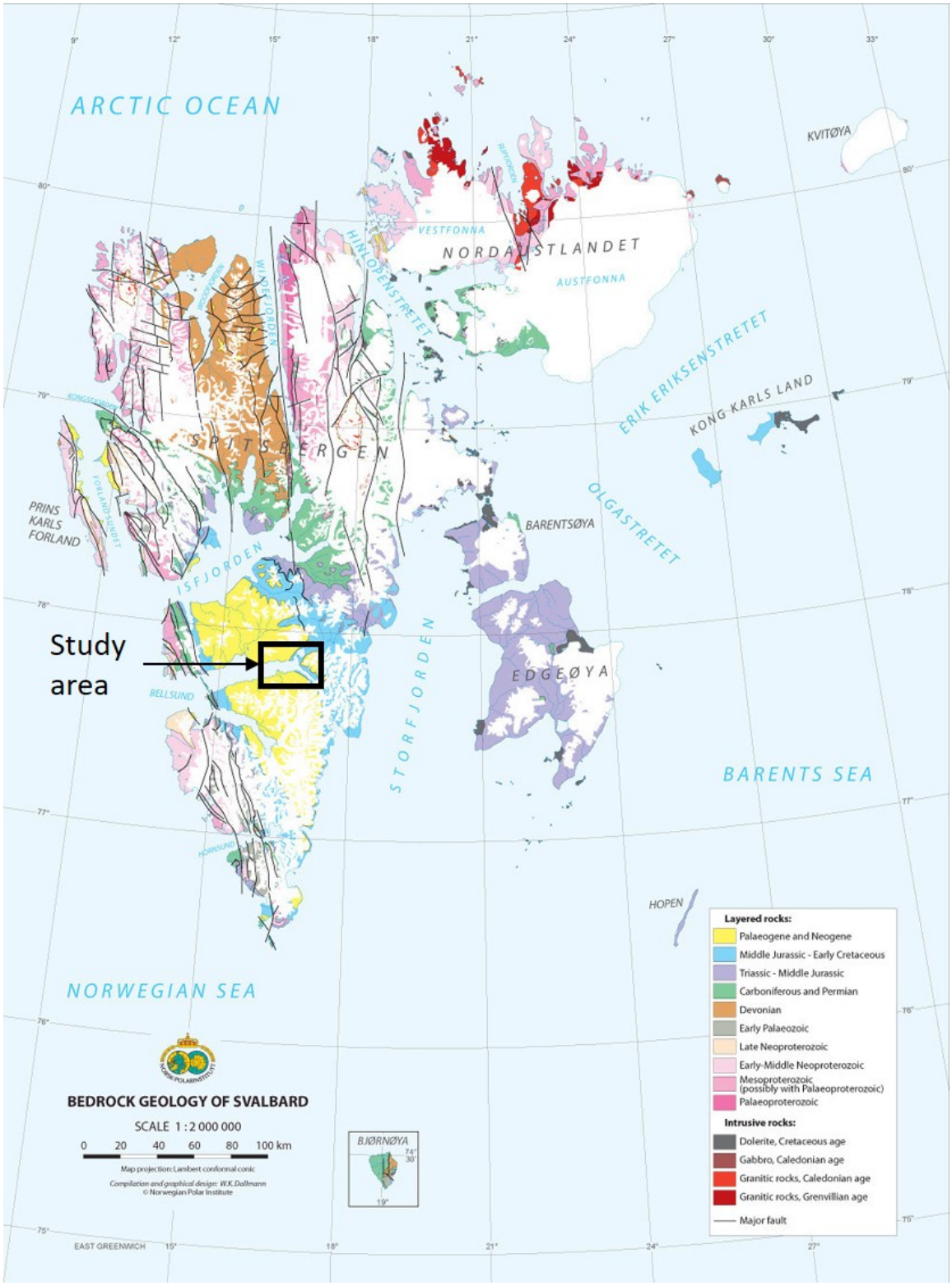

Figure 3.1: Map of Svalbard's bedrock geology, colored after geological periods discovered. The study area (Van Mijenfjorden) is located inside the black rectangle. Modified from © Norwegian Polar Institute [49].

The three mineral silicates in table 3.1; clay, silt and quartz sandstone, are classified after their grain sizes, e.g. following the *ISO 14688-1:2017* standard [56]. Clay is here classified

as minerals with particle diameters < 0.002 mm, silt as minerals with particle diameters between 0.002 mm and 0.06 mm, and sand as minerals with particle diameter of 0.06 mm to 2 mm. Since these minerals are all silicates, mixtures of these minerals may be considered homogeneous.

Some of the macro elastic properties of water filled porous media are poorly understood. For example can solid clay sediments originally deposited in salt water, and later exposed to fresh water, suddenly turn into a liquid state [57, ch. 3.2]. This is a great example of the complexity related to macro elastic properties of clay and its ability to contain bounded water as a part of its crystalline structure [57, ch. 3]. The clay-water mix will be modeled in section 3.3.1, see also the calculated macro elastic properties in [1, figure 9].

3.2 Differential effective medium (DEM) model after Kuster and Toksöz (1974)

The effective moduli theory by [16] is based on first order scattering theory [57, ch. 8]. This means that scattering of a P-wave incident on a representative volume V_0, can at position $\underline{x}$ outside volume V_0 be described [57, ch. 8] either as

- the sum of intensities from an incident wave and scattered waves from N inclusion types

or as

- the sum of intensities from the incident wave and scattered waves from V_0 with elastic properties defined by the effective medium.

If we consider a plane wave propagating towards N inclusions randomly embedded within a finite volume V_0 of the effective medium, as illustrated in figure 3.2, we may write the displacement vector $\underline{u}(\underline{x})$ observed at a point $\underline{x}$ outside V_0 [16] as in equation (3.2),

$$\underline{u}(\underline{x}) = \underline{u}_0(\underline{x}) + \sum_{s=1}^{N} \underline{u}_s(\underline{x}, \underline{x}_s) \tag{3.2}$$

where $\underline{u}_s(\underline{x}, \underline{x}_s)$ is the displacement vector observed at $\underline{x}$ due to the wave scattered by the sth inclusion located at position $\underline{x}_s$, and $\underline{u}_0(\underline{x})$ is the displacement from the incident plane wave.

Considering figure 3.2, we have presented a two-phase medium in an infinite matrix (e.g. host medium) bounded by V_0. This could be a model representations of a porous mineral with N randomly shaped and distributed pores. If for example the pores are liquid water filled, and the host medium is some mineral, the porosity of V_0, ϕ, says something about how water filled the effective volume is.

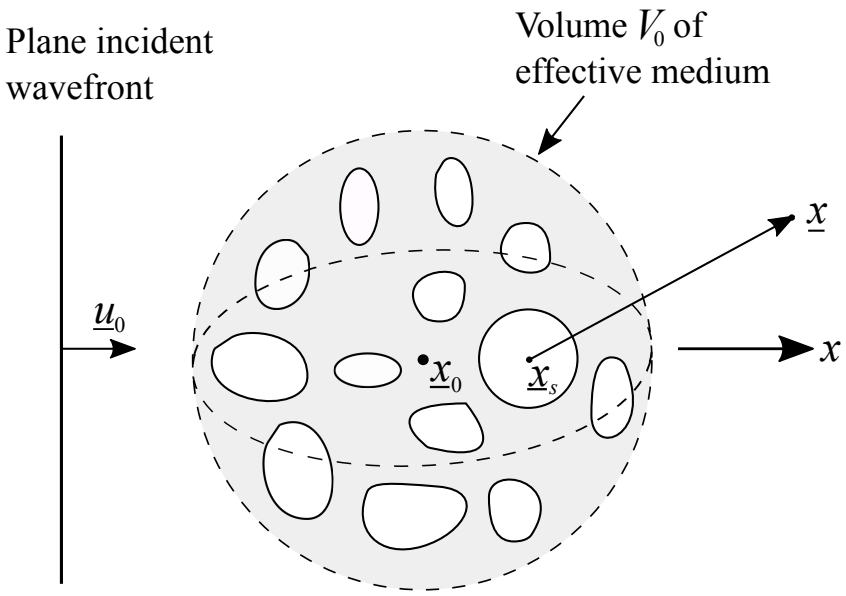

Figure 3.2: Illustration of a plane incident wavefront with displacement vector $\underline{u}_0$, propagating towards some different shaped inclusions (white structures), embedded within a finite volume V_0 of the host medium (gray) in positive x-direction. $\underline{x}_0$ is the center of the representative volume, $\underline{x}_s$ is the center of the sth inclusion and $\underline{x}$ is an observed displacement point outside the matrix. Modified from [16, figure 1].

If we assume this two-phase medium to be homogeneous, we can define the elastic properties of the effective medium to be the same of those of the homogeneous medium, which produces the same displacement field at point $\underline{x}$ as the field generated by the N inclusions [16]. Therefore we can replace the sum of displacement vectors observed at $\underline{x}$ (due to the wave scattered by the sth inclusion located at position $\underline{x}_s$), with a scattered displacement field, $\underline{u}^*(\underline{x},\underline{x}_0)$, as in equation (3.3),

$$\underline{u}(\underline{x}) = \underline{u}_0(\underline{x}) + \underline{u}^*(\underline{x},\underline{x}_0) \tag{3.3}$$

where $\underline{u}^*(\underline{x},\underline{x}_0)$ is the scattered displacement field observed at $\underline{x}$ due to the volume V_0 having effective properties. Thus, from equations (3.2) and (3.3), the fundamental equation defining the effective medium could be written [16] as in equation (3.4),

$$\underline{u}^*(\underline{x},\underline{x}_0) = \sum_{s=1}^{N} \underline{u}_s(\underline{x},\underline{x}_s). \tag{3.4}$$

If we then assume that the two-phase medium is isotropic, the effective medium is also isotropic, hence by requiring that volume V_0 is spherical, the scattered waves do not depend on the orientation of V_0 with respect to the incident field. Now, by assuming that the observation point $\underline{x}$ is sufficiently far away from the representative volume sphere, an approximation [16] given in equation (3.5),

$$\underline{x}_s \approx \underline{x}_0, \qquad s = 1, ..., N \tag{3.5}$$

could be made. This results in that the displacement for the effective medium equals the sum of the displacements from the sth inclusions.

One last assumption, e.g. that multiple scattering effects are negligible, allows us to take the undistributed incident field as the field incident on each inclusion within the representative volume sphere V_0 [57, ch. 8.7]. This restricts the validity of our results to small volume concentrations of inclusions, or to non-interacting inclusions [16]. However, the DEM model version used in this master thesis is extended to incorporate the effect of pore interaction. This could be done using for example the *self consistent approach (SCA)*, which mimics the effect of second and higher order scatterings terms. Such methods have been discussed by [58, 59] and [60], and is implemented in the DEM model used here, given in appendix A.

If assumed only two constituents representing the effective medium, whose volume fractions are V_1 and $V_2 = 1 - V_1$, the elastic moduli of the effective medium, K^*_{DEM} and μ^*_{DEM}, occur from solving two coupled ordinary differential equations [61], given in equations (3.6) and (3.7),

$$(1-y)\frac{d}{dy}\left[K^*_{DEM}(y)\right] = \left(K_2 - K^*_{DEM}\right)P^{*2}(y) \tag{3.6}$$

$$(1-y)\frac{d}{dy}\left[\mu^*_{DEM}(y)\right] = \left(\mu_2 - \mu^*_{DEM}\right)Q^{*2}(y) \tag{3.7}$$

where y denotes volume fraction of inclusion phase embedded in steps dy [1]. K^*_{DEM} and μ^*_{DEM} are the effective bulk- and shear moduli, starting from initial conditions $K^*_{DEM}(0) = K_1$ and $\mu^*_{DEM} = \mu_1$, which are usually set to the elastic moduli of the initial host material. K_2 and μ_2 denote the moduli of the added inclusions and the term P^* and Q^* are geometrical factors associated with the inclusion material, see for example [47, chapter 4.7], for more details.

From the modeled effective bulk- and shear moduli in equations (3.6) and (3.7), the effective compressional- and shear velocities as function of porosity can be calculated using equations (2.41) and (2.42), with effective density estimated as linearly decreasing or increasing, depending on the initial densities of the host- and inclusion constituents [48]. For example, if we want to investigate the elastic properties of a clay mineral incrementally introduced to water inclusions (i.e. water filled pores), we can assume that the effective density will linearly decrease from density of clay ($\rho_{clay} = 2500$ kg/m^3) to density of water ($\rho_w = 1030$ kg/m^3), since the effective density is defined as the total density of the effective medium. For such cases, when the effective medium reaches 100 % porosity, we say that the effective medium is only water, hence the water inclusions have taken up all the representative volume of the effective medium. Therefore, in such cases, the effective density of the effective medium could be seen as linearly decreasing from density of clay to density of water [57, ch. 8.13].

3.2.1 Input file to DEM model

The input file to the DEM model is ".inp"-formatted, which is editable in Text Editor on Linux Ubuntu computers. The input file is constructed in four blocks where the first row defines the bulk modulus (GPa), shear modulus (GPa) and density (kg/m^3) of the host medium. The next row defines the same for the inclusion. The third row specifies the value of the inclusion's aspect ratio (α), named α_w for water and α_{silt} for silt, which says something about the shape of the inclusion (see figure 3.3). The fourth and last row defines the first, last and increment (%) for volume concentration of added inclusions. In table 3.2 is an example of an input file to the DEM model where clay is the host medium and water is the inclusion, with added water inclusions from 0 to 100 % and increments 0.01 %,

Table 3.2: Example of input file to the DEM model when clay is the host medium and water is the inclusion with water aspect ratio $\alpha_w = 0.02$.

Input parameters			Symbols, units & descriptions
21.0	7.0	2.500	K (GPa), μ (GPa), ρ (kg/m^3): host medium (clay)
2.318	0.0	1.030	K (GPa), μ (GPa), ρ (kg/m^3): inclusion (water)
0.02			α_w: aspect ratio of water inclusions (e.g. disk-like)
0.0	100.0	0.01	first, last, increment (%) of water inclusions

The aspect ratio (α) required to the input in the DEM scheme, can be seen as the ratio between the polar axis (a) and the equatorial axes (b) and (c) of an added inclusion, given in equation (3.8),

$$\alpha = \frac{a}{b} \tag{3.8}$$

where for disc-like inclusions, $\alpha \to 0$ when $a \to 0$, and for spherical inclusions, $\alpha = 1$ when $a = b = c$. In figure 3.3 is an illustration of oblate spheroid and disc inclusions. For oblate spheroid inclusions, then $a < b = c$. If the polar axis of an oblate spheroid inclusion becomes small (e.g. $a << b = c$), the oblate spheroid tends to take shape as a disc. And, for instance, if $a > b = c$, the inclusions are called prolate spheroids [16].

3.3 Numerical examples: DEM

The DEM model by Johansen (UiB) (ref. appendix A) is used to calculate the macro elastic properties of mineral-water mixes, based on equations (3.6) and (3.7), which then could relate to macro compressional- and shear velocities according to equations (2.41) and (2.42). In the numerical examples, we will vary the spheroidal water inclusion aspect ratios ($\alpha_w = 0.02, 0.03, 0.04, 0.05, 1.0$) to illustrate the effect of water filled pores with different spheroidal

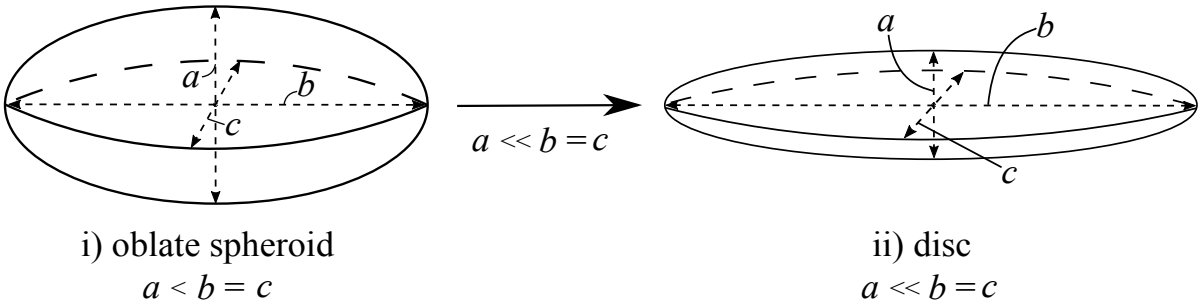

Figure 3.3: Illustration a of aspect ratio α for oblate spheroids used in the DEM models. An i) oblate spheroid inclusion ($a < b = c$), tends to take shape as ii) disc when $a << b$. Modified from [57, ch. 3.10].

pore structures. The main purpose of this modeling is to demonstrate and predict the effective elasticity and seismic velocities in fluid-filled rocks, with known pore geometries. In chapters 3.3.1, 3.3.2, 3.3.3 and 3.3.4, the porosity is strictly related to the percentage of water added to the different silicates.

Then we have, by trial and error, estimated an aspect ratio which at 80 % porosity gave a shear velocity of approximately 10 m/s for the quartz with clay-water mix, to be consistent with [1] and Avseth et.al. [62]; who reported that shallow clay deposits may have a porosity in the range of 60 % to 80 %. We chose this mineral, since we wanted to investigate the macro elastic properties of a more complex mineral, consisting of both coarse (sand) and fine (clay) constituents [56]. Soil is in [56] defined as an "aggregate of minerals and/or organic material which can be disaggregated by hand in water" [56, p.3].

The elastic properties at some initial porosities for the quartz with clay-water mix were then used to construct a new effective medium consisting of the water saturated quartz with clay mineral, embedded spherical silt grains ($\alpha_{silt} = 1$). Since silt is also a quartz material, the quartz with clay-silt mix retains homogeneous, hence the DEM model is still applicable for this case. The purpose of this modeling, was to estimate the effective macro elastic properties for water-filled quartz with clay, embedded spherical silt inclusions. Hence, tuning the DEM model, might indicate a model which could be used to estimate the constituents and porosity of the subsurface.

3.3.1 A: Clay as host medium with added water inclusions

When the input parameters to the DEM model are as in table 3.2 for clay-water mix, the calculated macro elastic properties as function of porosity for oblate spheroid water inclusions with different water-inclusion aspect ratios α_w are given in figure 3.4. We see from figure 3.4, that the variations in aspect ratios are decisive for the effective bulk- and shear moduli, compressional- and shear velocities and the v_p/v_s-ratios. Here are some other observations made from figure 3.4, when porosity increases for the clay-water mix,

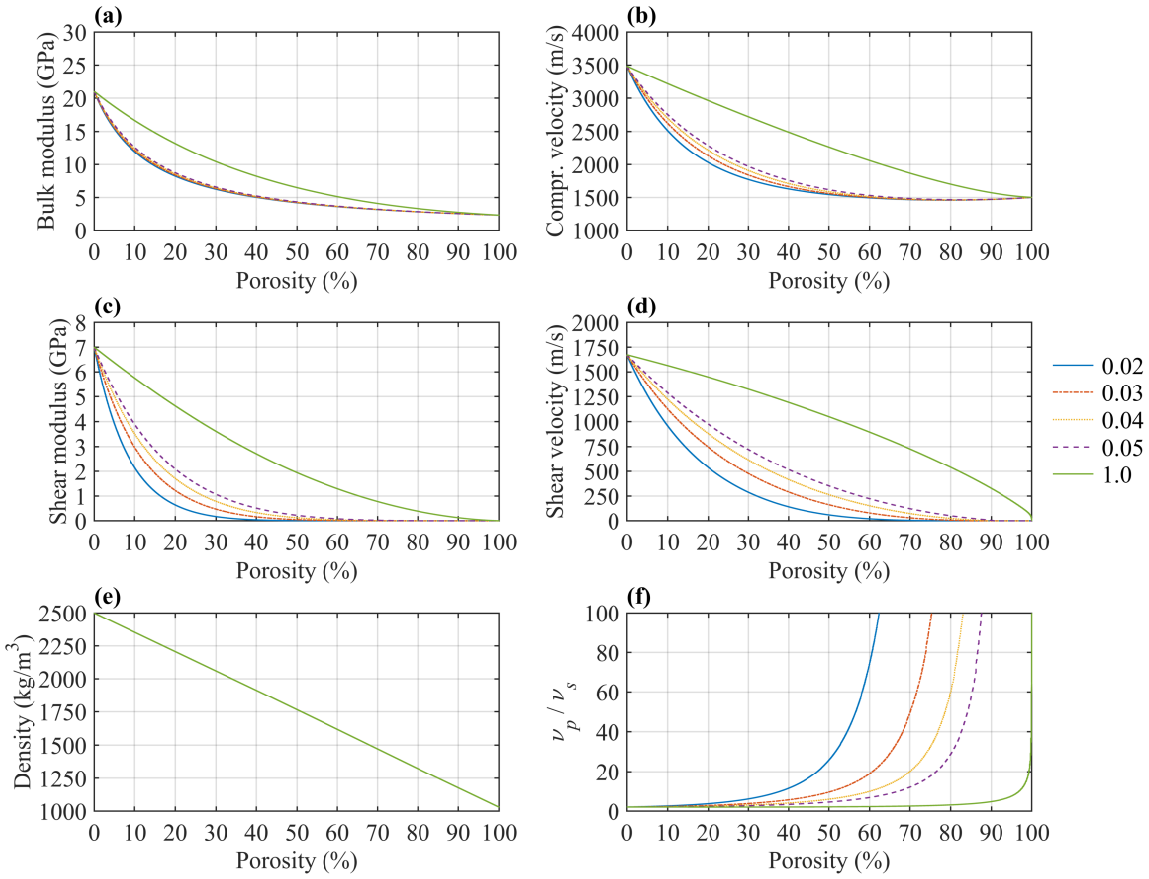

Figure 3.4: Macro elastic properties of modeled clay-water mix when clay is host medium and water is the inclusion with different water-inclusion aspect ratios $\alpha_w = 0.02$ (blue), 0.03 (orange), 0.04 (yellow), 0.05 (purple) and 1.0 (green). a) Bulk modulus K, b) compressional velocity v_p, c) shear modulus μ, d) shear velocity v_s, e) density ρ and f) v_p/v_s-ratio.

- Density (e) decreases linearly from density of clay ($\rho_{clay} = 2500$ kg/m³) towards density of water ($\rho_w = 1030$ kg/m³) for all aspect ratios. Hence, variation in aspect ratio does not effect on the effective density of the clay-water mix.

- Shear modulus (c) goes to zero and the bulk modulus (a) converge towards bulk modulus of water ($K_w = 2.318$ GPa), when porosity increases, hence the effective medium become more water-like.

- Compressional velocity (b) converges towards the P-wave velocity of water ($v_w = 1450$ m/s) and the shear velocity (d) decays towards zero as porosity increases.

- The v_p/v_s-ratio (f) are orders of magnitude higher than more compact sediments [1].

- The v_p/v_s-ratio (f) diverges for large porosities. This has to do with the fact when porosity increases, the effective medium becomes more and more water-like, hence loosing shear strength. For lower aspect ratios and porosities, the v_p/v_s-ratio (f) di-

verge faster, and consequently, due to the loss of shear strength for large porosities, the mineral decreases its overall rigidity faster for lower aspect ratios.

Notice that when evaluating the shear wave velocities in all the modeled effective media, for some reason, the DEM model outputted some (randomly) distributed points very close to 100 % porosity. This we interpreted as an error caused by the calculations in the DEM model code. Since, physically speaking, when porosity reaches 100 %, the shear wave velocity of the effective medium should be zero, since fully porous effective medium should not hold shear strength, hence no shear velocity from equation (2.42). On the other hand, results indicating shear velocities close to 100 % porosity would normally either indicate zero P-wave velocity or infinitely S-wave velocity. From the modeled results figure 3.4, neither cases are present. We therefore concluded that this had to be an issue with the code, hence, to compensate for this error, we checked and manipulating the output shear velocity vector in MATLAB, ref lines 279-322 i appendix B. The manipulation of the shear velocity vector, was done by checking the output shear velocity vector from the DEM model using a for-loop. If a shear wave velocity i was 0, all subsequent shear velocities were converted to zero. This phenomena we first discovered when closely investigating the v_p/v_s-ratio plot for low aspect ratios and high porosities. Consequently, for porosity values for v_s and v_p/v_s close to 100 %, we do not trust the results from the code. This yields for the subsequent macro elastic property results in figures 3.5, 3.6, 3.7 and 3.10 as well.

3.3.2 B: Quartz as host medium with added water inclusions

For the quartz-water mix, we used the inputs in table 3.3 to the DEM model with different oblate spheroid water-inclusion aspect ratios α_w, resulting in the macro elastic properties as function of porosity given in figure 3.5.

Table 3.3: Example of input file to the DEM model when quartz is the host medium and water is the inclusion.

Input parameters			Symbols, units & descriptions
36.6	45.0	2.650	K (GPa), μ (GPa), ρ (kg/m^3): host medium (quartz)
2.318	0.0	1.030	K (GPa), μ (GPa), ρ (kg/m^3): inclusion (water)
0.02			α_w: aspect ratio of inclusions (e.g. disk-like)
0.0	100.0	0.01	first, last, increment (%) of water inclusions

From figure 3.5, we see similar characteristics as for the clay-water mix in figure 3.4. The main difference is that the magnitudes are different, i.e. reflecting that we have changed the host medium from clay (fine soil) to quartz (coarse soil).

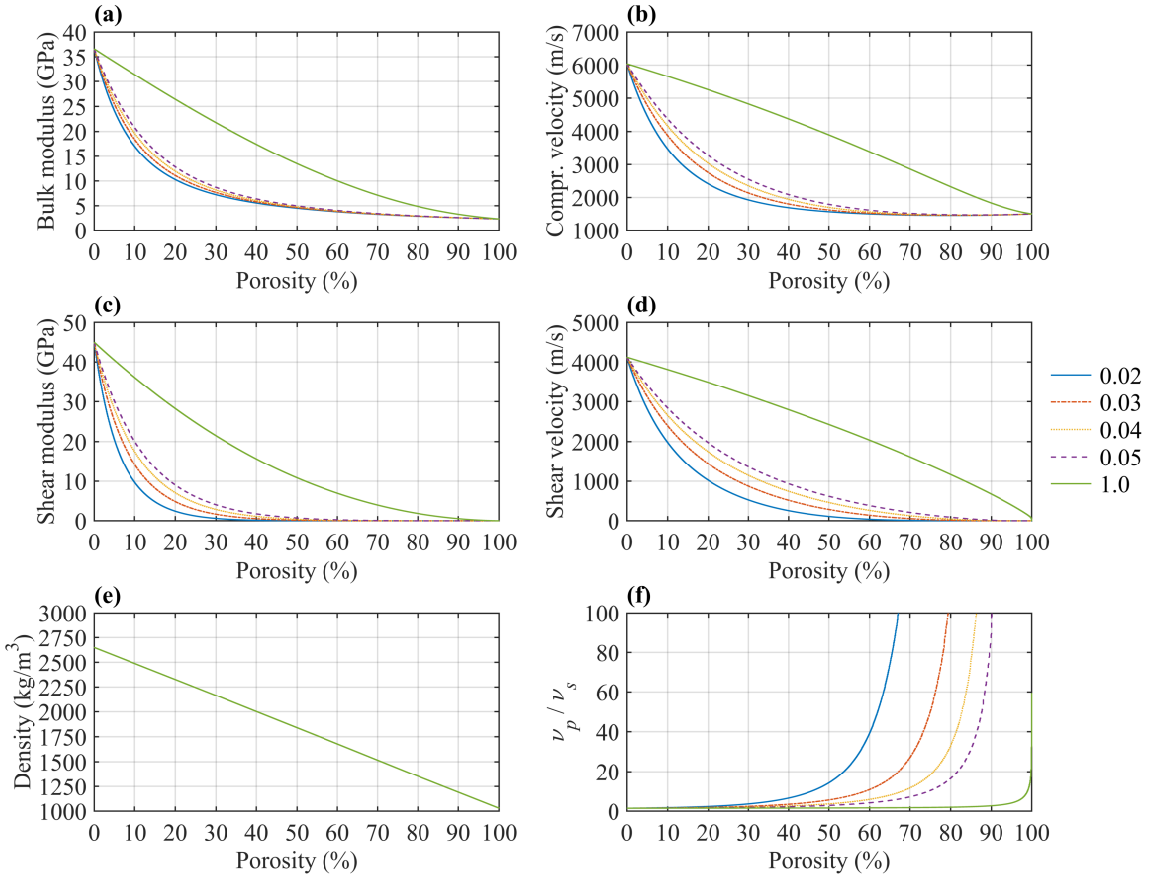

Figure 3.5: Macro elastic properties of modeled quartz-water mix when quartz is host medium and water is the inclusion with different water-inclusion aspect ratios α_w = 0.02 (blue), 0.03 (orange), 0.04 (yellow), 0.05 (purple) and 1.0 (green). a) Bulk modulus K, b) compressional velocity v_p, c) shear modulus μ, d) shear velocity v_s, e) density ρ and f) v_p/v_s-ratio.

3.3.3 C: Silt as host medium with added water inclusions

For the silt-water mix, we use the inputs in table 3.4 to the DEM model with different oblate spheroid water-inclusion aspect ratios α_w, resulting in the macro elastic properties as function of porosity given in figure 3.6.

Table 3.4: Example of input file to the DEM model when quartz is the host medium and water is the inclusion.

Input parameters			Symbols, units & descriptions
37.0	44.0	2.650	K (GPa), μ (GPa), ρ (kg/m^3): host medium (quartz)
2.318	0.0	1.030	K (GPa), μ (GPa), ρ (kg/m^3): inclusion (water)
0.02			α_w: aspect ratio of inclusions (e.g. disk-like)
0.0	100.0	0.01	first, last, increment (%) of water inclusions

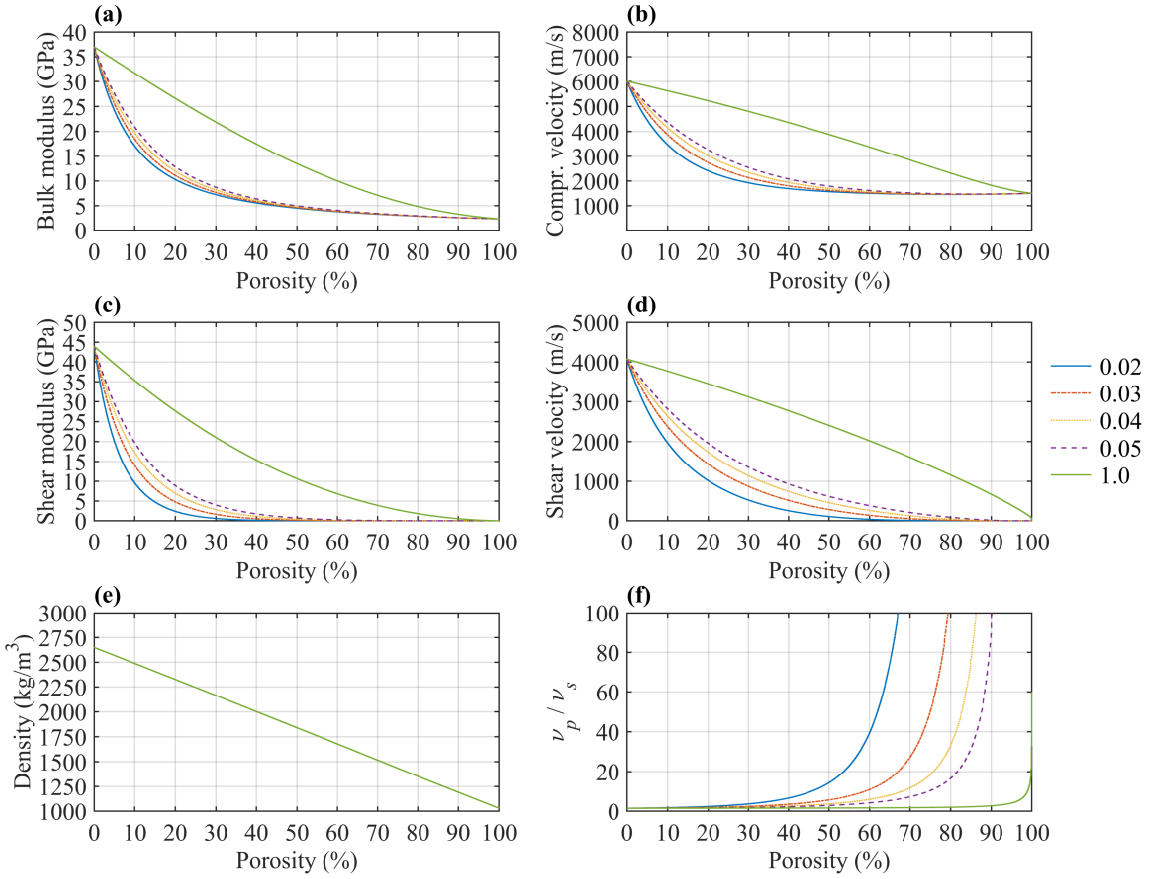

Figure 3.6: Macro elastic properties of modeled silt-water mix when silt is host medium and water is the inclusion with different water-inclusion aspect ratios $\alpha_w = 0.02$ (blue), 0.03 (orange), 0.04 (yellow), 0.05 (purple) and 1.0 (green). a) Bulk modulus K, b) compressional velocity v_p, c) shear modulus μ, d) shear velocity v_s, e) density ρ and f) v_p/v_s-ratio.

We note that the results in figure 3.6 are of similar contour and magnitude as for the quartz-water mix in figure 3.5. Hence the particle diameters separating silt and quartz sand may not influence as much on the macro elastic properties of such mineral-water mixes. Additionally, from the v_p/v_s-ratios in (f), for lower spheroidal aspect ratios, the v_p/v_s diverge for lower porosities. This means that the solid structure looses its shear strength for lower porosities and lower spheroidal water aspect ratios.

3.3.4 D: Quartz with clay as host medium with added water inclusions

For the quartz with clay-water mix, we used the elastic properties reported by Han [55], who measured the v_p and v_s of quartz minerals with small amounts of added clay fractions. The inputs in table 3.5 were inputs to the DEM model with different oblate spheroid water-inclusion aspect ratios α_w, resulting in the macro elastic properties as function of porosity for different water-inclusion aspect ratios given in figure 3.7.

Table 3.5: Input file to DEM model when quartz with clay is the host medium and water is the inclusion.

Input parameters			Symbols, units & descriptions
39.0	33.0	2.650	K (GPa), μ (GPa), ρ (kg/m^3): host medium (quartz with clay)
2.318	0.0	1.030	K (GPa), μ (GPa), ρ (kg/m^3): inclusion (water)
0.02			α_w: aspect ratio of inclusions (e.g. disk-like)
0.0	100.0	0.01	first, last, increment (%) of water inclusions

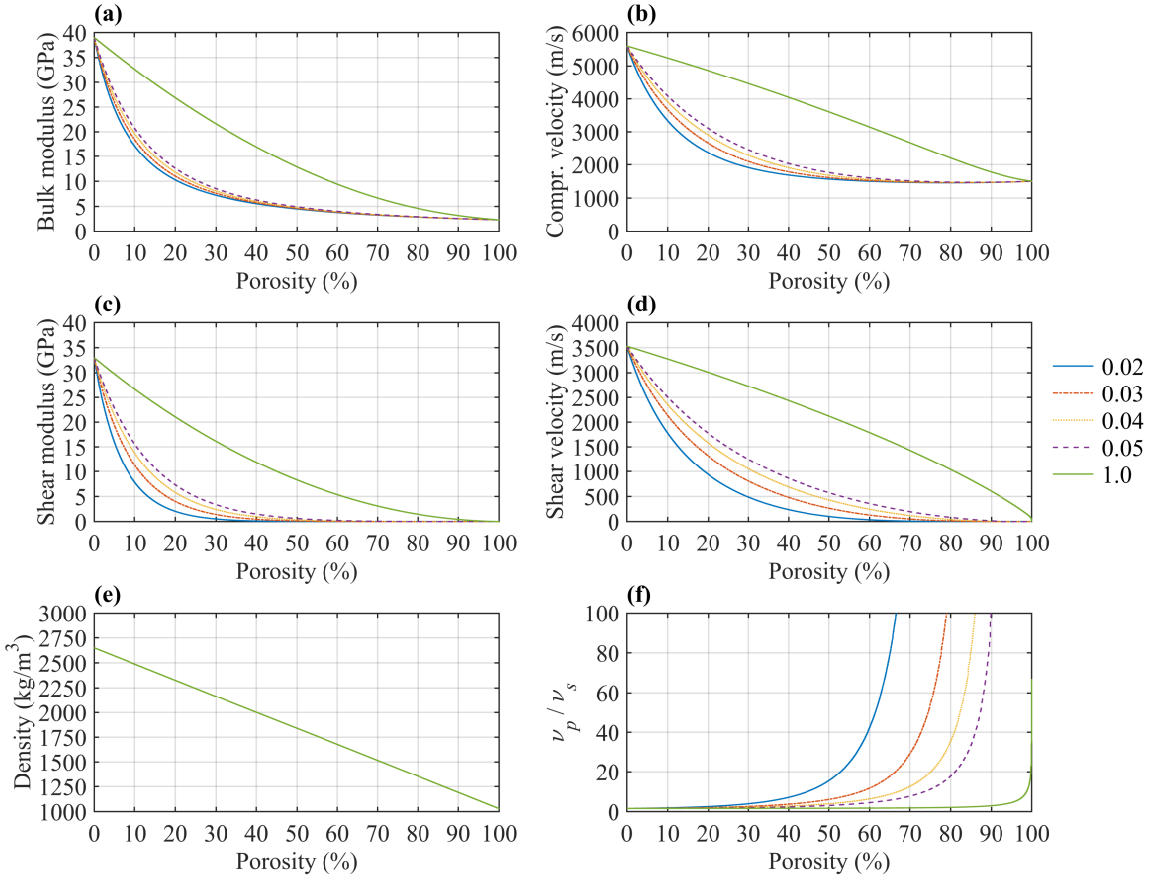

Figure 3.7: Macro elastic properties of modeled quartz with clay-water mix when quartz with clay is host medium and water is the inclusion with different water-inclusion aspect ratios $\alpha_w = 0.02$ (blue), 0.03 (orange), 0.04 (yellow), 0.05 (purple) and 1.0 (green). a) Bulk modulus K, b) compressional velocity v_p, c) shear modulus μ, d) shear velocity v_s, e) density ρ and f) v_p/v_s-ratio.

By changing the spheroidal aspect ratio of water inclusions for the quartz with clay-water mix, we, by trial and error, found the aspect ratio which gave an S-wave velocity of approximately 10 m/s for 80 % porosity, among others to be consistent with Johansen & Ruud [1] and Avseth et.al. [62]. We estimated a spheroidal water-inclusion aspect ratio $\alpha_w = 0.0289$,

which resulted in a modeled macro shear velocity of 10.1 m/s for 80 % porosity, see figure 3.8. The resulting modeled macro elastic properties for the quartz with clay-water mix using

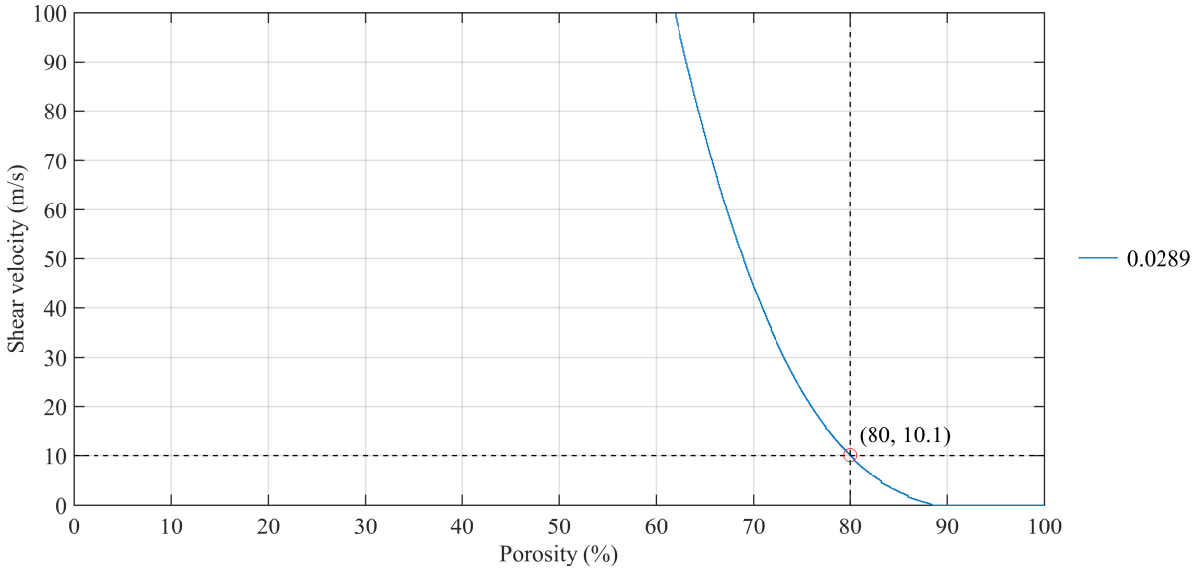

Figure 3.8: Modeled macro shear wave velocities of quartz with clay-water mix (blue) when quartz with clay is host medium and water is the inclusion with constant water-inclusion aspect ratio $\alpha_w = 0.0289$. This aspect ratio resulted in a shear velocity of 10.1 m/s at 80 % porosity, see the red intersection point indicated.

the estimated constant water inclusion aspect ratio ($\alpha_w = 0.0289$) is given in figure 3.9.

From figure 3.9, we see that for 80 % porosity, the effective shear modulus is low, the effective compressional velocity ($v_p = 1412$ m/s) is lower than the compressional velocity of water ($v_{p,w} = 1500$ m/s), and the v_p/v_s-ratio is higher then 100. Next, we averaged ten data-points for some initial porosities for the quartz with clay-water mix with constant water inclusion aspect ratio $\alpha_w = 0.0289$, as given in table 3.6,

Table 3.6: Macro elastic properties for different initial porosities for the quartz with clay-water mix and constant water aspect ratio $\alpha_w = 0.0289$, found in figure 3.7. At each respective initial porosity, ten data-points were averaged for each macro elastic property. Notice that since the effective shear moduli were so low, the magnitudes of the required shear moduli given here are 10^3 times lower than the required magnitudes to the input file to the DEM code.

Initial porosity (%)	Bulk mod. (GPa)	Shear mod. (MPa)	Density (kg/m^3)	v_p (m/s)	v_s (m/s)
60	3.8	23.4	1677.9	1518.4	118.1
65	3.5	9.1	1596.9	1492.3	75.4
70	3.3	3.0	1515.9	1474.7	44.4
75	3.1	0.8	1434.9	1464.1	23.2
80	2.9	0.1	1353.9	1459.7	10.1

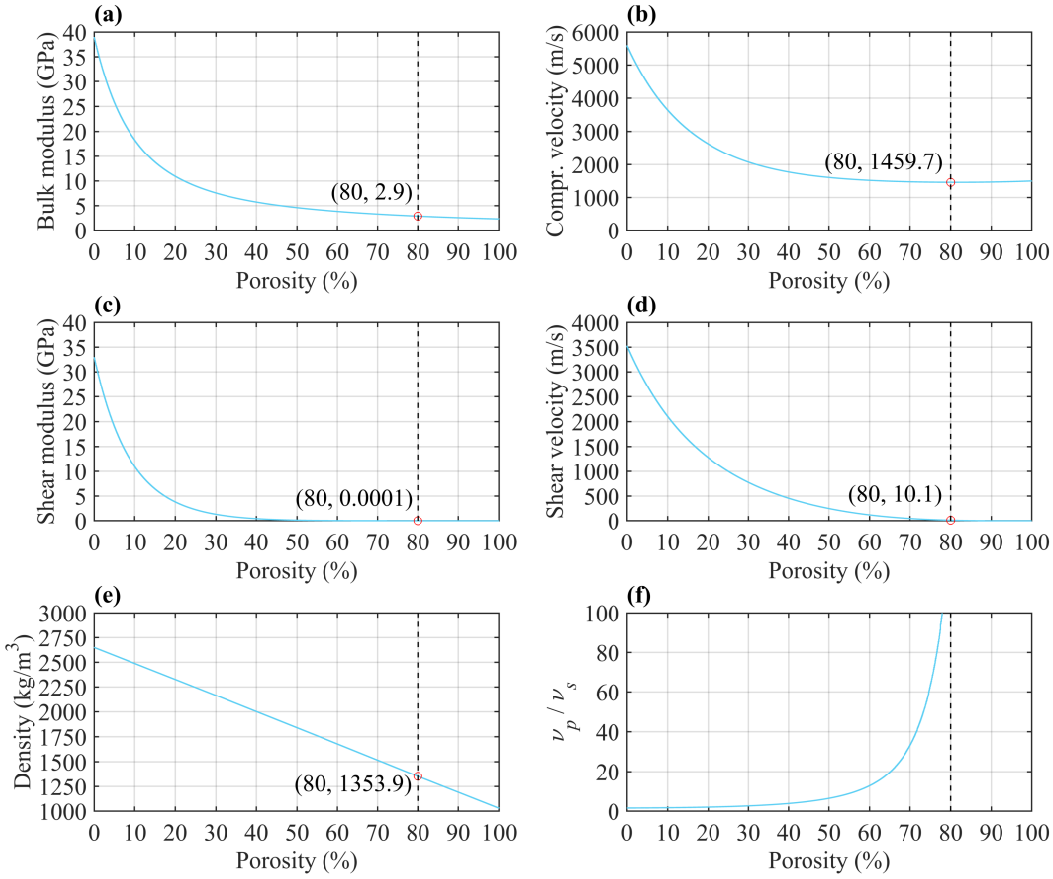

Figure 3.9: Macro elastic properties of modeled quartz with clay-water mix when quartz with clay is host medium and water is inclusion with constant water inclusion aspect ratio α_w = 0.0289 (light blue lines). The red points indicate estimates of the macro elastic properties at the given conditions for 80 % porosity. a) Bulk modulus K, b) compressional velocity v_p, c) shear modulus μ, d) shear velocity v_s, e) density ρ and f) v_p/v_s-ratio.

3.3.5 E: Quartz with clay and water as host medium with added spherical silt inclusions

For different initial water porosities, the water saturated quartz with clay mix in figure 3.7, was introduced to spherical silt grains. This was done to study the effect of adding spherical grains, which have no porosity [1], to a water filled quartz with clay effective medium. In table 3.6, averaged modeled macro elastic properties for different initial porosities, ϕ = 60, 65, 70, 75, 80, are tabulated for the quartz with clay-water mix. We see from table 3.6, that by increasing the initial porosity for the water saturated quartz with clay mineral, leads to lower compressional- and shear velocities for the effective medium. Another observation from table 3.6, is that when increasing the initial porosity, the shear velocities seem to lower most, compared to the compressional velocities. Hence we might conclude that for fine and coarse soils, variations in shear strength are prominent. By studying the variations in shear

velocities for such water saturated minerals, we may be able to say something about the shear module of the effective medium, which could be a great tool to use for when estimating the sub-bottom geological layers at seabeds.

An example of an input file to the DEM model code where water saturated quartz with clay (with constant water aspect ratio $\alpha_w = 0.0289$ and 80 % initial porosity) is host medium, and spherical silt grains are the inclusion, is given in table 3.7. The porosity for the effective medium when spherical silt grains are added in figure 3.11, follow equation

$$\phi = 0.8 \cdot (100 - C) \tag{3.9}$$

where C is the concentration of the spherical silt grains. The resulting macro elastic properties with adding spherical silt grains ($\alpha_{silt} = 1$) to the the water saturated quartz with clay effective medium is given in figure 3.10.

Table 3.7: Example of an input file to the DEM model when quartz with clay and water ($\alpha_w = 0.0289$) is the host medium and spherical silt grains ($\alpha_{silt} = 1.0$) is inclusion, for water saturated quartz with clay mineral at initial porosity 80 %.

Input parameters			Symbols, units & descriptions
2.9	0.0001	1.3539	K (GPa), μ (GPa), ρ (kg/m^3): host medium
37.0	44.0	2.65	K (GPa), μ (GPa), ρ (kg/m^3): inclusions (silt)
1.0			α_{silt}: aspect ratio of silt inclusions (e.g. spherical)
0.0	100.0	0.01	first, last, increment (%) of silt inclusions

From figure 3.10 we see that the v_p/v_s-ratios do not follow the same trends as in the previous macro elastic properties plots. For example for 80 % initial host medium porosities (i.e. 80 % water saturated quartz with clay medium), the v_p/v_s-ratio reaches 100 below 40 % added spherical silt grains. While for the quartz with clay with water as inclusion in figure 3.9, the v_p/v_s-ratio is around 7 at 40 % added water inclusions. This indicates that by adding spherical silt grains, the shear wave velocities of the effective medium reduces significantly for the same porosity of the effective water saturated quartz with clay medium. This observation is in agreement with the results for the clay-water mix studied in Johansen & Ruud [1]. For initial porosity 80 % (see blue curve in figure 3.10b)) the curve seem to jump at around porosity 22-23 %, which might indicate an error in the coding. From discussions with senior engineer Bent Ole Ruud (UiB) and professor Tor Arne Johansen (UiB), we think this has two separate explanations. First, is that since the stop-criterion in the subrutine 'kustext.f' is hard coded (i.e. see line 84 in appendix A.2), the code might fail for porosities reaching critical porosities. Second, the step-length (i.e. d/dy) in the DEM code might be too long, which could result in such error. Hence, we concluded this had to be a coding-issue, which for instance, could be solvable by tuning the stop-criterion and the step-length to fit the model of interest.

The macro shear velocities for different initial porosities of the quartz with clay and water

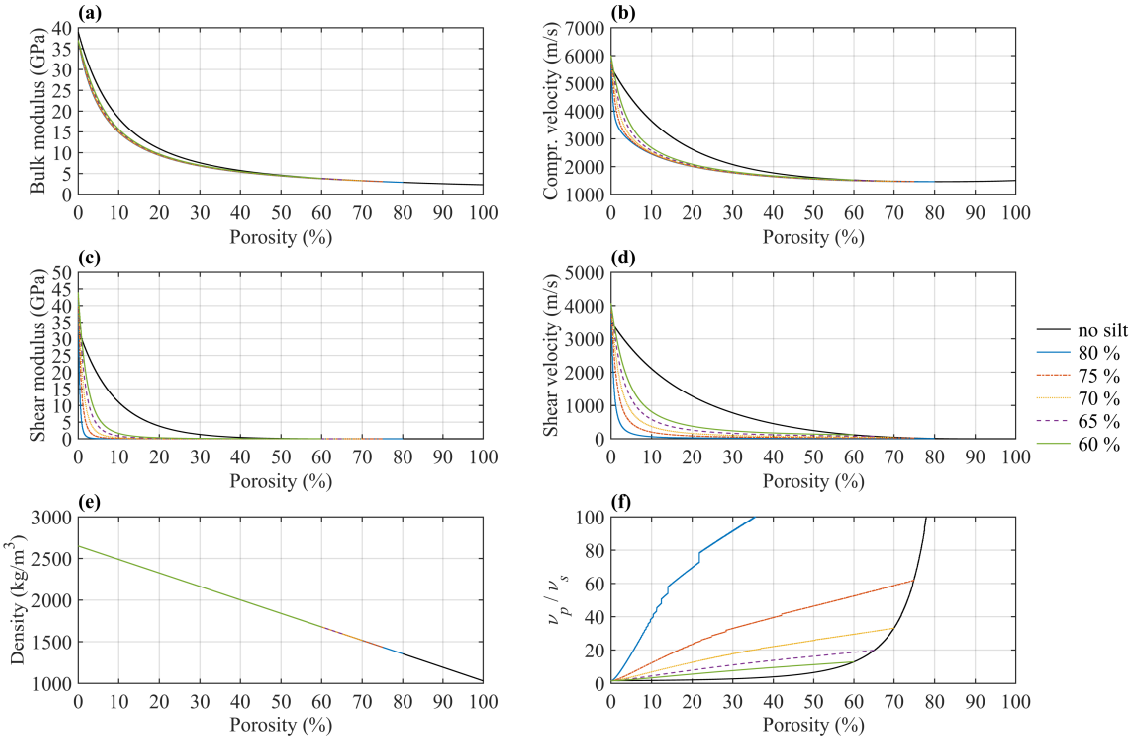

Figure 3.10: Modeled macro elastic properties of modeled quartz with clay-water mix (α_w = 0.0289) as host medium and silt (α_{silt} = 1.0) as inclusion, for different initial porosities of the effective quartz with clay-water host medium. Initial porosities: 80 % (blue), 75 % (orange), 70 % (yellow), 65 % (purple) and 60 % (green). The black curve represents quartz with clay and water, i.e. with no added silt inclusions.

(α_w = 0.0289) as host medium, with spherical silt inclusions (α_{silt} = 1), are given in figure 3.11. We see from figure 3.11 that by introducing the spherical silt fractions to the water saturated quartz with clay mineral, the shear velocities of the effective medium decreases drastically. Additionally the shear velocities highly depend on the initial water filled porosities for the quartz with clay and water effective medium. This is in agreement with the macro elastic results for the clay-water mix studied in Johansen & Ruud [1]. Johansen & Ruud [1] state that when adding the non-porous silt grains to the water saturated clay, in order for the clay to maintain the porosity, "the water-filled porosity of clay needs to increase when porous clay is replaced by silt grains" [1]. This means that the non porous spherical silt grains sort of replaces the water pores, hence resulting in lower porosities and higher shear velocities. For the water saturated quartz with clay effective medium studied in this chapter, we conclude the same. This indicates that the macro elastic properties of water saturated quartz with clay media, are very sensitive to added spherical silt grains. By adding silt grains to water saturated quartz with clay media will increase the shear strength of the effective medium drastically.

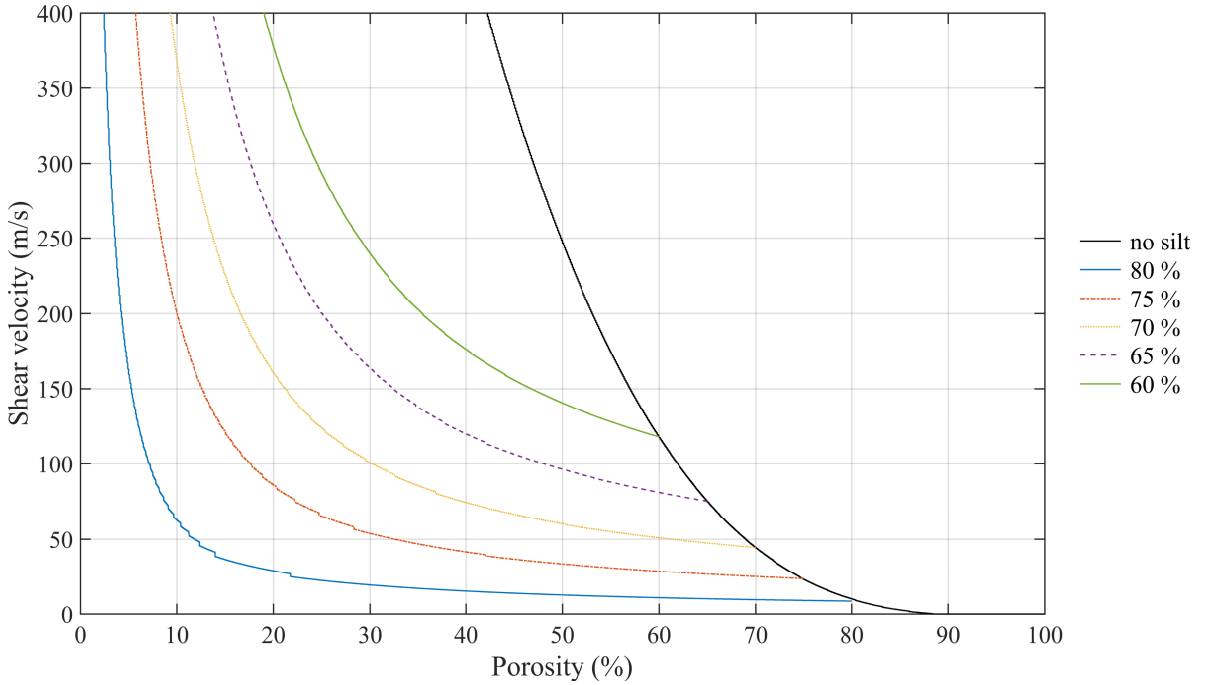

Figure 3.11: Shear velocity varying with porosity when spherical silt ($\alpha_{silt} = 1$) inclusions are added to the quartz with clay and water mix, for different initial porosities; 80 % (blue), 75 % (orange), 70 % (yellow), 65 % (purple) and 60 % (green). The black curve represents quartz with clay and water, i.e. with no added silt inclusions.

Chapter 4

Experimental setup and methods

The seismic arctic experiment conducted in Van Mijenfjorden, Svalbard in late February/beginning of March 2018, was a part of the M.Sc./PhD student course: "AG335/835: Arctic seismic exploration", arranged by the University Centre in Svalbard (UNIS). The seismic experiment was lead by professor Tor Arne Johansen (UiB), with other technical staff supporting the operation.

I, the author of this master thesis, did not attend the Svea 2018 seismic experiment, unfortunately, so we have used the article by Johansen et.al. [4] as source for information for describing the experimental set up. In Johansen et.al. [4] the same seismic method is presented, but with different experimental design, e.g. different receiver intervals and source depths. For the Svea 2018 seismic experiment two 'README' text-files containing information about the experimental setup follow the SEG-Y raw datasets, see appendix C.

4.1 Svea 2018 experimental set up

Detailed information about the experimental set up is important to describe, among others since it helps when modeling and processing the seismic datasets. An illustration of the seismic setup used during the Svea 2018 seismic experiment is given in figure 4.1.

On the right hand side in figure 4.1, we see the two seismic sources used in the Svea 2018 seismic experiment; detonating cords (2 x 25 m Nobelcord detonating cords in parallel (2 kg explosives)) placed on top of the sea ice and airgun submerged in water. Due to some technical problems with the smaller Sercel Mini G airgun (12 cu.in., 2000 psi), the larger Bolt LLX 1900 (40 cu.in., 2000 psi) was used in the experiment for node positions close to land [20]. For other specifications for the sources, see appendix D.

The sources were fired distinctly at 25 m intervals at the node positions. The sources were then moved up-stream and in parallel with the seismic line, i.e. from south-west to north-east in figure 1.2, shooting in the down-stream direction, i.e. from north-east to south-west

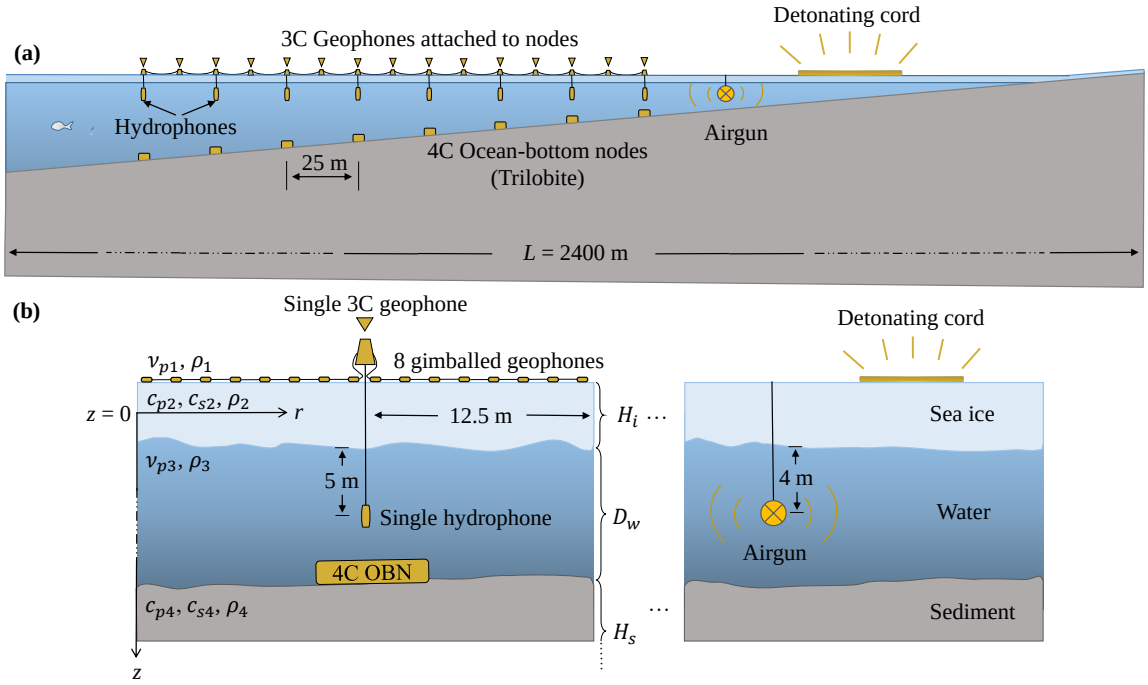

Figure 4.1: Illustration of (a) an overview of (b) the seismic setup used during the Svea 2018 seismic experiment. $L = 2400$ m: total length of the seismic line, H_i: thickness of ice layer ($\sim 20-40$ cm [5]), D_w: water layer thickness ($\sim 0-50$ m [5]), H_s: sediment layer thicknesses (unknown), 3C geophones: three-component geophones (placed on top of sea ice at 12.5 m intervals), 4C OBN: three component geophone + hydrophone ocean-bottom node (trilobite) (placed on seabed at 25 m intervals). With inspiration from [4, figure 2].

in figure 1.2. Some shots with detonating cords were also conducted on land (i.e. at the Credner Moraine, ref figure 1.2), hence figure 4.1a) also include some ice laying on land for illustration.

On the left hand side in figure 4.1b), we see the four different receiver configurations used in the Svea 2018 seismic experiment; eight gimballed geophones (group length 12.5 m), single hydrophones (submerged to constant 5 m depths at 25 m intervals), single three-component (3C) geophones (placed on top of the sea ice at 12.5 m intervals) and single four-component (4C) ocean-bottom nodes (OBNs) (submerged and placed on seabed at 25 m intervals).

In figure 4.2 is a photo of some of the receiver devices used in the Svea 2018 seismic experiment. Before submerging the 4C OBNs at node positions trough drilled holes in the sea ice, they were calibrated (e.g. by space and time calibrating the inbuilt atomic watches with satellites) done by technical staff attending the experiment. At the node positions (at 25 m intervals) one 3C geophone node was place, attached to one single unite hydrophone submerged in water at constant 5 m water depth. Between each node position, eight gimballed geophones (i.e. geophone strings) were placed on top of the sea ice, in parallel to the spread. The geophone strings' midpoints (with group length 12.5 m), were shifted 6.25 m relative to the node positions and attached to the nodes. Up to node position no. 61, 3C geophones were placed at 12.5 m intervals. All receivers had a sampling rate of 1 ms and 8000 sam-

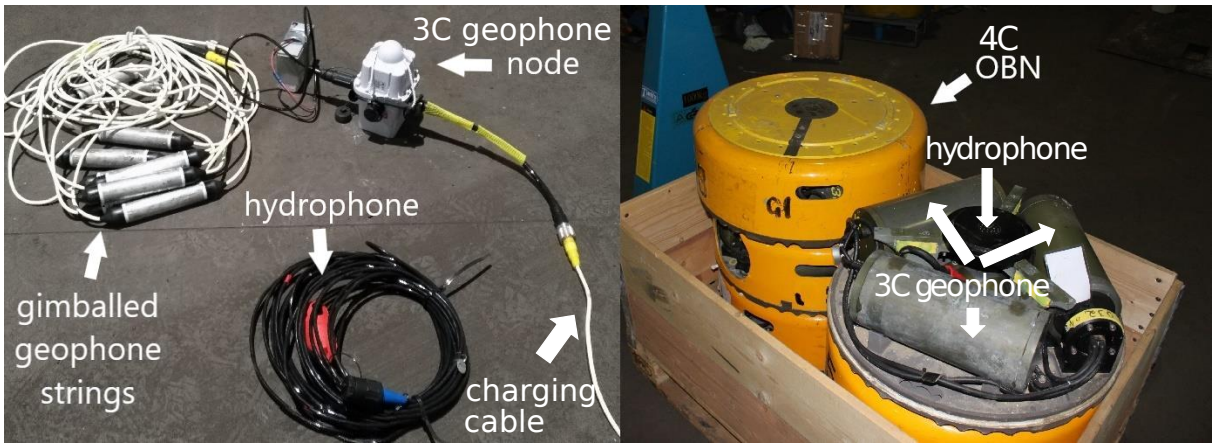

Figure 4.2: Photo of some of the receivers used in the Svea 2018 seismic experiment. Six gimballed geophone string is located at the upper left, single unite hydrophone (black, red and blue) in the lower left, 3C geophone node connected to a battery (connected to a charging cable) in the center left, and some 4C OBNs (right photo), with the 3C geophone and hydrophone components placed inside a yellow capsule. Modified from [19].

ples per trace, yielding a maximum sampling time of 8 seconds per trace. More instrument specifications could be find in appendix D.

There were a total of 100 node positions (i.e. shot points) through the seismic line, with several shots in each node position depending on source type. The Nobelcord detonating cords (25 meters long, two in parallel and 2 m apart, 2 kg explosives), were placed as lines on top of the sea ice in parallel to the seismic line, a few meters away from the seismic line. The cords were detonated in the downstream direction, meaning from north-east according to figure 1.2, burning with a velocity of approximately 7000 m/s [4]. These line sources can therefore be approximated as lines of point sources, in which each point along the cord is triggered with a time delay $\Delta t = x/7000$ m/s, relative to the initial ignition time, with x denoting the distance from the ignition point.

The Sercel Mini G airgun was submerged to different water depths (e.g. 2, 3, 4 m) at the node positions, and several shots were done in the downstream direction (as for the detonating cords). When the larger Bolt LLX 1900 airgun replaced the smaller Sercel Mini G airgun, constant water depth of 4 m was used. Firing the airguns introduced an elastic disturbance (propagating as a bubble pulse [63]) in water, which could hit the water-seabed and water-sea ice interfaces. According to theory of elastic waves, then Scholte waves are excited at these interfaces, measurable close to the respective fluid-solid interfaces.

A summary of the experimental design for the data acquisition is listed in the table 4.1, where the following abbreviations are used:

- DC: Nobelcord detonating cords placed on top of sea ice (25 meters long, two in parallel and 2 m apart, 2 kg explosives).
- AG: Sercel Mini G airgun (12 cu.in., 2000 psi) submerged in water at 2, 3 and 4 m water

depths.

- AG2: Bolt LLX 1900 airgun (40 cu.in., 2000 psi) submerged in water at constant 4 m water depth.
- OBN: four component ocean-bottom nodes (trilobites), consisting of three geophones and one hydrophone, submerged in water to the seabed at different water depths.
- Hydro: single hydrophones in water at constant 5 m water depth.
- Strings: eighth gimballed geophones placed on top of sea ice.
- 3C: single three component geophones placed on top of sea ice.

Table 4.1: Experimental design for data acquisition in the Svea 2018 seismic experiment used in this thesis. *: Due to lack of measured water depths at the first 7 and last 14 node positions', these water depths are unknown.

Source type	Receivers	No. pos.	Receiver int. (m)	Spread (m)	Water depths (m)
Line (2 x 25 m)	OBN	80	25	25-2025	*>51-14
(DC)	Hydro	80	25	25-2025	*>51-14
	Strings	190	12.5	25-2400	*>51-0*
	3C	136	12.5	25-1725	*>51-29
Airgun	OBN	46	25	200-1350	51-25
(AG)	Hydro	46	25	200-1350	51-25
	Strings	92	12.5	200-1350	51-25
	3C	82	12.5	200-1225	51-29
Airgun 2	OBN	20	25	1375-2300	27-<14*
(AG2)	Hydro	20	25	1375-2300	27-<14*
	Strings	40	12.5	1375-2300	27-<14*

As we see from table 4.1, the first last water depths are unknown, due to lack of measured water depths. Although, Senior Engineer Bent Ole Ruud (UiB), who attended the Svea 2018 seismic experiment, estimated that at node position 183 the water depth was 10-12 m (used later when presenting some shot gathers). And if we assume increased water depth for decreasing shot points, the water depths should be larger than 51 m for shot points near 25 m spread. Additionally, from the field-report to Sysselmannen [20], we know that some of the shots were on land on the Credner Moraine, hence the last shots were at 0 m water depth. The same abbreviations used in table 4.1 were also used when naming the SEG-Y datasets, e.g. the SEG-Y dataset named 'svea_2018_ag2_obn.segy' contains measurement results from when measuring the response using the Bolt LLX 1900 airgun as source and the 4C ocean-bottom node as receivers.

The experimental data from the measurement devices, were collected and stored in field using a padded computer which withstands the cold Arctic climate conditions. The data

were later formatted as SEG-Y[(1)]-formatted datasets, one trace for each source-receiver pair.

When choosing which source we wanted to concentrate our research on, we focused mostly on the results from airgun shots. That is because the primary objective of this project was to map the seabed using Scholte waves, i.e. we wanted induced distrubances generated by a source which facilitate to generate low-frequency seismic energy, compared to the relative high seismic energy generated by detonating cords [4, 5]. Additionally, when using detonating cords on sea ice in shallow waters, the induced flexural waves might hide the Scholte waves [5], which is to be avoided for this project.

From the land shots, i.e. for high shot numbers in the datasets, we plotted some of the DC shots to see if we could observe and measure a Leaky Rayleigh-to-Scholte wave conversion. The hydrophone datasets were also briefly analyzed, but Scholte waves were not observed in these datasets. The geophone strings data sets were not analyzed in details, since it was the main subject in [1]. We therefore concentrated, and will only present, the airgun shots with the four component OBNs and the three component geophones as receivers.

4.2 Seismic signal processing techniques used

When we process the synthetic shot gathers in chapter 5 and measured shot gathers in chapter 6, we use some conventional digital processing techniques to remove noise with minimal possible impact to the signal itself. We used the open source CWP/SU package [23] for processing and plotting the results. We will briefly present the processing techniques used, and explain the physical applications of these techniques, found in for examples Yilmaz [45].

4.2.1 Amplitude recovery - SUGAIN: *t*-squared

Amplitude recovery processing techniques, using SUGAIN in CWP/SU [23, pp. 59-60], attempt to correct for the amplitude losses that are unrelated to the reflection coefficient, such as wave attenuation, spherical spreading and source variations. To compensate for wave attenuation and spherical spreading, both statistical and deterministic approaches exist [66] - we applied the deterministic *t-squared* method.

The reason this method is called the t-squared method, is discussed in for example Clarbout [67, pp.233-234]. According to [67, pp.233], the first power of t is a result from transforming the three dimensional space to one when assuming plane waves. But since spherical wave amplitudes, which are proportional to the square root of the energy, spread out in three di-

[(1)]The SEG-Y format is a standard developed by the Society of Exploration Geophysicists (SEG) for storing geophysical data, first published in 1975 [64]. This standard was originally developed for storing single-line seismic reflection digital data on magnetic tapes. Ever since, the standard has been developed due to the nature of seismic data acquisition, processing and continuous evolving of seismic hardware. The latest version, named the *rev 2.0 specification* [65], also allows for storing 2D and 3D seismic data.

mensions, the surface area of the wave expands with radius squared. Consequently, the area at which the energy is distributed is also proportional to the time squared. But, since acoustic amplitudes are proportional to the square root of the energy, only a single power of t is necessary for spherical divergence correction [67, pp.233].

The second power of t comes from a simple absorption model, which from experience is shown to be needed [67]. Assume a plane wave propagating in one dimension in a medium with constant medium velocity and a frequency dependent absorption factor, $\alpha_{Np/m}$. If, in addition, we assume no multiple reflections and white noise, the absorption model could be given as an integration over all positive frequencies given in [66], as in equation (4.1),

$$\int_0^\infty e^{-\pi f t/Q} df = \frac{Q}{\pi t} \tag{4.1}$$

where the multiplication of t in equation (4.1) comes from an assumption that the amplitudes for monochromatic waves decrease exponentially with depth. Q in equation (4.1) is the so-called *seismic quality factor*, which is material and wave specific (often diagnostic of rock type), and is a measure of how *dissipative* the material is [47, pp.121-129]. The fraction between the point source's wave amplitude, A, at distance, r, away from the point source, and reference wave amplitude, A_0, at reference distance, r_0, away from the point source, could be given as in [66], as in equation (4.2),

$$\frac{A}{A_0} = \frac{r_0}{r} e^{-\alpha(r-r_0)}, \qquad \texttt{where} \quad \alpha_{Np/m} = \frac{\pi f}{Q v} = \frac{\pi}{Q\lambda} \tag{4.2}$$

where v_{ph} is phase velocity (m/s), f is frequency (Hz) and $\lambda = v/f$ is the wavelength (m) of the wave. In general, we see from equation (4.2) that the smaller Q–factor, the larger absorption (i.e. $\alpha \propto Q^{-1}$). The Q-factor for compressional- and shear waves will be defined in chapter 5.2.1.

4.2.2 Digital band-pass filtering - SUFILTER

After a Fourier transform of a shot gather, we can use the standard zero-phase, sine-squared tapered digital Ormsby band-pass filter, called SUFILTER in CWP/SU [23], to remove noise effects in the seismic data for a given frequency interval. The Ormsby bandpass filter requires four frequencies: low cut-, low pass-, high pass- and high cut frequencies [45, pp. 41–46]. We used the filter coefficients: [low cut, low pass, high pass, high cut] = [1, 2, 20, 40] Hz on all shot gathers, to filter away frequency components close to zero hertz as well as the highest frequency components. The low pass and high pass filter coefficients are the so-called *-3 dB frequencies* [24], i.e. at which half of the power of a signal is enclosed, which for our example are 2 Hz and 20 Hz.

4.2.3 Trace balancing - SUGAIN: pbal, mbal

We used trace balancing to correct for different source variations [68, p. 180], by scaling the amplitudes according to a time-invariant balancing factor, i.e. a frequency dependent balancing factor [45, pp. 89]. For SUGAIN: pbal [23, p. 72], the amplitudes for all traces in a given shot gather are divided by the RMS power of the amplitudes, i.e. the square root of the sum of the squared amplitudes for all traces in the shot gather [68]. For SUGAIN: mbal [23, p. 72], the factor is determined by the mean amplitude of each trace, and the amplitudes are subtracted for each trace individually.

4.2.4 Trace stacking - SUSTACK

We stacked our traces if there were multiple shots in the same position. Stacking of multiple shots in the same source position, often increases the signal-to-noise ratio (SNR), e.g. if noise is Gaussian or "white", the improvement of SNR is proportional to the square root of total number of traces [69].

4.3 Plotting of seismic data

The results from the seismic datasets were both processed and plotted using the CWP/SU package. The CWP/SU's primary interface is the UNIX commandline and shell script language. To run multiple commands using the CWP/SU package, the commands can be cascaded via UNIX pipes in shell (SH) scripts [23, p. 14], meaning lines ending with UNIX pipes (i.e. with symbols "|"), are inputs to subsequent lines, etc..

In this thesis, the SH scripts read, processed and plotted the results as postscript (PS) files. In appendix I is an example of a shell script which plots the seismograms, $(f-k_r)$ and $f-v$ spectra for model A in chapter 5.3. For model B and C, and the measured datasets, similar scripts were written. Each dataset was gain corrected using SUGAIN, frequency-filtered using SUFILTER and windowed using SUWIND with the CWP/SU package. The seismograms were plotted using SUPSWIGP (PostScript Polygon-filled WIGgle plot of a SEG-Y dataset) and the respective frequency domains were plotted using SUPSIMAGE (PostScript IMAGE plot of a SEG-Y dataset).

The $(f-k_r)$ domains were calculated using SUSPECFK (F-K Fourier SPECtrum of data set), which transforms the data from the offset-time $(r-t)$ to the frequency-wavenumber $((f-k_r))$ domain. Note that when using SUSPECFK, the horizontal wavenumber is coded with unit (1/m). This comes from the relation given in [70], which for a given phase defined as $i(\omega t - k_r r)$, is transformed as in equation (4.3),

$$i(\omega t - k_r r) = 2\pi i(Ft - K_r r) \tag{4.3}$$

where F and K_r define the notion of frequency and wavenumber. Hence the relation between the wavenumbers are as in equation (4.4),

$$k_r = 2\pi K_r \tag{4.4}$$

The frequency-phase velocity domains were calculated using SUPHASEVEL (Multi-mode PHASE VELocity dispersion map computed from shot record(s)) [44] based on the transformation method described by Park et.al. [43].

The results were then converted to PDF formatted files before attached to this document. By first saving the files as PS and then converting to PDF, vector graphics are enabled, which ensures high quality images and high resolution. Additionally, the media box bounds follow the same as the original PS bounding box, which rejects redundant white space in the results.

Chapter 5

Modeling surface acoustic Scholte waves (OASES)

In this chapter, results from modeling the amplitudes (i.e. pressure and vertical particle velocity) of surface acoustic Scholte waves in two-dimensional horizontally stratified environments will be presented. The model we used is based on the wavenumber integration technique in combination with the *Direct Global Matrix* [14] solution, called *Ocean Acoustic and Seismic Exploration Synthesis* (OASES) [18, 13], where attenuation is accounted for by allowing for the medium velocities to be complex. OASES is based on its predecessor called *Seismo-Acoustic Fast Field Algorithm for Range Independent Environments* (SAFARI), with a user guide given in [71]. We have used the module called *OASES-OASP: 2D Wideband Transfer Functions*, which calculates the "depth-dependent Green's function for a selected number of frequencies and determines the transfer function at any receiver position by evaluating the wavenumber intergral" [15, ch. 8].

One characteristic property of the Scholte wave is that it is normally dispersive, i.e. in the $(f - v_{ph})$ domain, the phase velocity of the Scholte wave changes with frequency, or alternatively, a slight change in frequency, might cause a relatively big change in phase velocity. This dispersive characteristic is detected when the sedimentary properties, and correspondingly seismic velocities, vary with depth, where several Scholte wave modes occur [72, 73].

5.1 Input file to OASES-OASP

When modeling in OASES-OASP: 2D Wideband Transfer Functions, we limit our environmental models so that all geological layers are horizontally stratified, the interfaces are plane and in parallel, and the mechanical layer properties are functions of depth only, i.e. the geological layers consist of homogeneous, isotropic solids/sediments. The fluid layer, e.g. water, is modeled as a homogeneous, ideal fluid layer, in contact with the sediment/solid at all time. The depth of the respective fluid layer is based on an average seawater depth from the Svea

2018 seismic experiment, to be consistent with the water depths in the experimental results.

Hope & Schmidt [74] have made a parallelized version of some modules in the OASES package. As for the OASES Post-Processor range-independent module, each frequency response can be calculated independently, hence lowering the computational burden. Since our models are not that complicated and the frequency bandwidth is relatively low, i.e. 0 to 40 Hz with 61 mHz intervals, we did not use the parallelized version of the OASES package. On the other hand, when running the OASES-OASP, by using Secure Shell (SSH) protocols, a supercomputer called "Ultrasonic" was used, which by October, 22 2020, had eight cores and a total of 252 GB RAM. This supercomputer belongs to the Acoustic group at UiB. By using Ultrasonic, the computational time was approximately halved, compared to using a regular Linux Ubuntu student PC available at the student office.

The environmental model input file to OASES-OASP is structured in eight blocks [15, pp. 59-74]. The blocks need to be filled in with information by the user. In appendix E is an example of an input file to OASES-OASP is attached. In Block IV the environmental model is defined, where the user defines the horizontally stratified layers. According to the manual [15], the environmental model inputs are:

- z_m: depth of layer m
- $v_{p,m}(v_{c,m})$: Pressure (compressional in solids) phase velocity (m/s) in layer m
- $v_{s,m}$: shear phase velocity (m/s) in layer m
- $\alpha_{p,m}$: pressure (compressional in solids) attenuation (dB/λ) in layer m
- $\alpha_{s,m}$: shear attenuation (dB/λ) in layer m
- ρ_m: density (g/cm^3) in layer m
- $N_v(\Delta \underline{r})_m$: RMS value of interface roughness (m) in layer m

The input file is then directed to OASES-OASP by a C-shell (.csh) code, readable for UNIX operating systems. In the C-shell code we read the input file and direct the input file to where OASES-OASP is installed on the computer.

Then we run the OASES-OASP module. A description of how the OASES-OASP module solves the depth equation is given in Jensen et.al. [18, ch. 4.3], as in three steps. First, the OASES-OASP code calculates the depth-dependent Green's function (i.e. equation (2.25)) at a discrete number of radial wavenumbers for the selected receiver depth(s). Secondly, the wavenumber integral (e.g. for vertical particle displacement given in equation (2.17)) is evaluated, which yield the transfer function at the selected depths and ranges. By repeating these two steps at selected frequencies, the frequency integration (i.e. inverse Fourier transform in equation (2.12)) is done to yield the total response in time [18, p. 244]. The range-stacked

shot gathers are then saved as ASCII files and converted to CWP/SU files using a script called *asc2su* (made by Senior Engineer Bent Ole Ruud, see appendix G). Another shell code is then made for processing and plotting the range-stacked shot gathers using CWP/SU.

When processing and plotting the results SU formatted results from OASES, we constructed several shell scripts, see for example appendix I. The processing techniques are briefly described in chapter 4.2. We used different processing techniques depending on the receiver lay out. The $(f-k_r)$ and $(f-v_{ph})$ spectra of the results were calculated using CWP/SU's SUSPECFK and SUPHASEVEL modules, respectively. These results were then imaged as postscript images using SUPSIMAGE in CWP/SU. The $(f-k_r)$ and $(f-v_{ph})$ spectra were colored, from dark blue (low) to red (high), based on a smooth color distribution. These results will be presented and commented in chapters 5.2 and 6.

5.2 Numerical examples: OASES-OASP

When modeling in this chapter, we use the inverted environmental model given in Johansen & Ruud [1, table 2], added a relatively thin two layered sea ice layer on top with thicknesses reported in Johansen et.al. [5, table 2], and with respective compressional and shear sea-ice velocities reported in Johansen et.al. [4, table 3]. Although these three papers are based on different seismic experiments, conducted at different times, all are based on results from seismic experiments in Van Mijenfjorden, Svalbard. The main purpose of the modeling in this chapter, is to observe Scholte waves, and to analyze the seismic response with an added, relatively thin, two-layered sea ice layer on top of the water layer. Additionally, we wanted to verify if this environmental model could be representative for the measurement results given in chapter 6.

The environmental model given in Johansen & Ruud [1, table 2], is based on inverted shear velocity estimations by measured group- and phase velocities. It is constructed based on having the compressional velocities fixed and increasing with depth, and computing the densities from the compressional velocities by the Nafe-Drake relation given in [75]. Then, by a hypothesis that the shear velocities also increase with depth, the shear velocities were calculated using the inversion program called *surf96*, see Herrmann [76]. The thickness of the sea ice layer for the Svea 2016 seismic experiment, was reported in Johansen et.al. [5] to vary between 20 to 40 cm, we chose a 40 cm thick sea ice layer, divided into two separate sea ice layers of 10 cm and 30 cm layer thicknesses. The compressional and shear velocities of 3000 m/s and 1500 m/s, and 1600 m/s and 800 m/s, where assigned to the two sea ice layers, respectively, in table 5.1.

First, note that for the environmental model in table 5.1 to be representative for the experimental results, the water layer thicknesses for the models were set to correspond with the measured water depths from the experimental results in chapter 6. Consequently, two dif-

Table 5.1: Environmental model used when modeling in OASES-OASP. The properties for the two-layered sea ice layer is taken from [4, table 3], modified to fit the measured sea ice thicknesses reported in [5]. The properties of water and sediment layers' are taken from [1, table 2], with estimated average water layer thickness of 19.1 m. The first layer (i.e. air) is the upper-halfspace and the last layer (rock bottom) is the lower half-space, meaning they extent to $+/-\infty$, respectively.

Layer Number	Depth (m)	v_p (m/s)	v_s (m/s)	α_p (dB/λ)	α_s (dB/λ)	Density $(\mathrm{kg/m^3})$	Typical Layer
1	–	325.0	–	0.0	0.0	1.3	Air (half-space)
2	0.0	3000.0	1500.0	0.1	0.1	920.0	sea ice top
3	0.1	1600.0	800.0	0.1	0.1	920.0	sea ice bottom
4	0.3	1500.0	0.0	0.1	0.1	1030.0	water
5	19.5	1600.0	44.0	0.1	0.1	1217.0	sediment 1
6	25.5	1650.0	95.0	0.1	0.1	1478.0	sediment 2
7	25.5	1700.0	168.0	0.1	0.1	1645.0	sediment 3
8	37.5	4200.0	2200.0	0.1	0.1	2500.0	rock bottom (half-space)

ferent water thicknesses of 19.1 m (for results in chapters 5.3 and 5.4) and 32.0 m (for results in chapter 5.5) are used.

Second, note that the unit for densities to the OASES-OASP input files, see appendix E, do not follow the SI-standard. In OASES-OASP it uses the $\mathrm{g/cm^3}$ unit [15], hence one must divide by 10^3 in this table to get the corresponding density magnitudes used as inputs to OASES-OASP.

5.2.1 Accounting for viscoelastic attenuation in OASES-OASP

In table 5.1 the compressional- and shear attenuation constants, α_p and α_s, were set the same for all layers, i.e. 0.1 dB/λ, except for the air layer which was set to zero. As mentioned, viscoelastic attenuation is included in the wavenumber integration approach by allowing for complex medium velocities, i.e. complex medium wavenumbers, in layers m. For pressure waves in fluid layers, i.e. compressional waves in elastic media, we therefore assume complex medium wavenumber, $\widetilde{k}_m$, given in Jensen et.al. [18, p. 243] as in equation (5.1),

$$\widetilde{k}_m = k_m(1+\delta_{p,m}), \qquad \delta_{p,m} > 0 \tag{5.1}$$

where k_m is the medium wavenumber in layer m, and $\delta_{p,m}$ is the so-called *loss tangent* for pressure waves in fluids and compressional waves in elastic media in layer m. Similarly, for shear waves in elastic media in layer m, we define the complex wavenumber, $\widetilde{\kappa}_m$, given in Jensen et.al. [18, p. 243] as in equation (5.2),

$$\widetilde{\kappa}_m = \kappa_m(1+\delta_{s,m}), \qquad \delta_{s,m} > 0 \tag{5.2}$$

Next, Jensen et.al. [18, p. 243] state that from experimental results given in Ewing & Jardetsky [41] and Kolsky [77], most elastic media have attenuations increasing linearly with frequency. Hence, by introducing complex Lamé constants, $\widetilde{\lambda}_{s,m}$ and $\widetilde{\mu}_{s,m}$, for elastic solid media in layer m (subscript s stands for solid as in chapter 2.5), given in [18, p. 243] as in equations (5.3) and (5.4) for layers m,

$$\widetilde{\lambda}_{s,m} = \lambda_{s,m} - i\lambda'_{s,m} \tag{5.3}$$

$$\widetilde{\mu}_{s,m} = \mu_{s,m} - i\mu'_{s,m} \tag{5.4}$$

we can find that the linear frequency dependence of attenuation requires that the ratios given in [18, p. 243], as in equations (5.5) and (5.6) for layer m,

$$\frac{\lambda'_{s,m} + 2\mu'_{s,m}}{\lambda_{s,m} + 2\mu_{s,m}} = \frac{1}{Q_{p,m}} \tag{5.5}$$

$$\frac{\mu'_{s,m}}{\mu_{s,m}} = \frac{1}{Q_{s,m}} \tag{5.6}$$

must be constant. Where $Q_{p,m}$ and $Q_{s,m}$ are the so-called *quality factors* for compressional and shear waves in solids in layer m, respectively. Hence, Jensen et.al. [18, p. 244] argues that for small attenuations (i.e. large $Q_{p,m}$ and $Q_{s,m}$), we find the relation between the loss tangents, $\delta_{p,m}$ and $\delta_{s,m}$, and the quality factors, $Q_{p,m}$ and $Q_{s,m}$, by the definitions of the compressional speed and shear speed in layer m (see equations (2.41) and (2.42)). This results in the relation given in Jensen et.al. [18, p. 244], as in equations (5.7) and (5.7) for layer m,

$$\delta_{p,m} = \frac{1}{Q_{p,m}} \tag{5.7}$$

$$\delta_{s,m} = \frac{1}{Q_{s,m}} \tag{5.8}$$

Then, according to Jensen et.al. [18, p. 244], the loss fraction in layer m, for compressional waves in equation (5.7) and shear waves in equation (5.8), can relate attenuations in dB per wavelength, $\alpha_{p,m}(\mathrm{dB}/\lambda)$ and $\alpha_{s,m}(\mathrm{dB}/\lambda)$, in layer m. This relation is given in Jensen et.al. [18], as in equations (5.9) and (5.10) for layer m,

$$\alpha_{p,m}(\mathrm{dB}/\lambda) = 40\pi\,\delta_{p,m}\,\log e \approx \frac{27.29}{Q_{p,m}} \tag{5.9}$$

$$\alpha_{s,m}(\mathrm{dB}/\lambda) = 40\pi\,\delta_{s,m}\,\log e \approx \frac{27.29}{Q_{s,m}} \tag{5.10}$$

Jensen et.al. [18] comments further that the attenuations $\alpha_{p,m}(\mathrm{dB}/\lambda)$ and $\alpha_{s,m}(\mathrm{dB}/\lambda)$ have to be meaningful, requiring that a "pure dilatation of an elastic medium does not produce

energy." [18, p. 244]. According to Jensen et.al. [18], this results in that the bulk modulus must have a positive imaginary part. Hence, the fraction between the attenuations required that the relation given [18, p. 244], as in equation (5.11) for layer m,

$$\frac{\alpha_{s,m}}{\alpha_{p,m}} = \frac{\delta_{s,m}}{\delta_{p,m}} < \frac{3}{4}\left(\frac{c_{p,m}}{c_{s,m}}\right)^2 \tag{5.11}$$

is required.

5.2.2 Receiver arrays used in OASES-OASP

We used three different receiver array configurations, see table 5.2. As wee see from table

Table 5.2: Table of receiver array specifications used in OASES-OASP when modeling the seismo-acoustic response with three different receiver arrays. All receiver arrays use the same synthetic point-source located at constant water depth $z_s = 4$ m, with center frequency $f_c = 10$ Hz. OASES-OASP options: P: negative complex pressure amplitudes ($|-p(k_r,z)|$) calculated, V: vertical particle velocity amplitudes ($|v_z(k_r,z)|$) calculated. Receiver array analogies to measurement devices: OBN: ocean bottom-nodes, 3C: three component geophones.

	Receiver depth (m)	Receiver interval (m)	Options (P or V)	Representative Receiver
Model A	19.4	5	P	OBN hydrophones
Model B	19.4	5	V	OBN 3C
Model C	0.05	5	V	3C

5.2, all models have the same spatial receiver interval $\Delta r = 5$ m, which from the Nyquist wavenumber criterion (using a phase such as $i(\omega t - k_r r) = 2\pi i(Ft - K_r r)$ [70]), yields,

$$K_{ny} = \frac{1}{2 \cdot 5} = 0.1 \text{ m}^{-1} \tag{5.12}$$

The water depths for the synthetic receiver arrays in table 5.2 differ, as well as which amplitudes are calculated. In model A we calculate the negative pressure in water at 10 m above the water-sediment 1 interface. Whereas in models B and C, we calculate the complex vertical particle velocity amplitudes 10 cm above the water-sediment 1 interface and the sea ice-air interface, respectively.

Jensen et.al. [18] writes that the three steps for calculating the wave fields are not independent, with particular emphasis on the frequency and wavenumber sampling. This comes from the fact that when modeling using computers, we cannot integrate a function from $-\infty$ to $+\infty$, which in practice would have taken for ever. Instead we use discrete steps to evaluate

the functions as sums (i.e. instead of integrals), over a representative interval. Therefore, picking the start, steps and end parameters for the radial wavenumbers could be hard for inexperienced users without the usual convergence testing [15, pp. 70–71].

When we model in OASES-OASP, we controlled the frequency and wavenumber sampling by a numerical integration regime used to evaluate the respective transforms, see more in Jensen et.al. [18, ch. 4]. In OASES-OASP, this is done by the input option "$NW = -1$" (ref. appendix E), which automatically activates the so-called *Complex frequency integration contour* [15, pp. 8-9]. When the complex frequency integration contour is chosen, it calculates a range of phase velocities that are necessary to calculate the wavefield. The maximum and minimum radial wavenumbers are then determined by the minimum- and maximum phase velocities, named $CMIN$ and $CMAX$, respectively, in OASES-OASP [15, p. 70]. $CMIN$ and $CMAX$ are then used to calculate the minimum and maximum radial wavenumbers as a function of the center frequency of the source, named $FREQ$ in OASES-OASP [15, p. 70]. Then the following equations for minimum and maximum radial wavenumbers given in [15, p. 70], as in equations (5.13) and (5.14),

$$(k_r)_{min} = \frac{2\pi \cdot FREQ}{CMAX} \tag{5.13}$$

$$(k_r)_{max} = \frac{2\pi \cdot FREQ}{CMIN}. \tag{5.14}$$

respectively, determine the minima and maxima. In our input files, we used a source with center frequency 10 Hz.

5.3 OASES-OASP model A

When running the input environmental model in table 5.1 in OASES-OASP, we used the 'run_model.csh' script given in appendix F, with the receiver array for model A given in table 5.2. From the automatic wavenumber sampling regime, we got the parameters given in table 5.3,

Table 5.3: Parameters from the automatic wavenumber sampling regime for OASES-OASP model A. The center frequency of the source was set to 10 Hz at 4 m water depth.

	Frequency (Hz)	Phase velocity (m/s)	Rad. wavenumber (rad/m)	Time (s)	Range (m)
Min	1.0	10.0	$2 \cdot 10^{-9}$	0.0	0
Step	0.06	-	-	0.001	1
Max	40.0	$4 \cdot 10^{9}$	6.3	16	501

The radial wavenumbers in table 5.3 are calculated using equations (5.13) and (5.14) with

center frequency for the source, $FREQ$ = 10 Hz. Unfortunately, we did not figure out how to extract the k_r-wavenumbers from OASES-OASP, to for example plot the k_r wavenumber amplitudes.

After OASES-OASP finished calculating the transfer functions, we were directed to the OASES Pulse Post-processor (PP), where several options in OASES PP were controlled by the 'run_model.csh' code. Using the OASES manual given in [15, pp. 149-150], the following was done in OASES PP,

- 1: filename -> "OASES_Svea_AG2_OBN_hydro_shot_183.trf".
- 2: Source type -> 1 (Explosive source (default) normalized to unit pressure at 1 m distance).
- 11: Range stacked.
- 18: Trace file -> "OASES_Svea_AG2_OBN_hydro_shot_183" (ASCII formatted).
- 19: Return (PP main menu).
- 22: Exit PP.

In OASES PP. the transfer functions from OASES-OASP are convolved with the selected source spectrum, i.e. OASES' "Explosive source (default) normalized to unit pressure at 1 m distance" spectrum. Then the inverse Fourier transform (e.g. given in equation (2.12)) is performed. See more details in the OASES manual [15, ch. 16].

Running the 'run_model.csh' code, the resulting convolved data were saved as ASCII file, i.e. as "OASES_Svea_AG2_OBN_hydro_shot_183.ASCII". This ASCII file was then converted to SU-file by the "asc2su" code, given in appendix G. For plotting/imaging the complex pressure amplitudes, we used the 'plot_seis_OASES_OASP.sh' code given in appendix I. In figure 5.1 we see the shot gather obtained when running OASES-OASP with environmental model given in table 5.1, wavenumber samples given in table 5.3 and receiver array for model A given in table 5.2, with the explosive point source given by OASES-OASP [15, p. 66]. To avoid wrap-around effects, we modeled in OASES-OASP for a total of 10 seconds for each trace, and plotted the results for 6 s. As wee see from figure 5.1, we get some high-amplitude, slowly and dispersive propagating waves (i.e. low group velocities) near the water-sediment 1 interface. Using equation 2.91, we can estimate the group velocities of the waves observed in figure 5.1 as the gradient of straight lines passing through the amplitudes. A very rough estimate based on reading the slopes of the two black dashed lines drawn in figure 5.1, indicate group velocities in the range 80 - 90 m/s.

The respective frequency-wavenumber and frequency-phase velocity spectra of the shot gather given in figure 5.1, are given in figure 5.2. The $(f-k_r)$ and $(f-v_{ph})$ spectra were obtained from running the shell script in appendix I. The $(f-k_r)$ spectrum in figure 5.2) was calculated

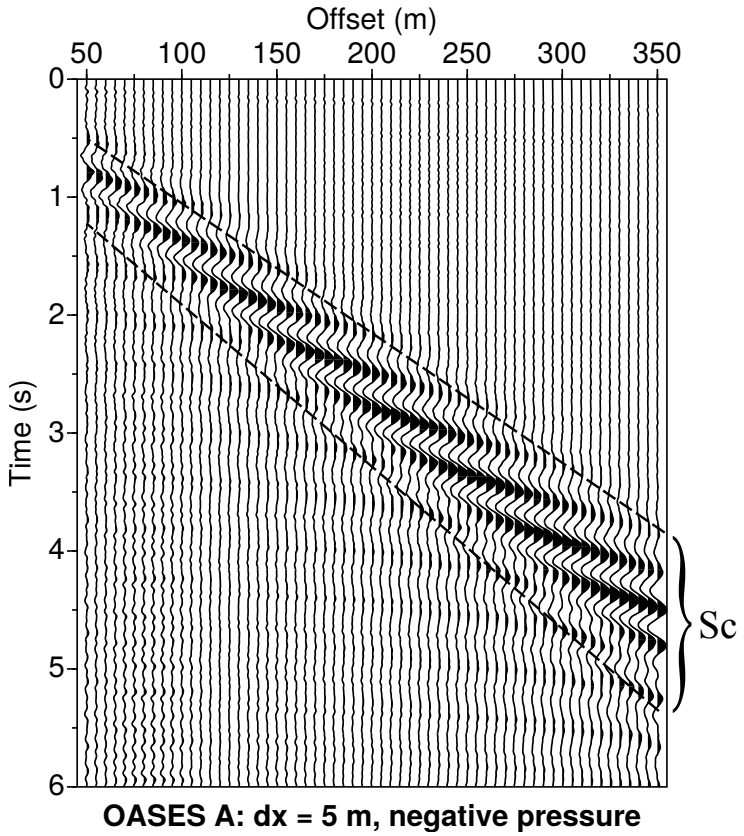

Figure 5.1: Modeled shot gather from running OASES-OASP with the environmental model in table 5.1, and the receiver array for model A in table 5.2. OASES-OASP used the 'N' option to calculate the negative pressure amplitudes ($|-p(k_r,z)|$) at 10 cm above the water-sediment 1 interface. The Scholte waves, inside the dashed black line and marked as "Sc", seem to be highly dispersive. The spatial distance between each trace is 5 m.

using the SUSPECFK code, implemented in CWP/SU by Stockwell [70]. The SUSPECFK code transforms the negative pressure amplitudes in the $(x-t)$ domain to the $(f-k_r)$ domain by using the *2-D Fourier transform*, see for example Bracewell [78, p. 241]. Be aware that for a given phase, the SUSPECFK code uses the relation given in equation (4.3), and therefore all frequency-wavenumber images in this thesis are given with wavenumbers having (1/m) as unit, and not (rad/m), which is more common. The $(f-v_{ph})$ spectra is obtained by using the SUPHASEVEL code, implemented in CWP/SU by Liner [44]. The SUPHASEVEL code transforms the negative pressure amplitudes into the $(f-v_{ph})$ using theory given in Park et.al. [43]. The white dashed line in figure 5.2b) indicates the resolution limit due to spatial aliasing, which is in agreement with Johansen & Ruud [1, figure 6]. It is based on Foti et.al. [46] and unwrapping radial wavenumbers from $-k_{ny} \leqslant k < k_{ny}$ to $0 \leqslant k \leqslant 2k_{ny}$. Instead of letting $k > k_{ny}$ be the limit for spatial aliasing, we let $k > 2k_{ny}$ be the limit. Hence we get the

relation given in equation (5.15),

$$\left(v_{ph}\right)_{max} = \frac{2\pi\ f_{max}}{2 \cdot k_{ny}} = f_{max}\ \Delta x \tag{5.15}$$

where we see that $\left(v_{ph}\right)_{max} \propto f_{max}$ for constant Δx. Therefore waves with maximum frequency 20 Hz and constant receiver interval $\Delta x = 5$ m, using equation (5.15) yields $\left(v_{ph}\right)_{max} =$ 100 m/s, which is the principle used in figure 5.2b) for spatial resolution limit.

As we see from figure 5.2a), most of the higher valued absolute negative pressure amplitudes (red colors) are present for wavenumbers near zero m^{-1}. We also observe some relatively strong amplitudes for negative radial wavenumbers. Why we get these strong amplitudes for negative wavenumbers, can be hard to tell. That is because when we presented the theory behind the wavenumber integration method, we limited the coordinate system to cylindrical coordinates for $r > 0$, ref. chapter 2.3. Then, when we introduced the Hankel transform pairs in equations (2.17) and (2.18), and later the solution to the wavenumber integral (i.e. a Hankel transform of the depth-dependent Green's function given in equation (2.36), we defined the wavenumber integrals for only positive radial wavenumbers. And since OASES-OASP uses this method, negative radial wavenumbers should not be obtained following the integral representations. However, Jensen et.al. [18, ch. 4.5] discuss how aliasing effects occur when applying the fast field programs, and how negative wavenumbers might occur in the OASES-OASP model when solving for the discretized solutions to the wavefield. For our purpose, if we could be able to get the radial wavenumber amplitude spectra from OASES-OASP, we would be able to analyzed if the negative amplitudes originate from negative radial wavenumbers.

In the $(f - v_{ph})$ spectrum given in figure 5.2b), we see the fundamental mode having relatively larger amplitudes for frequencies in the relatively small bandwidth 3 Hz to 5 Hz, with corresponding phase velocities of approx. 150 m/s to above 500 m/s. According to Johansen et.al. [1], who constructed the environmental model in table 5.1, but without the ice layers, they measure Scholte waves in the same frequency interval, but with slightly lower phase velocities. In figure 5.2b), we have also indicated two possible Scholte wave harmonics, as "Sc2?" and "Sc3?", i.e. Scholte waves with higher frequency and phase velocity components. These higher harmonics might be what we see as the "dipping" trends in figure 5.2a) for higher frequencies. The arrows and numbers in figure 5.2a), are to indicate regions for discussion. The one marked as "Sc?" is a prediction that this high amplitude area has a relation to the fundamental Scholte wave mode. Given the frequency-phase velocity spectrum in figure 5.2b), we can see that most of the energy is associated to the same bandwidth in figure 5.2a).

5.4 OASES-OASP model B

Here, we run the same input environmental model in table 5.1 and water thickness as in model A. The difference is that in model B we calculate the vertical particle velocity amplitudes, instead of the negative pressure as in model A. The automatic wavenumber sampling regime in OASES-OASP, yields the radial wavenumber interval given in table 5.4 for model B,

Table 5.4: Parameters from the automatic wavenumber sampling regime for OASES-OASP model B. The center frequency of the source was set to 10 Hz at 4 m water depth.

	Frequency (Hz)	Phase velocity (m/s)	Rad. wavenumber (rad/m)	Time (s)	Range (m)
Min	1	10	$2 \cdot 10^{-8}$	0.0	0
Step	0.06	-	-	0.001	1
Max	40	$4 \cdot 10^{9}$	6	16.4	501

By comparing table 5.3 with table 5.4, we see that they're completely the same. Hence, it seems that the automatic wavenumber sampling regime in OASES-OASP is independent on which component is calculated.

The shot gather for model B is given in figure 5.3. As wee see from figure 5.3, the shot gather is very similar to the shot gather given in figure 5.1. This might indicate that measuring the response from calculating the negative pressure at the seabed is similar to calculating the vertical particle velocity at the seabed. To get more information from the shot gather in figure 5.3, we transform the amplitudes to the frequency-wavenumber and frequency-phase velocity domains, as we did for model A, i.e. we used the same processing techniques. We can now examine the different responses from calculating the amplitudes based on negative pressure versus vertical particle velocity.

The resulting $(f - k_r)$ and $(f - v_{ph})$ spectra of shot gather in figure 5.3 are given in figure 5.4. Comparing the $(f - k_r)$ spectrum in figure 5.2a) with the $(f - k_r)$ spectrum in figure 5.4a), we see that the calculated complex amplitudes are higher and more concentrated on the fundamental mode in figure 5.4a). By comparing the $(f - v_{ph})$ spectra in figures 5.2b) and 5.4b), we see that the first harmonic mode has higher complex amplitudes in figure 5.4b). The higher complex amplitude region (red), also result in slight lowering of the highest amplitudes for lower phase velocities in figure 5.4b). Hence, when modeling, and potentially measuring, Scholte waves close to the seabed, vertical particle velocity may yield more concentrated information about the fundamental Scholte wave mode.

5.5 OASES-OASP model C

In OASES-OASP model C, we run the input environmental model in table 5.1 with water layer thickness of 31.1 m, instead of 19.1 meter as in models A and B. The change in water

thickness was done to relate to the averaged experimental water depth given in chapter 6.2. The automatic wavenumber sampling regime in OASES-OASP, yields the radial wavenumber interval given in table 5.5 for model C,

Table 5.5: Parameters from the automatic wavenumber sampling regime for OASES-OASP model C. The center frequency of the source was set to 10 Hz at 4 m water depth.

	Frequency (Hz)	Phase velocity (m/s)	Rad. wavenumber (rad/m)	Time (s)	Range (m)
Min	1.0	10.0	$2 \cdot 10^{-9}$	0.0	0
Step	0.06	-	-	0.001	1
Max	40.0	$4 \cdot 10^{9}$	6.3	16	501

By using the receiver array for model C given table 5.2, the shot gather in figure 5.5 is obtained. In figure 5.5, when calculating the vertical particle velocity amplitudes on floating sea ice, we observe other wave phenomena compared to at the seabed in models A and B. For this receiver model, we have a very complex situation where the boundary conditions for fluid-solid interfaces, i.e. continuity of vertical displacement, u_z, continuity of normal stress, σ_{zz}, and vanishing shear stress, σ_{rz}, all must be fulfilled on both sides of the water layer. With theory from Lamb [79, 80], Ewing [41] showed that if the wavelengths are large compared to the thickness of the floating sea ice, flexural waves will occur. The flexural waves originate from the so-called anti-symmetric Lamb modes, whose average displacements are in the transverse direction according to Lamb [79, 80]. The highest amplitudes observed in figure 5.5, which have a fan like shape, must therefore be associated to flexural waves. Johansen et.al. [5, figure 7] have presented a comparable modeled shot gather displaying flexural waves.

The resulting $(f - k_r)$ and $(f - v_{ph})$ spectra of shot gather in figure 5.5 are given in figure 5.6. The $(f - v_{ph})$ spectrum in figure 5.6b) shows a complicated pattern with many phase velocities present close to zero frequency and zero phase velocity. Additionally, from figure 5.6b), we can glimpse the flexural wave in the phase velocity spectrum (marked as "F"), which tends to converge to zero phase velocity for lower frequencies [5]. By comparing the $(f - k_r)$ and $(f - v_{ph})$ spectra obtained close to the fluid-solid interfaces in chapters 5.3 and 5.4, with the spectra obtained in figure 5.6, we observe more complicated and smeared patterns in figure 5.6. Using Foti et.al. [46], we can clearly see in the $(f - k_r)$ spectrum in figure 5.6a) aliasing effects, where positive wavenumbers are mapped as negative. For the previous models A and B, such aliasing effects were not as prominent.

5.6 Summary of OASES-OASP results

The modeled shot gathers obtained from using the wavenumber integration technique OASES-OASP on the environmental model in table 5.1, show some of the expected wave phenomena

encountered in shallow-water Arctic seismic experiments on floating sea ice, ref. figure 1.1. When complex amplitudes (i.e. pressure or vertical particle velocity) are calculated close to the water-seabed interface, the shot gathers in figures 5.1 and figure 5.3, and the $(f - v_{ph})$ spectra in figure 5.2b) and figure 5.4b), show prominent dispersive Scholte waves, if compared to results given in Johansen et.al. [1]. This indicates that if the environmental model in table 5.1 is representative for the study area (outlined in figure 1.2), we should expect to measure dispersive Scholte waves close to the seabed in this area.

All $(f-k_r)$ spectra in figures 5.2a, 5.4a and 5.6a, show amplitudes for negative radial wavenumbers. According to Foti et.al. [46], these amplitudes for negative radial wavenumbers are related to noise and aliasing events. Foti et.al. [46] also comments that in practice, when limiting the extension of the receiver array, strongly influences on the results obtained in $(f - k_r)$-analysis. Hence, the total length of the receiver array influences on the resolution in the $(f - k_r)$-domain.

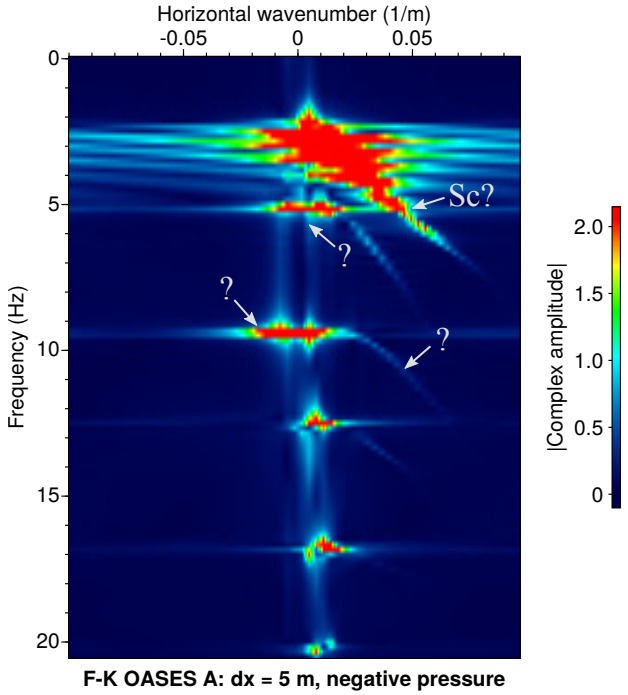

(a) $(f - k_r)$ spectrum

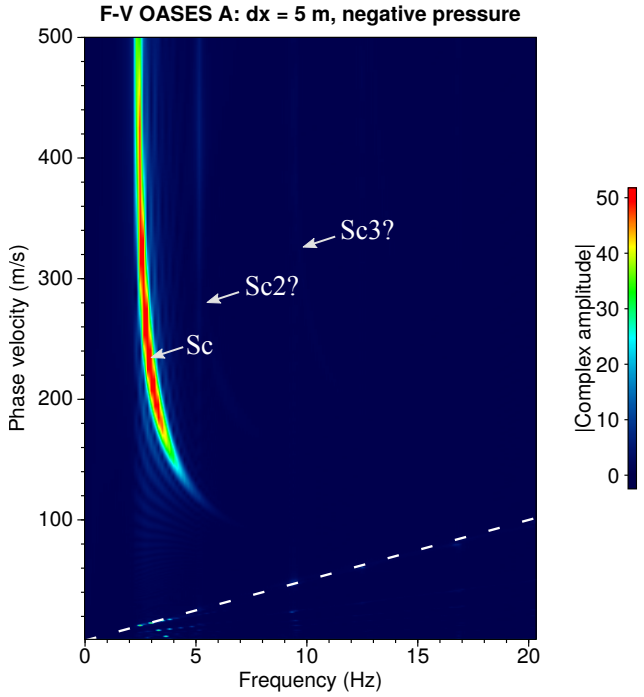

(b) $(f - v_{ph})$ spectrum

Figure 5.2: Resulting (a) frequency-radial wavenumber and (b) frequency-phase velocity spectra of the modeled shot gather in figure 5.1, where the complex amplitudes for negative pressure, $|-p(k_r, z)|$, are colored according to low (dark blue) and high (red). In (b) we see the first fundamental Scholte wave mode marked as "Sc", with some possible (lower amplitude) higher harmonics, "Sc2?" and "Sc3?". The white dashed line in (b) indicates the resolution limit due to spatial aliasing.

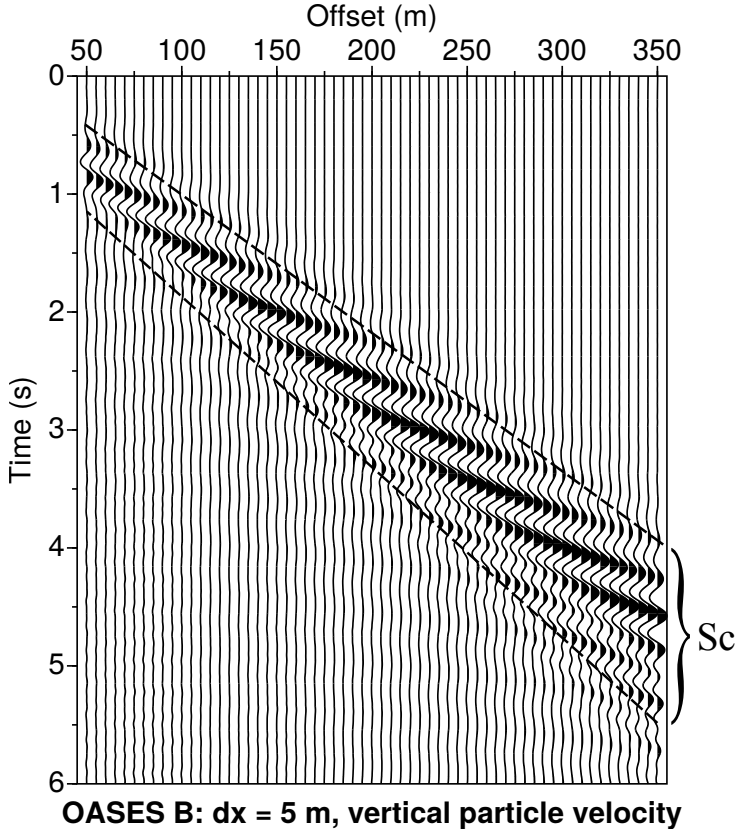

Figure 5.3: Modeled shot gather from running OASES-OASP with the environmental model in table 5.1, for the receiver array defined for model B in table 5.2, with water layer thickness 19.1 m. OASES-OASP used the 'V' option to calculate the complex amplitudes for vertical particle velocity ($v_z(k_r, z)$) at 10 cm above the water-sediment 1 interface. The Scholte waves, inside the dashed black line and marked as "Sc", seem to be highly dispersive. The spatial distance between each trace is 5 m.

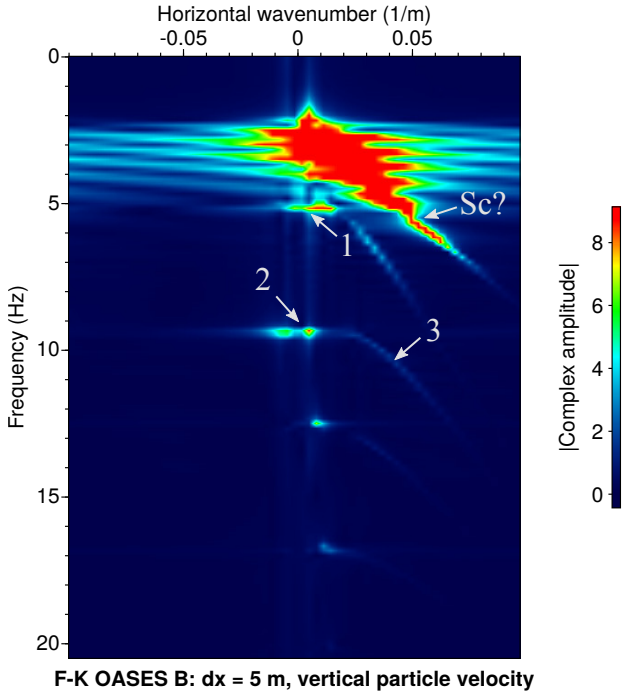

(a) $(f - k_r)$ spectrum

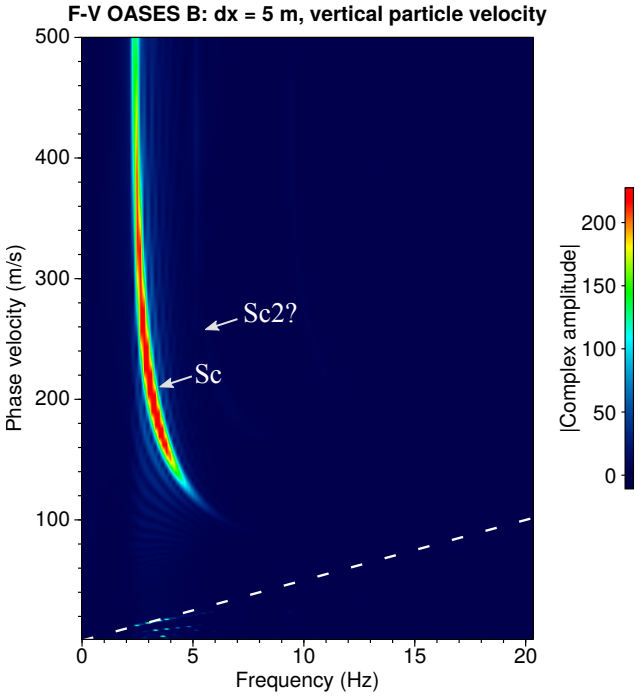

(b) $(f - v_{ph})$ spectrum

Figure 5.4: Resulting (a) frequency-radial wavenumber and (b) frequency-phase velocity spectra of the modeled shot gather in figure 5.3, where the complex amplitudes for vertical particle velocity, $|v_z(k_r, z)|$, are colored according to low (dark blue) and high (red). In (b) we see the first fundamental Scholte mode marked as "Sc", with a possible (lower amplitude) higher harmonic, "Sc2". The white dashed line in (b) indicates the resolution limit due to spatial aliasing.

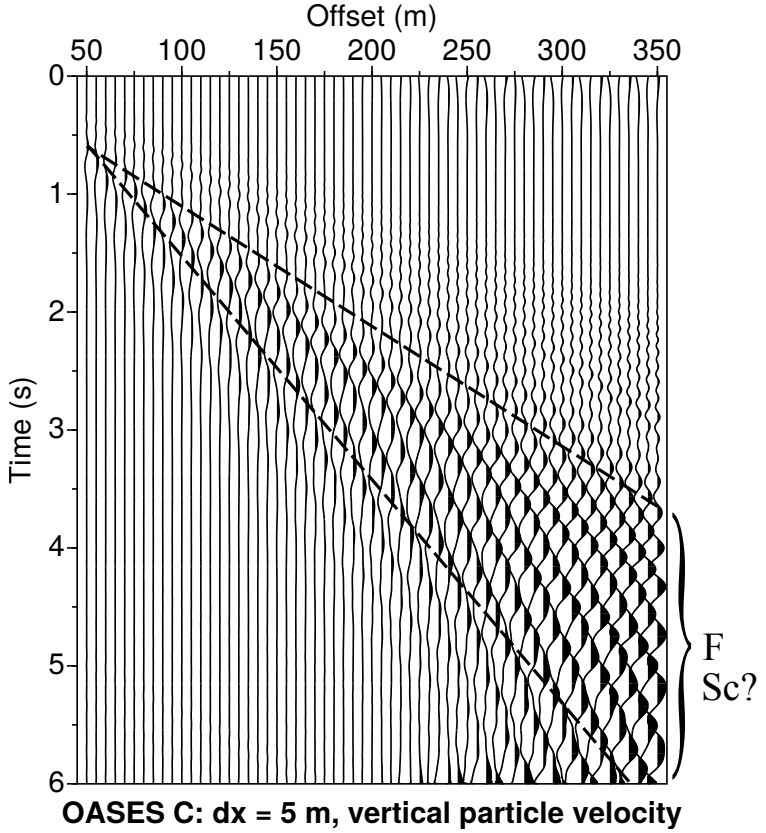

Figure 5.5: Modeled shot gather from running OASES-OASP with the environmental model in 5.1, for the receiver array defined for model C in table 5.2 with water layer thickness 31.1 m. OASES-OASP used the 'V' option to calculate the complex amplitudes for vertical particle velocity ($|v_z(k_r, z)|$) at 5 cm below the sea ice top-air interface. The flexural waves ('F') and possible Scholte waves ('Sc') are marked in the figure. The spatial distance between each trace is 5 m.

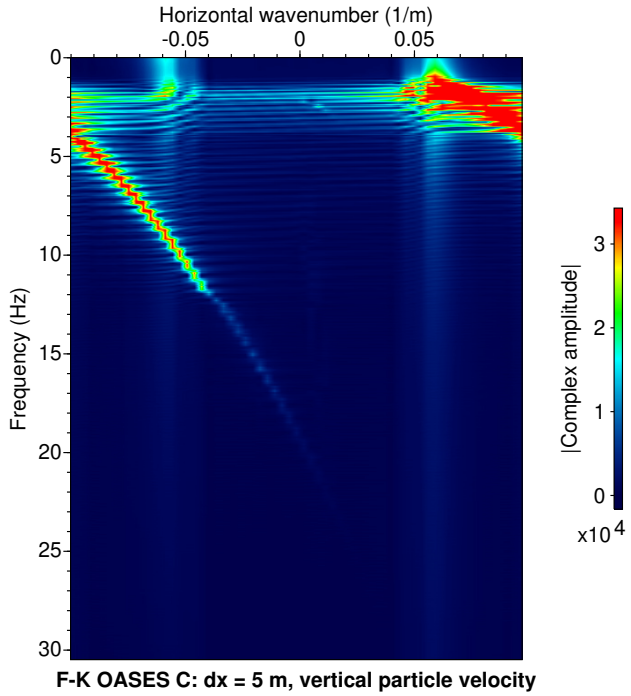

(a) $(f - k_r)$ spectrum

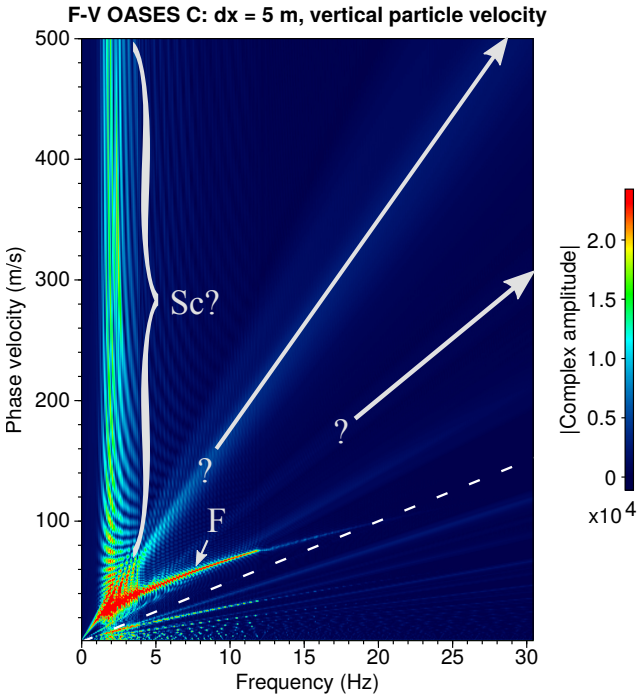

(b) $(f - v_{ph})$ spectrum

Figure 5.6: Resulting (a) frequency-radial wavenumber and (b) frequency-phase velocity spectra of the modeled shot gather in figure 5.5, where the complex amplitudes for vertical particle velocity, $|v_z(k_r, z)|$, are colored according to low (dark blue) and high (red). F: Flexural waves, 'Sc?': possible dispersive Scholte waves?, '?': unknown effects. The white dashed line in (b) indicates the resolution limit due to spatial aliasing.

Chapter 6

Experimental results

Processed shot gathers, frequncy-wavenumber and frequency-phase velocity spectra from the experimental Svea 2018 seismic experiment will be presented in this chapter. The measured amplitudes obtained from using the Bolt LLX 1900 (AG2) airgun source and 4C Ocean-bottom node (OBN) receivers, and the Sercel mini G (AG) airgun source and three component geophones (3C) receivers will be presented here. The AG-3C results will be presented to illustrate measurements of ice flexural on top of the sea ice.

The four component OBN datasets are recorded as receiver gathers, which do not follow the SEG-Y standard given in [65]. This complicates the reading of the SEG-Y rawdata, but does not diminish the results. Since the OBNs are four component receivers (e.g. containing one hydrophone and three geophones), we used the SU-keyword ”trid” (trace identification code) with bytes 11 (seismic pressure sensor) and 12-14 (multi component seismic sensor for vertical- (11), cross-line- (12) and in-line (13) components) when calling the headers from the SEGY-files.

In the script given in appendix J, the processing techniques used in CWP/SU when processing the AG2 OBN (hydrophone) data are documented. Here is a list of the processing techniques used:

- SUGAIN: tpow = 1: t-squared gain correction with $t = 1$ as the exponential.
- SUFILTER: Omrsby bandpass filter with filter coefficients: [1, 2, 20, 40] Hz.
- SUSTACK: stacking multiple shots with same offsets.

The script in appendix J could be used as reference for processing the results for the AG2 OBN (three component geophone) data.

In the script given in appendix K, the processing techniques used in CWP/SU when processing the AG 3C data are documented. Here is a list of those processing techniques used:

- SUGAIN: tpow = 1: t-squared gain correction with $t = 1$ as the exponential.

- SUGAIN: pbal = 1: balance traces by diving by the RMS of trace the respective trace
- SUFILTER: Omrsby bandpass filter with filter coefficients: [1, 2, 20, 40] Hz.
- SUABSHW: key = offset: replace the amplitudes by their absolute value.

We chose to process and plot the results measured from node positions (i.e. shot point positions) 183 and 138 for the AG2 and AG datasets, respectively. This was because at these two shot point positions, prominent Scholte- and ice flexural waves were detected in the shot gathers. Other shot point positions in these measured datasets could also be of interest, e.g. shot point position 182 showing prominent Scholte waves and 140 showing prominent ice flexural waves. Due to technical issues with the smaller Sercel Mini G airgun at node position 46 [20], the airgun was replaced a larger Bolt LLX 1900 airgun, and all subsequent airgun shots were conducted using the AG2 airgun. Consequently, since the two airguns do not have the same specifications (see table D.1), the responses can not be compared to full extent. This follows for example from the depth-separated Helmholtz equation in equation (2.20), where the right side of the equation represents the source term. On the other hand, we can compare the measured amplitudes from measuring negative pressure versus measuring vertical particle velocity at the seabed.

6.1 Comparison of negative pressure and vertical particle velocity measured at the seabed using ocean-bottom nodes

By using the script in appendix J for shot position (i.e. node position) number 183 with the Bolt LLX 1900 airgun as source and OBN - hydrophones as receivers, the shot gather in figure 6.1 is obtained. For the same shot position number, the same airgun source and same receiver intervals, but with OBN three component geophones as receivers, the shot gather in figure 6.2 is obtained. In shot point 183, the water column thickness was assumed to be 10-12 m, and the average water depths for the OBN receivers was approximately 19 m (ranging from approx. 10 to 26 m).

In figure 6.1 we see the first arrivals having a group velocity of approximately 1500 m/s (blue), indicating the measured water pressure wave $U_{p,2}$ = 1500 m/s. This event is not seen in figure 6.2. The red lines in figure 6.1 and figure 6.2, indicate group velocities of U_2 = 34.8 m/s and U_3 = 37.8 m/s, respectively, which suppose to indicate group velocities for the observed Scholte waves. We think we have Scholte waves in these measurements, among others, since the theory by Vinh [29] state that at all fluid-solid interfaces, Scholte waves are generated. Additionally, the measured shot gathers showing these relatively slowly propagating, high amplitude waves, are comparable to Scholte waves measurements given in Johansen et.al. [4, 1]. An interesting observation from figures 6.1 and 6.2, is that there seem to be two Scholte waves, one arriving approximately 1.5 seconds after, and with slightly larger group velocity

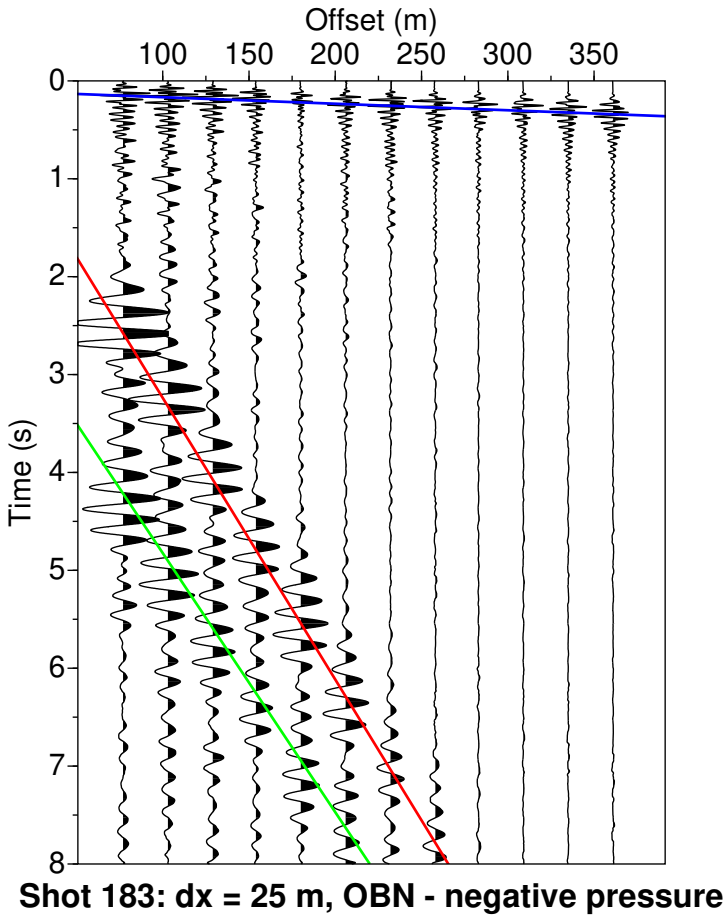

Figure 6.1: Shot gather for shot position 183 from the Svea 2018 seismic experiment, where Bolt LLX 1900 airgun was source (submerged 4 m water depth) and OBN hydrophones were receivers with receiver intervals $\Delta x = 25$ m. The OBN hydrophones measured the negative pressure as function of time at the seabed. Group velocity lines: $U_1 = 1500.0$ m/s (blue), $U_2 \approx 34.8$ m/s (red), $U_3 \approx 37.8$ m/s (green).

(green line) than the other (red line). To determine the group velocities of the Scholte waves based on curve fitting with the highest amplitudes observed, can be risky. That is because spatial aliasing effects, which it seems that we have in these shot gathers. Specifically, will the relatively large receiver intervals make the decision-making of the slopes of the lines hard to define, since there are relatively long intervals between the traces. Although determining the group velocities by curve-fitting based on the highest amplitudes is risky, it might give an estimate of the group velocities. Johansen & Ruud [1] reported on Scholte waves with group velocities near 40 m/s close to the study area for the Svea 2018 experiment, which is close to our estimated Scholte wave group velocities, taking into account the uncertainties from estimating the curves in the shot gathers.

For low time-intervals, i.e. approx. 0.5 s to approx. 1.5 s, in figures 6.1 and 6.2, we think the recorded amplitudes originate from some noise contributions from the surroundings.

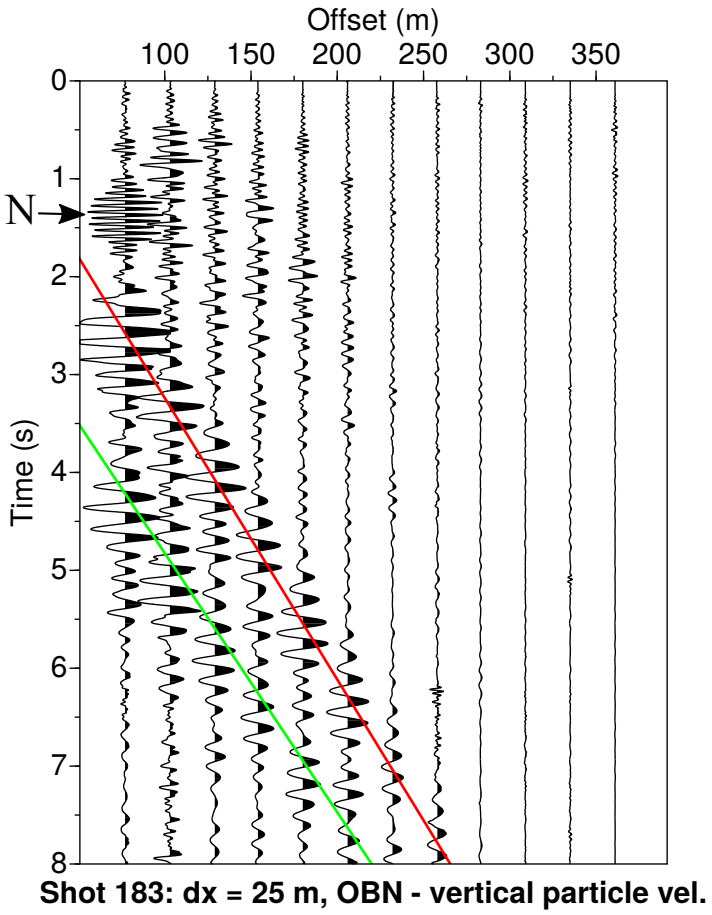

Figure 6.2: Shot gather for shot position 183 from the Svea 2018 seismic experiment, where Bolt LLX 1900 airgun was source (submerged 4 m water depth) and OBN 3C geophones were receivers with receiver intervals $\Delta x = 25$ m. The average water layer thickness for this shot gather was 19 m. The OBN three component geophones measured the vertical particle velocity as function of time at the seabed. Group velocity lines: $U_1 = 1500.0$ m/s (blue), $U_2 \approx 34.8$ m/s (red), $U_3 \approx 37.8$ m/s (green). N: Noise burst.

In figure 6.2 we see a recorded high-amplitude event at the first trace at approximately 1 second, which lasts for approximately 0.8 seconds. Johansen & Ruud [1, figure 5] reported on similar event, but recorded on top of the sea ice layer, naming it *noise burst*. If this is a noise burst, it could have been filtered out by for example trace editing when processing, but the event was included for here discussion. It is interesting that we measured the noise burst for measured vertical particle velocity, but not for measured negative pressure. Especially since the recording was conducted with the same OBN measurement devices, it measured at the same time and at the same location. What's causing these noise bursts is uncertain. One hypothesis which has been discussed in the Geophysics group leaded by prof. Tor Arne Johansen (UiB), is that small Arctic organisms (e.g. snails, crabs, fish, etc.) could be settling in and on the receivers before measuring. If so, the organic organisms could act as added loads which might be recorded by the submerged measurement devices.

The $(f-k)$ spectra for the shot gathers given in figures 6.1 and 6.2, are given in figures 6.3a) and 6.3b), respectively. As we see from the $(f-k)$ spectra in figure 6.3, the amplitudes (i.e. $|-p|$ in figure 6.3a and $|v_z|$ in figure 6.3b) are concentrated within a narrow-band interval of approximately 4 Hz to approximately 6 Hz. Comparing the $(f-k)$ spectra in figures 6.3a and 6.3b, to the $(f-k_r)$ spectra in figures 5.2a and 5.4a, we see that the measured $(f-k)$ domains seem to have much more aliasing effects present. Additionally, we observe that the amplitudes are orders of magnitude higher for the measured $(f-k)$ spectra compared to the modeled spectra.

For receiver interval $\Delta x = 25$ m, using equation (5.12) yields the Nyquist wavenumber $K_{ny} = 0.02$ m, which is seen as the $\pm$ extreme wavenumbers in figure 6.3. From theory of spatial aliasing in chapter 2.10, by reducing the receiver intervals, increases the Nyquist wavenumber and spatial aliasing effects can be dampen [46]. Additionally, using the theory in Foti et.al. [46], we can unwrap the negative frequencies to the interval $(K_{ny}, 2K_{ny})$ assuming we know the direction of propagation, which might help to increase resolution of the $(f-k)$ domains.

The $(f-v_{ph})$ spectra for shot gathers in figure 6.1 and figure 6.2, are given in figures 6.4a) and 6.4b), respectively. From the $(f-v_{ph})$ spectra in figures 6.4a) and 6.4b), we see that for the bandwidth 2 Hz to 4 Hz, phase velocities below 50 m/s to 100 m/s, respectively, are below the resolution limit due to spatial aliasing. Consequently, Scholte waves with such frequencies and phase velocities are spatially aliased. We have already seen in the $(f-k)$ spectra in figure 6.3 that the data is suffering from spatial aliasing effects, hence, a narrower receiver interval than 25 m may be preferred when measuring Scholte waves at the seabed.

Compared to the modeled shot gather in figure 5.1 for negative pressure, we observed that most of the Scholte phase velocities were in the range 170 to above 400 m/s in the bandwidth 2 Hz to 4 Hz. In figure 5.3 for vertical particle velocity, we observed that most of the Scholte wave phase velocities were in the range 140 m/s to approximately 400 m/s, for the same bandwidth 2-4 Hz. Due to spatial aliasing effects in measured data sets, we cannot say if the environmental model presented in chapter 5.2 is representable for the study area. But from comparing the modeled and measured $(f-v_{ph})$ spectra, we can see that the bandwidths coincide, which at least can indicate that Scholte waves are both modeled and observed.

6.2 vertical particle velocity measured on top of sea ice

Three component geophones placed on top of floating sea ice can be used to measure ice flexural waves [5]. A shot gather for when measuring the vertical particle velocity amplitudes at shot position 138 (i.e. 1125 m away from shot position 183) using the Sercel Mini G airgun source, is given in figure 6.5. In figure 6.5 we see the first high-amplitude arrivals, which indicate the direct compressional wave traveling within the sea ice. The ice flexural

waves have the fan-like character, which propagate with higher velocity than the Scholte waves [5]. At offset value 337.5 m there is a bad trace detected, meaning a dis-functional or not correctly orientated receiver. That specific 3C geophone receiver could have been tilted when measuring, causing the more or less random amplitudes recorded. This specific trace could have been muted when processing, but is presented here as an example of a bad trace.

The resulting $(f-k)$ and $(f-v_{ph})$ spectra of the shot gather in figure 6.5 is given in figure 6.6. Figure 6.6 show flexural waves for frequencies in the interval 15 Hz to 30 Hz, maybe strongest amplitudes in the 20 Hz to 25 Hz band. From figure 6.6a, we see that at larger frequencies, i.e. 20 - 25 Hz, we have some vertical particle velocity amplitudes which are recognized as the ice flexural waves in figure 6.5. These amplitudes are under the resolution limit for spatial aliasing, hence the flexural waves are spatially aliased.

In figure 6.6a), we see the characteristic dispersion property of Scholte waves for bandwidth 2 Hz to 8 Hz. According to Johansen & Ruud [1], for low frequencies and thin water layers, we should be able to measure Scholte waves using geophones on place on top of the sea ice. By a bandpass filter, one could separate the Scholte waves from the flexural waves given in figure 6.6b, since they are band-limited.

6.3 Reducing aliasing effects from modeling in OASES-OASP with different receiver intervals

The measured results in chapter 6.1 showed prominent aliasing effects when measuring Scholte waves at the seabed. Foti et.al. [46] state that resolution in the $(f-k)$ domain is severely reduced from limiting the extension of the array. Hence, to reduce spatial aliasing effects, a long seismic line is preferable. Additionally, one can, to some extent, reduce the spatial aliasing effects by optimal receiver intervals suited for the environment. This in hand, comes with the consequence of having to place out many receivers to avoid resolution loss due to the limited extension of the receiver array. In Arctic climate, known for its harsh and unpredictable climate [81], one must often measure the outcome with the operational cost in field. Hence, a very dense spacing of receivers for a very long receiver array, may be undesired. An alternative could be to model with different receiver configurations to give a fairly good prediction of an optimal survey design suited for an area.

Based on the environmental model in table 5.1, we have therefore used OASES-OASP to calculate the vertical particle velocity 10 cm away form the water-sediment 1 interface, with different receiver intervals. The vertical particle velocity component was chosen, since the 3C geophones in the 4C OBNs best facilitate to measure Scholte waves. If the environmental model in table 5.1 is representable for the study area, the conclusions from this modeling could be used for improving the experimental set up given in figure 4.1.

Since the transfer functions for the individual source-receiver pairs in OASES-OASP are in-

dependent of each others [15], we can model the vertical particle velocity amplitudes for receiver intervals 1 m. Then we can use CWP/SU to determine the receiver intervals, by choosing which traces to be included. In figure 6.7 are the shot gathers obtained when running OASES-OASP script in appendix I, but for vertical particle velocity and changing the receiver intervals. As we see from figure 6.7, narrower receiver intervals yield better resolution and easier determination of group velocities observed. To analyze the effect of changing the receiver interval, we can calculate the $(f-k)$ spectra for the respective shot gathers, given in figure 6.8.

From the $(f-k_r)$ spectra in figure 6.8, when decreasing the receiver interval, the Nyquist wavenumber (associated to the minima and maxima in the $(f-k_r)$ spectra) increases, and spatial aliasing effects from negative horizontal wavenumbers are reduced. In figure 6.8d we see the same $(f-k_r)$ spectrum as presented in chapter 5.4. From figure 6.8d, we see that the highest amplitudes (red) are not wrapped for negative wavenumbers, hence spatial aliasing effects are avoided. Consequently, receiver intervals of 5 m or less are preferable when modeling Scholte waves. If the environmental model in table 5.1 is representable for the study are, the results in figure 6.8 could indicate that 5 m receiver interval is optimal. Nevertheless, f-k filtering was not applied to any of the results given in this text. For example *dip filtering* [45, ch. 6] could be applied, to suppress other wavenumber components not associated with Scholte waves.

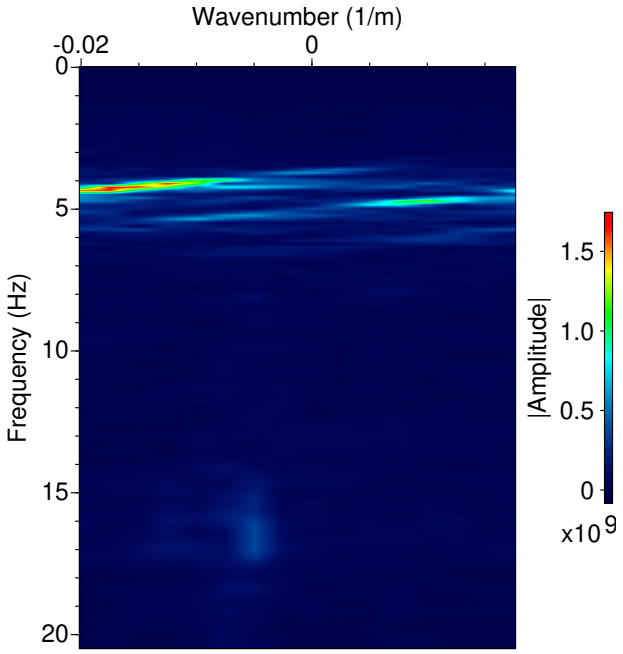

(a) $(f-k)$ spectrum for shot gather in figure 6.1

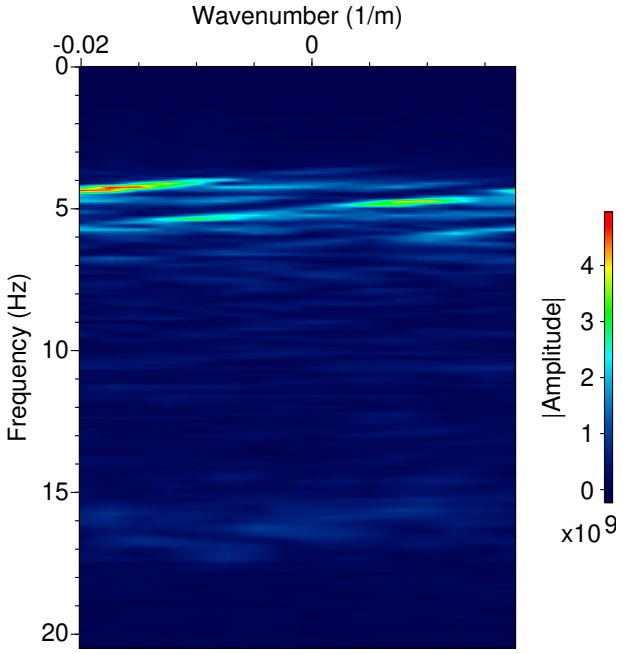

(b) $(f-k)$ spectrum for shot gather in figure 6.2

Figure 6.3: Resulting (a) $(f-k)$ spectrum for shot gather in figure 6.1 and (b) $(f-k)$ spectrum for shot gather in figure 6.2. The average water layer thickness for the respective shot gather was 19 m. In (a) the absolute value of the measured negative pressure is colored from low (dark blue) to high (red). In (b) the absolute value of the measured vertical particle velocity amplitudes are colored from low (dark blue) to high (red).

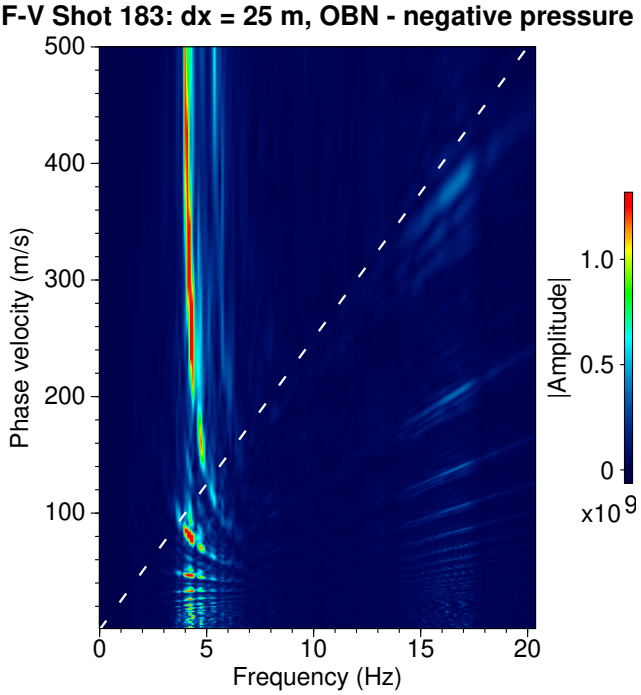

(a) $(f - \nu_{ph})$ spectrum for shot gather in figure 6.1

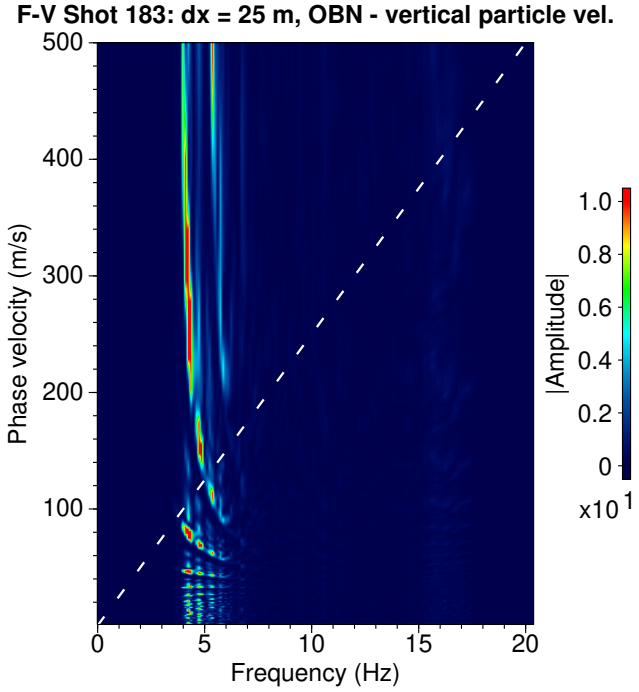

(b) $(f - \nu_{ph})$ spectrum for shot gather in figure 6.2

Figure 6.4: Resulting (a) $(f - \nu_{ph})$ spectrum for shot gather in figure 6.1 and (b) $(f - \nu_{ph})$ spectrum for shot gather in figure 6.2. The average water layer thickness for the respective shot gather was 19 m. In (a) the values for measured negative pressure are colored from low (dark blue) to high (red). In (b) the values for measured vertical particle velocity amplitudes are colored from low (dark blue) to high (red). The white dashed line in the spectra indicate the resolution limit due to spatial aliasing.

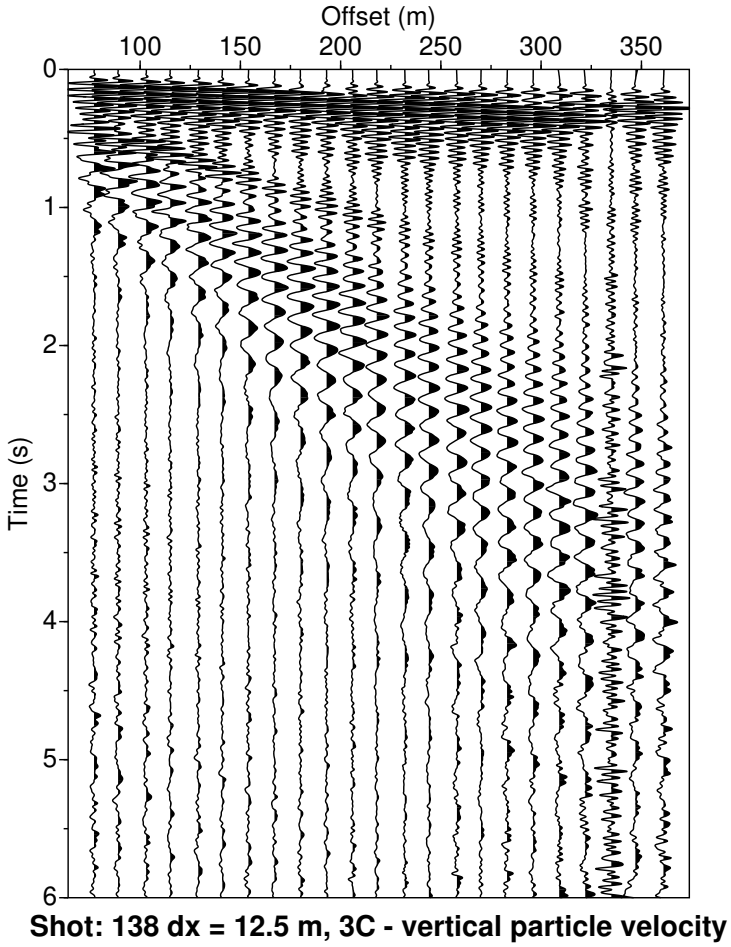

Figure 6.5: Shot gather for shot position 138 from the Svea 2018 seismic experiment, where Sercel Mini G airgun was source (submerged to 4 m water depth) and 3C geophones were receivers with receiver intervals Δx = 12.5 m. The water depth at the source position was measured to 31.2 m, and the average water depth for the shot gather was 32 m (ranging from approx. 30.7 to 33.4 m). The 3C geophones measured the vertical particle velocity amplitudes as function of time on top of the sea ice.

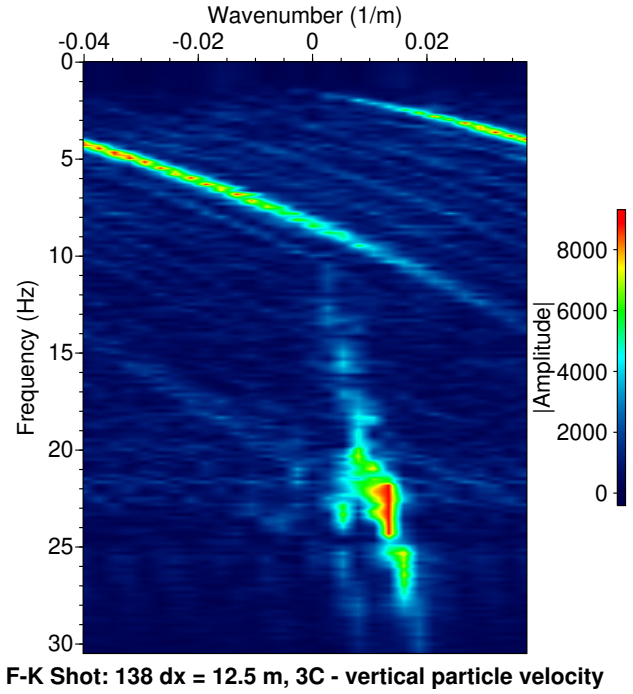

(a) $(f-k)$ spectrum for shot gather in figure 6.5

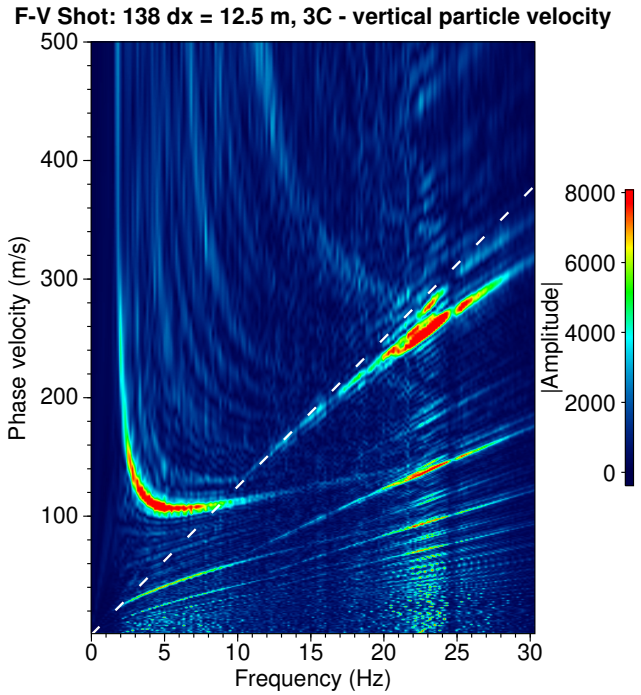

(b) $(f-v_{ph})$ spectrum for shot gather in figure 6.5

Figure 6.6: Resulting (a) $(f-k)$ and (b) $(f-v_{ph})$ spectra of the synthetic shot gather in figure 6.5. The average water depth for the respective shot gather was 32 m. In (a) the absolute value of the measured negative pressure is colored from low (dark blue) to high (red), and in (b) the values for measured vertical particle velocity are colored from low (dark blue) to high (red). The white dashed line in (b) indicates the resolution limit due to spatial aliasing.

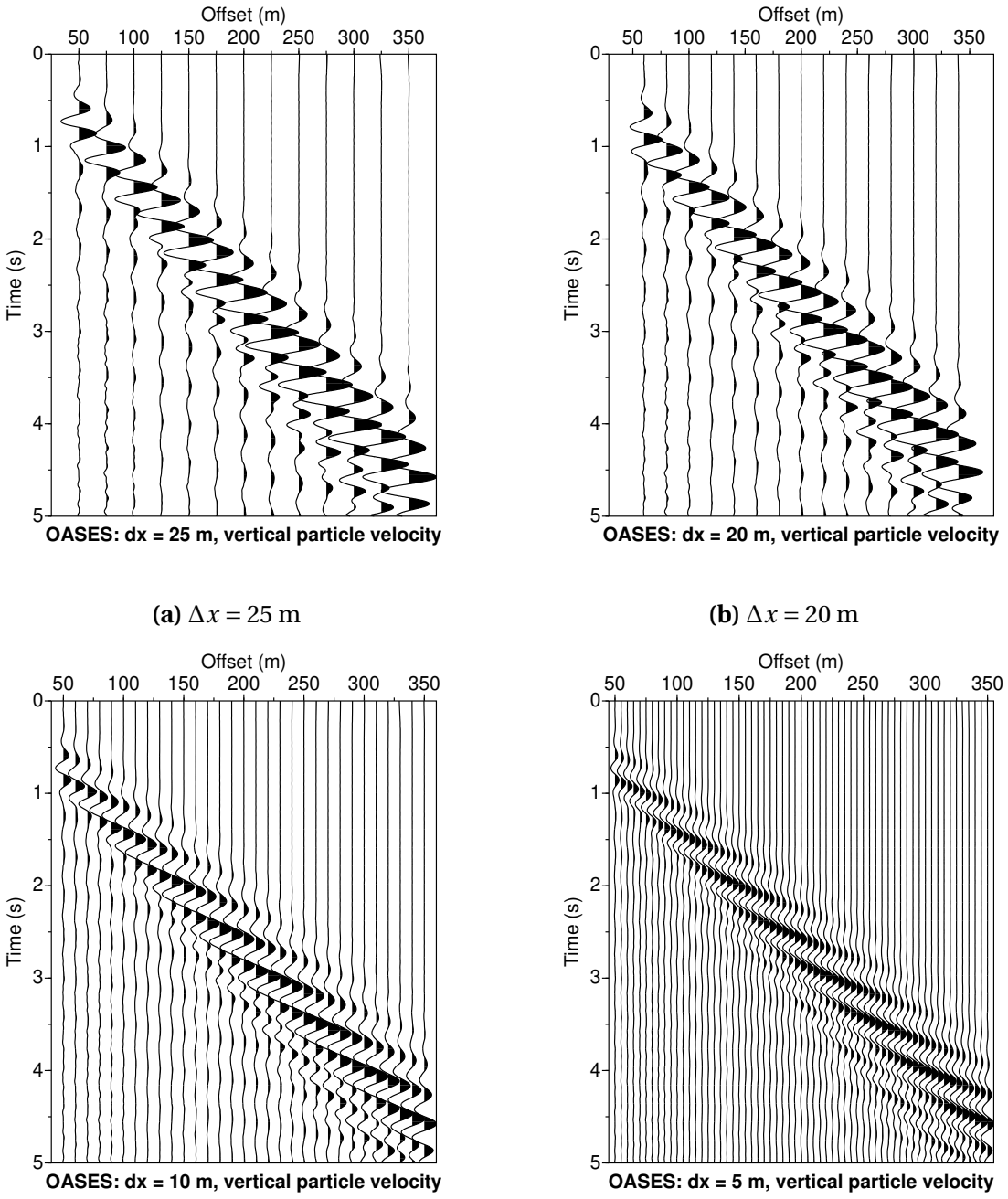

(a) $\Delta x = 25$ m

(b) $\Delta x = 20$ m

(c) $\Delta x = 10$ m

(d) $\Delta x = 5$ m

Figure 6.7: Shot gathers from calculated vertical particle velocities for different receiver intervals using OASES-OASP. The environmental model in table 5.1 is used when modeling, with water layer thickness of 19.1 m. The amplitudes were calculated 10 cm above the water-sediment 1 interface.

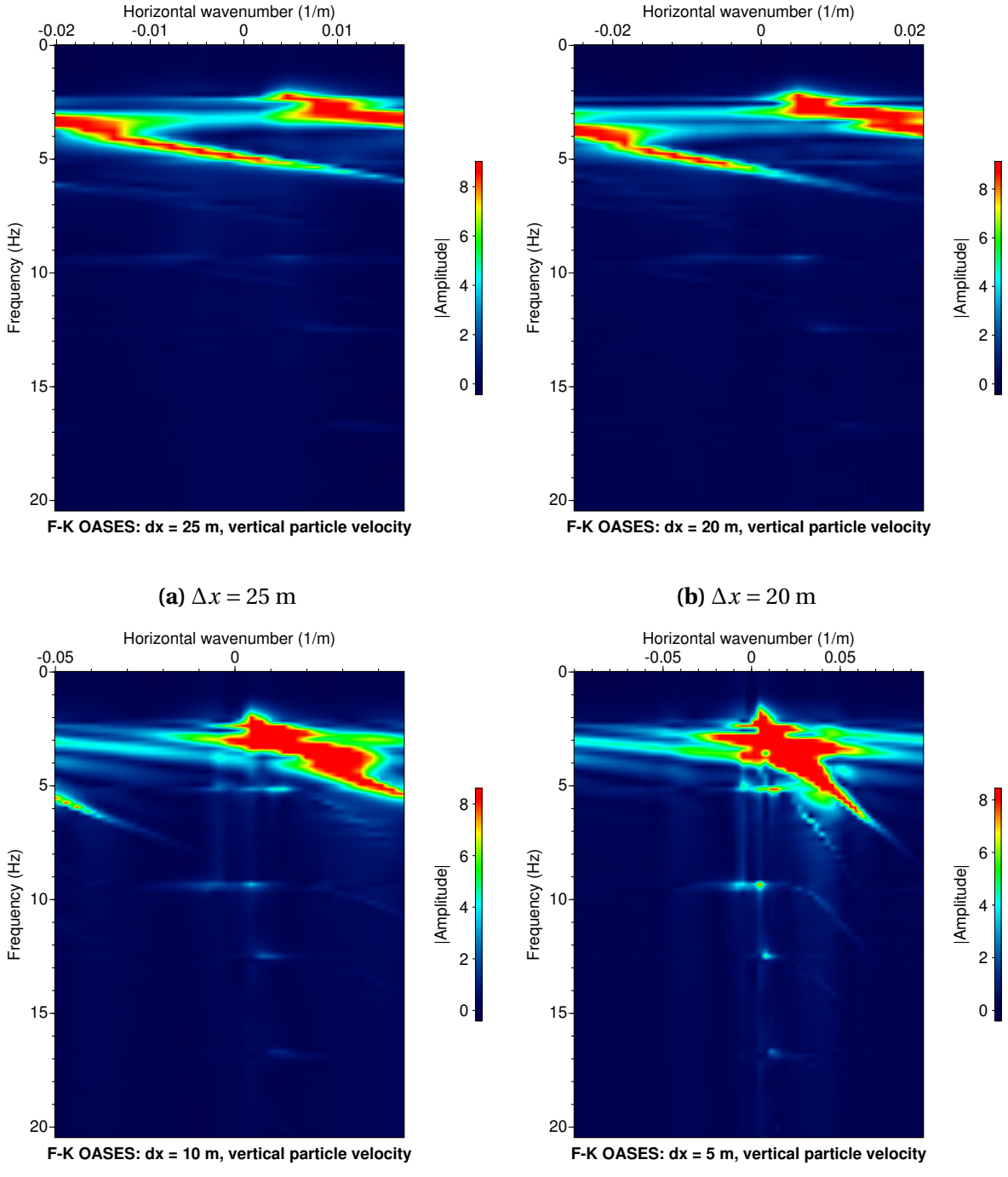

(a) $\Delta x = 25$ m

(b) $\Delta x = 20$ m

(c) $\Delta x = 10$ m

(d) $\Delta x = 5$ m

Figure 6.8: $(f-k)$ spectra for the shot gathers in figure 6.7, with varying receiver intervals. The horizontal wavenumber in this plot, K_r (1/m), relates to k_r (rad/m) by the relation $K_r = k_r/2\pi$, as in equation 4.3.

Chapter 7

Discussion

In chapter 3 we showed that for silicates, i.e. common minerals found in and around Van Mijenfjorden, Svalbard, the v_p/v_s-ratios are orders of magnitudes larger than for more compact sediments, which is in correspondence with Johansen & Ruud [1]. Consequently will water filled silicates loose its shear strength as water inclusions are added in incremental manners. The different silicate-water mixes showed minimal differences in macro elastic properties when water inclusions were added. As mentioned in Johansen & Ruud [1], when the nonporous silt inclusions were added to water-filled quartz with clay medium, in order to maintain porosity, the water filled quartz with clay need to increase when silt grains are added. Hence, for initial water-filled quartz with clay medium, the shear velocities decreases rapidly as nonporous silt grains fill the pores, hence the shear velocity of the effective medium increases drastically. This might indicate that the shear strength of a mineral is important for remaining a solid when waters fill the pores of the mineral.

Although the DEM model by Kuster & Toksöz [16] is limited to isotropic, linear and elastic media and dilute concentrations of inclusions, it can be used to get some knowledge about how the mechanical properties vary with added water inclusions. The DEM model used, by prof. Tor Arne Johansen (UiB), show an error for highly water filled materials, where some (randomly distributed) shear velocities are mapped close to 100 % porosity. This makes the model uncertain when investigating the mechanical properties of highly water saturated materials. It has been suggested by senior engineer Bent Ole Ruud and prof. Tor Arne Johansen himself, that the line 'DATA TOL/1.D+6/' (ref line 84 in appendix A.2) should be changed to 'DATA TOL/1.D+5/', to reduce the impact of the DEM model's "hard coded" stop criterion.

In chapters 5.3 and 5.4, the OASES-OASP models show prominent Scholte waves when calculating the amplitudes close to the water-sediment 1 interface. Even though the OASES-OASP is limited to horizontally stratified environments, the model seem to be robust for 2-D seismic modeling of Scholte waves. OASES also allow for 3-D modeling, which could be interesting to perform in an Arctic environmental model. When we defined the environmental

model, we used the absorption constant of 0.1 dB/λ in all layers, except for the air halfspace. Compared to the 'real world' we should expect viscoelastic attenuation in materials, hence some attenuation is expected. But, as Jensen et. al. [18] states, it can be hard to determine the absorption coefficients. Hence setting the constants to zero might be a good thin to do, and for instance, you avoid complex phase velocities, i.e. no complex wavenumbers neither. It might be that the absorption coefficients can contribute to aliasing effects, where complex wavenumbers are mapped as negative wavenumbers.

The frequency-phase velocity spectrum in figure 6.6 show two band-separated events, i.e. Scholte waves in the lower frequency range 2 Hz to 9 Hz and flexural waves in the higher frequency range 20 Hz to above 25 Hz. It would have been interesting to apply a narrow-band bandpass filter on that shot gather, to analyze the shot gather for each individual frequency band. Hence, one could maybe see the Scholte wave more distinctly in the shot gather, which is very disturbed by the flexural waves in figure 6.5.

The measurement results presented in chapter 6 show prominent aliasing effects, which according to Foti [46], is highly related to the total length of the seismic line. To minimize spatial aliasing effects, Foti et.al. [46] suggest to apply zero padding in space domain when several modes are present. We did not apply a frequency-wavenumber-filter on out data, which could have been done to for example filter away the negative wavenumbers. The main reason we did not apply the frequnecy-wavenumber filter, was that the respective filter method used in CWP/SU was hard to understand, and gave little meaning on how to apply. Nevertheless, in the $(x-t)$ domain for our experimental results, show prominent Scholte waves with group velocities less than 40 m/s, which is in correspondence with result given in Johansen & Ruud [1].

Chapter 8

Conclusion

The differential effective medium models show that for common porous rocks found in the study area (such as clay, quartz and silt), relatively high v_p/v_s- ratio are present when water filling the pores.

We have successfully managed to model and observe dispersive Scholte waves at (or close to) the water-sediment interfaces. We experienced aliasing effects in the measured data sets, which could make it hard to determine the group- and phase velocities from the measured amplitudes. Three component geophone ocean-bottom nodes at the seabed are generally sensitive to recording Scholte waves. Seismic experiments on floating sea ice in shallow water using airguns submerged to 4 meters water depths show prominent Scholte wave data measured at the seabed, and prominent ice flexural waves measured on top of the sea ice. The added ice layer in the environmental model, resulted in an interesting case of band-separated Scholte waves and flexural waves calculated on top of the sea ice, worth for future investigations.

8.1 Further work

Here are some suggestions to further work

- Look into the effect of roughness on seabed using OASES-OASP.
- Figure out how to 'extract' the radial wavenumbers from OASES-OASP, to be able to plot the radial wavenumber response before processing. This could maybe yield additional information for explaining why we get negative wavenumbers.
- 3-D modeling of the response to environmental model given in table 5.1, using for example OASES-OASP3D.
- Decrease receiver intervals and increase the total length of the seismic line to counter spatial aliasing effects, in combination with wavenumber-filtering the data sets.

- Process and analyze the shots close to land, and on land, to see if a Scholte-wave to Rayleigh-wave conversion is observed in the Svea 2018 seismic dataset. A narrow receiver interval is recommended for better resolution in this case.
- Make an inversion based on the measured phase velocities for the 3C geophones data on top of sea ice.

References

[1] T. A. Johansen and B. O. Ruud, "Characterization of seabed properties from scholte waves acquired on floating ice on shallow water," *Near Surface Geophysics*, vol. 18, no. Quantitative Geophysical Characterisation of Marine Near-Surface, pp. 49–59, 2020.

[2] M. D. Esteban, J. J. Diez, J. S. López, and V. Negro, "Why offshore wind energy?," *Renewable Energy*, vol. 36, no. 2, pp. 444–450, 2011.

[3] E. Muyzert, "Scholte wave velocity inversion for a near surface s-velocity model and ps-statics," in *SEG Technical Program Expanded Abstracts 2000*, pp. 1197–1200, Society of Exploration Geophysicists, 2000.

[4] T. A. Johansen, B. O. Ruud, and G. Hope, "Seismic on floating ice on shallow water: Observations and modeling of guided wave modes," *Geophysics*, vol. 84, no. 2, pp. P1–P13, 2019.

[5] T. A. Johansen, B. O. Ruud, R. Tømmerbakke, and K. Jensen, "Seismic on floating ice: data acquisition versus flexural wave noise," *Geophysical Prospecting*, vol. 67, no. 3, pp. 532–549, 2019.

[6] T. Bohlen, S. Kugler, G. Klein, and F. Theilen, "1.5 d inversion of lateral variation of scholte-wave dispersion," *Geophysics*, vol. 69, no. 2, pp. 330–344, 2004.

[7] S. Kugler, T. Bohlen, S. Bussat, and G. Klein, "Variability of scholte-wave dispersion in shallow-water marine sediments," *Journal of Environmental and Engineering Geophysics*, vol. 10, no. 2, pp. 203–218, 2005.

[8] S. Kugler, T. Bohlen, T. Forbriger, S. Bussat, and G. Klein, "Scholte-wave tomography for shallow-water marine sediments," *Geophysical Journal International*, vol. 168, no. 2, pp. 551–570, 2007.

[9] C. B. Park, R. D. Miller, J. Xia, J. Ivanov, G. V. Sonnichsen, J. A. Hunter, R. Good, R. Burns, and H. Christian, "Underwater masw to evaluate stiffness of water-bottom sediments," *The Leading Edge*, vol. 24, no. 7, pp. 724–728, 2005.

[10] D. Boiero, E. Wiarda, and P. Vermeer, "Surface-and guided-wave inversion for near-surface modeling in land and shallow marine seismic data," *The Leading Edge*, vol. 32, no. 6, pp. 638–646, 2013.

[11] H. M. Stemland, T. A. Johansen, B. O. Ruud, and A. S. Aniceto, "Measured sound levels in ice-covered shallow water caused by seismic shooting on top of and below floating ice, reviewed for possible impacts on true seals," *First Break*, vol. 37, no. 1, pp. 35–42, 2019.

[12] P. C. Vinh, "Scholte-wave velocity formulae," *Wave Motion*, vol. 50, no. 2, pp. 180–190, 2013.

[13] H. Schmidt and F. B. Jensen, "A full wave solution for propagation in multilayered viscoelastic media with application to gaussian beam reflection at fluid–solid interfaces," *The Journal of the Acoustical Society of America*, vol. 77, no. 3, pp. 813–825, 1985.

[14] H. Schmidt and G. Tango, "Efficient global matrix approach to the computation of synthetic seismograms," *Geophysical Journal International*, vol. 84, no. 2, pp. 331–359, 1986.

[15] H. Schmidt, *OASES Version 3.1 User Guide and Reference Manual*. Department of Ocean Engineering, Massachusetts Institute of Technology, October 2004.

[16] G. T. Kuster and M. N. Toksöz, "Velocity and attenuation of seismic waves in two-phase media: Part i. theoretical formulations," *Geophysics*, vol. 39, no. 5, pp. 587–606, 1974.

[17] E. H. Jensen, L.-J. Gelius, T. A. Johansen, and Z. Wang, "Consistent joint elastic-electrical differential effective-medium modelling of compacting reservoir sandstones," *Geophysical Prospecting*, vol. 61, no. 4, pp. 788–802, 2013.

[18] F. B. Jensen, W. A. Kuperman, M. B. Porter, and H. Schmidt, *Computational ocean acoustics*. Modern Acoustics and Signal Processing, Springer Science & Business Media, 2nd ed., 2011.

[19] H. Stemland, "Seismic acquisition in a shallow marine sea ice covered environment: The significance of survey geometry and possible impacts on pinnipeds," Master's thesis, Department of Earth Science - University of Bergen, May 2017.

[20] T. A. Johansen, "Report: Fieldwork 2018 «arctic seismic data laboratory» - ris-id 10188, granted permission for field work, ref: 16/01643-12, given 16.02.2018," report to sysselmannen, University of Bergen & The University Centre in Svalbard, October 2018.

[21] K. Jensen, "Modeling and processing of flexural wave noise in sea ice," Master's thesis, Department of Earth Science - University of Bergen, April 2016.

[22] S. L. Furland, "Effects of frozen and partly frozen surfaces on seismic data," masters thesis, Department of Earth Science - University of Bergen, February 2018.

[23] J. K. Cohen and J. J. W. Stockwell, *CWP/SU: Seismic Un*x Release No. 44: an open source software package for seismic research and processing.* Center for Wave Phenomena, Colorado School of Mines, 2015.

[24] L. E. Kinsler, A. R. Frey, A. B. Coppens, and J. V. Sanders, *Fundamentals of acoustics.* John Wiley & Sons, Inc., 4th. ed., 2000. ISBN 978-0-471-84789-2.

[25] J. D. Achenbach, *Wave propagation in elastic solids.* Amsterdam, The Netherlands: North-Holland Publishing Company, 1973.

[26] K. D. Lohne, P. Lunde, and M. Vestrheim, "Ultrasonic signal transmission in plates – study of a steel plate immersed in water," in *Proceedings of the 31st Scandinavian Symposium on Physical Acoustics*, Norwegian Physical Society, Norway, 01 2008.

[27] P. Lunde, "PHYS374 Teoretisk akustikk, Kapittel 5: Elastiske bølger i faste stoff." Lecture notes, September 2016.

[28] J. G. Scholte, "The Range of Existence of Rayleigh and Stoneley Waves," *Geophysical Supplements to the Monthly Notices of the Royal Astronomical Society*, vol. 5, pp. 120–126, 05 1947.

[29] P. C. Vinh and P. T. H. Giang, "On formulas for the velocity of stoneley waves propagating along the loosely bonded interface of two elastic half-spaces," *Wave Motion*, vol. 48, no. 7, pp. 647–657, 2011.

[30] P. C. Vinh and P. T. H. Giang, "Uniqueness of stoneley waves in pre-stressed incompressible elastic media," *International Journal of Non-Linear Mechanics*, vol. 47, no. 2, pp. 128–134, 2012.

[31] P. C. Vinh, P. G. Malischewsky, and P. T. H. Giang, "Formulas for the speed and slowness of stoneley waves in bonded isotropic elastic half-spaces with the same bulk wave velocities," *International Journal of Engineering Science*, vol. 60, pp. 53–58, 2012.

[32] P. Lunde, "PHYS371 Selected Topics in Underwater Acoustics, Chapter 2: Underwater acoustic wave propagation." Lecture notes, September 2019.

[33] J. Pujol, *Elastic Wave Propagation and Generation in Seismology.* Cambridge: Cambridge University Press, 2003.

[34] J. Miklowitz, *The theory of elastic waves and waveguides*, vol. 22 of *North-Holland series in applied mathematics and mechanics.* Amsterdam: North-Holland Publishing Company, 1978.

[35] D. G. Harkrider, "Surface waves in multilayered elastic media i. rayleigh and love waves from buried sources in a multilayered elastic half-space," *Bulletin of the Seismological Society of America*, vol. 54, no. 2, pp. 627–679, 1964.

[36] B. A. Auld, *Acoustic fields and waves in solids*, vol. 2. R. E. Krieger Publishing Company, Inc., 2nd ed., 1990.

[37] X. Lurton, *An Introduction to Underwater Acoustics. Principles and Applications*. Springer and Praxis Publishing, 2nd ed., 2010.

[38] R. A. Adams and C. Essex, *Calculus: a complete course*. Pearson, 8th ed., 2013. Toronto, ISBN 9780134154367.

[39] J. Zhu, J. S. Popovics, and F. Schubert, "Leaky rayleigh and scholte waves at the fluid–solid interface subjected to transient point loading," *The Journal of the Acoustical Society of America*, vol. 116, no. 4, pp. pp. 2101–2110, 2004.

[40] S. Foti, C. G. Lai, G. J. Rix, and C. Strobbia, *Surface wave methods for near-surface site characterization*. CRC press, 2015.

[41] W. M. Ewing, W. S. Jardetzky, and F. Press, *Elastic waves in layered media*. New York: McGraw-Hill, 1957.

[42] Wolfram Alpha LLC, "Wolfram|alpha," 2020. Champaign, IL, Available from: https://www.wolframalpha.com/input/?i=%281030%2F1217%29*%28x%2F44%29%5E2*%5Csqrt%281-%28x%2F1600%29%5E2%29%2B%282-%28x%2F44%29%5E2%29%5E2*%5Csqrt%281-%28x%2F1600%29%5E2%29-4*%5Csqrt%281-%28x%2F44%29%5E2%29* %5Csqrt%281-%28x%2F1600%29%5E2%29*%5Csqrt%281-%28x%2F1500%29%5E2%29 %3D0 (Accessed: December 10, 2020).

[43] C. B. Park, R. D. Miller, and J. Xia, "Imaging dispersion curves of surface waves on multi-channel record," in *SEG Technical Program Expanded Abstracts 1998*, pp. 1377–1380, Society of Exploration Geophysicists, 1998.

[44] C. Liner, *CWP/SU: SUPHASEVEL - Multi-mode PHASE VELocity dispersion map computed from shot record(s)*. Center for Wave Phenomena, Colorado School of Mines, 1.5 ed., 2008. Available from: https://github.com/JohnWStockwellJr/SeisUnix/blob/master/src/su/main/transforms/suphasevel.c (Accessed December 19, 2020).

[45] Ö. Yilmaz, *Seismic data analysis: Processing, inversion, and interpretation of seismic data*, vol. 1. Society of exploration geophysicists, 2001.

[46] S. Foti, L. Sambuelli, L. V. Socco, and C. Strobbia, "Spatial sampling issues in fk analysis of surface waves," in *15th EEGS Symposium on the Application of Geophysics to Engineering and Environmental Problems*, pp. 1–11, European Association of Geoscientists & Engineers, 2002.

[47] G. Mavko, T. Mukerji, and J. Dvorkin, *The rock physics handbook : tools for seismic analysis of porous media*. Cambridge: Cambridge University Press, 2nd ed., 2009.

[48] T. A. Johansen, *Relations between seismic parameters and rock parameters.* PhD thesis, Institute of Solid Earth Physics - University of Bergen, 1990.

[49] Norwegian Polar Institute, "Map of bedrock geology svalbard." Internet, n.d. Available from: https://www.npolar.no/tema/geologi-svalbard (Accessed: October 20, 2020).

[50] M. Hald, T. Dahlgren, T.-E. Olsen, and E. Lebesbye, "Late holocene palaeoceanography in van mijenfjorden, svalbard," *Polar Research*, vol. 20, no. 1, pp. 23–35, 2001.

[51] R. J. Steel and D. Worsley, "Svalbard's post-caledonian strata - an atlas of sedimentational patterns and palaeogeographic evolution," in *Petroleum geology of the northern European margin* (A. M. Spencer et.al., ed.), pp. 109–135, Norwegian Petroleum Society, London: Graham & Trotman, 1984.

[52] G. Simmons, *Single crystal elastic constants and calculated aggregate properties*, 34 ed., 1965.

[53] W. P. Mason, "Quartz crystal applications," *The Bell System Technical Journal*, vol. 22, no. 2, pp. 178–223, 1943.

[54] I. Koga, M. Aruga, and Y. Yoshinaka, "Theory of plane elastic waves in a piezoelectric crystalline medium and determination of elastic and piezoelectric constants of quartz," *Physical Review*, vol. 109, no. 5, p. 1467, 1958.

[55] D.-h. Han, *Effects of porosity and clay content on acoustic properties of sandstones and unconsolidated sediments.* PhD thesis, Stanford University, 1986.

[56] ISO, "Geotechnical investigation and testing–identification and classification of soil–part 1: Identification and description," Standard ISO 14688-1:2017, International Organization for Standardization, Brussels, Belgium, 2017. Available from: https://www.iso.org/standard/66345.html (Accessed: August 4, 2020).

[57] T. A. Johansen, "Rock physics," in *Petroleum Geophysics - Geoclass*, Oslo: UniGEO AS, 2010. ISBN 978-82-93099-00-0.

[58] J. G. Berryman, "Confirmation of biot's theory," *Applied Physics Letters*, vol. 37, no. 4, pp. 382–384, 1980.

[59] J. G. Berryman, "Long-wavelength propagation in composite elastic media ii. ellipsoidal inclusions," *The Journal of the Acoustical Society of America*, vol. 68, no. 6, pp. 1820–1831, 1980.

[60] B. E. Hornby, L. M. Schwartz, and J. A. Hudson, "Anisotropic effective-medium modeling of the elastic properties of shales," *Geophysics*, vol. 59, no. 10, pp. 1570–1583, 1994.

[61] J. G. Berryman, "Single-scattering approximations for coefficients in biot's equations of poroelasticity," *Journal of the Acoustical Society of America*, vol. 91, pp. 551–571, 1992.

[62] P. Avseth, T. Mukerji, and G. Mavko, "Quantitative seismic interpretation: Applying rock physics tools to reduce interpretation risk," *Cambridge University Press*, 2005.

[63] G. E. Parkes and L. Hatton, *The marine seismic source*, vol. 4. Springer Science & Business Media, 2013.

[64] K. Barry, D. Cavers, and C. Kneale, "Recommended standards for digital tape formats," *Geophysics*, vol. 40, no. 2, pp. 344–352, 1975.

[65] R. Hagelund and S. A. Levin, "Seg-y_r2. 0: Seg-y revision 2.0 data exchange format," 2017.

[66] L. J. Gelius, "Seismic signal theory and processing," in *Petroleum Geophysics - Geoclass*, Oslo: UniGEO AS, 2010. ISBN 978-82-93099-00-0.

[67] J. F. Claerbout, *Imaging the Earth's Interior*. Oxford: Blackwell Scientific Publications, 1985.

[68] J. W. Stockwell, *A Course in Geophysical Image Processing with Seismic Unix: GPGN 461/561 Lab*. Center for Wave Phenomena, 2012. Available from: https://yangpl.files.wordpress.com/2015/09/stockwell_su_tutorial_ch1-14.pdf (Accessed: December 18, 2020).

[69] T. A. Johansen, "Quantitative seismic interpretation (new)," in *Petroleum Geophysics - Geoclass*, Oslo: UniGEO AS, 2010. ISBN 978-82-93099-00-0.

[70] J. J. W. Stockwell, *CWP/SU: SUSPECFK - F-K Fourier SPECtrum of data set*. Center for Wave Phenomena, Colorado School of Mines, 1.21 ed., 2011. Available from: https://github.com/JohnWStockwellJr/SeisUnix/blob/master/src/su/main/transforms/suspecfk.c (Accessed December 19, 2020).

[71] H. Schmidt, *SAFARI: Seismo-acoustic fast field algorithm for range in-dependent environments. User's guide*. SACLANT Undersea Research Centre, sr-113 ed., 1988. La Sezia, Italy (unpublished).

[72] A. T. de Hoop and J. H. Van der Hijden, "Generation of acoustic waves by an impulsive point source in a fluid/solid configuration with a plane boundary," *The Journal of the Acoustical Society of America*, vol. 75, no. 6, pp. 1709–1715, 1984.

[73] A. T. de Hoop and J. H. M. T. Van der Hijden, "Generation of acoustic waves by an impulsive line source in a fluid/solid configuration with a plane boundary," *The Journal of the Acoustical Society of America*, vol. 74, no. 1, pp. 333–342, 1983.

[74] G. Hope and H. Schmidt, "A parallelization of the wavenumber integration acoustic modelling package oases," *Computational Geosciences*, vol. 23, no. 4, pp. 777–792, 2019.

[75] W. J. Ludwig, J. E. Nafe, and C. L. Drake, "Seismic refraction," in *The Sea* (A. E. Maxwell, ed.), vol. 4, pp. 53–84, Wiley, 1970.

[76] R. B. Herrmann, "Computer programs in seismology: An evolving tool for instruction and research," *Seismological Research Letters*, vol. 84, no. 6, pp. 1081–1088, 2013.

[77] H. Kolsky, *Stress waves in solids*, vol. 1098. Courier Corporation, 1963.

[78] R. Bracewell, *The Fourier transform and its applications*. McGraw-Hill electrical and electronic engineering series, New York: McGraw-Hill Book Company, 1965.

[79] H. Lamb, "On the flexure of an elastic plate," *Proceedings of the London Mathematical Society*, vol. s1-21, no. 1, pp. 70–91, 1889.

[80] H. Lamb, "On waves in an elastic plate," *Proceedings of the Royal Society A: Mathematical, Physical and Engineering Sciences*, vol. 93, pp. 114–128, 1917.

[81] R. Trupp, J. Hastings, S. Cheadle, and R. Vesely, "Seismic in arctic environs: Meeting the challenge," *The Leading Edge*, vol. 28, no. 8, pp. 936–942, 2009.

Appendix A

DEM script by Tor Arne Johansen (UiB)

The DEM script by Tor Arne Johansen (UiB) use the Fortran 77 programming language. The main script is given in appendix A.1, and the calculations are given in appendix A.2.

A.1 run_dem.f

```
      implicit none
      integer ifase,nasp
      parameter (ifase=2, nasp=1)
      integer ishape(nasp),isuccess,ngrow,ic,nc
      real*8 bulk(ifase),shear(ifase),rho(ifase),visk(ifase),
     &        asp(nasp),con(nasp),por,wfreq,
     &        bulkeffr,bulkeffi,shearefr,shearefi,rhoeff,pg(50,nasp),
     &        vpdem,vsdem
      real bulk_host,shear_host,rho_host,
     &     bulk_incl,shear_incl,rho_incl,asp_rat,
     &     cpmin,cpmax,dcp,cp

c     read properties of host medium (start of DEM computation)
      read(*,*) bulk_host,shear_host,rho_host
c     read properties of inclusions
      read(*,*) bulk_incl,shear_incl,rho_incl
c     read aspect ratio of inclusions
      read(*,*) asp_rat
c     read volum concentrations of inclusions in percent: start, end, increment
      read(*,*) cpmin,cpmax,dcp

      asp(1)=asp_rat
      con(1)=1.0d0
      ishape(1)=1
      bulk(1)=bulk_host*1.d+9
      bulk(2)=bulk_incl*1.d+9
      shear(1)=shear_host*1.d+9
```

```
      shear(2)=shear_incl*1.d+9
      rho(1)=rho_host*1.d+3
      rho(2)=rho_incl*1.d+3
      visk(1)=0.d0
      visk(2)=0.d0
      pg(1,1)=1.d0
      pg(2,1)=1.d0
      wfreq=1.d0

      nc=nint((cpmax-cpmin)/dcp)+1
      do 10 ic=1,nc
           cp=cpmin+(ic-1)*dcp
           por=cp*0.01d0
           call kustext(nasp,ifase,por,bulk,shear,
     &                rho,visk,wfreq,asp,con,ishape,
     &                pg,bulkeffr,bulkeffi,shearefr,shearefi,
     &                rhoeff,isuccess,ngrow)
           write(9,*)cp,bulkeffr,shearefr,rhoeff,isuccess,ngrow
           vpdem=dsqrt((bulkeffr+(4.d0/3.d0)*shearefr)/rhoeff)
           vsdem=dsqrt(shearefr/rhoeff)
           write(*,'(f6.1,2f9.4,3f8.1)')cp,bulkeffr*1.d-9,shearefr*1.d-9,
     &                      rhoeff,vpdem,vsdem
   10   continue

        end
```

A.2 kustext.f

```
            SUBROUTINE KUSTEXT(IASP,IFASE,POR,BULKR,SHEARR,
     &          RHO,VISKP,WFREQ,ALPHA,C,IPOREGEO,
     &          D,BULKEFFR,BULKEFFI,SHEAREFR,SHEAREFI,
     &          RHOEFF,ISUCCESS,NGROW)
C
C
C AUTHOR: TOR ARNE JOHANSEN,
C INSTITUTE OF SOLID EARTH PHYSICS,
C SEISMOLOGICAL OBSERVATORY,
C ALLEGT. 41,
C N-5007 BERGEN, NORWAY.
C
C
C PROGRAM TO COMPUTE THE DYNAMIC ELASTIC MODULI AND AVERAGE DENSITY
C IN A MULTI-PHASE MEDIUM APPLYING THE THEORY OF KUSTER & TOKSOEZ (1974)
C EXTENDED TO INCORPORATE THE EFFECT OF PORE INTERACTION.
C
```

```
C
C REFERENCES:
C
C Berge et al. 1992. Velocity-Porosity Relationships in the Upper Oceanic
C Crust: Theoretical Considerations. J. Geoph. Res. 97, (B11), 15239-15254.
C
C Berryman, J.G. 1980. Long-wavelength propagation in composite elastic
C media. I. Spherical inclusions. J. Acoust. Soc. Am. 68, 1809-1819.
C
C Berryman, J.G. 1980. Long-wavelength propagation in composite elastic
C media. I. Ellipsoidal inclusions. J. Acoust. Soc. Am. 68, 1820-1831.
C
C Kuster, G.T and Toksoez, M.N. 1974. Velocity and attenuation of seismic
C waves in two-phase media: Part I. Geophys. 39, 587-606.
C
C Toksoez, M.N., Cheng, C.H. and Timur, A. 1976. Velocities of seismic
C waves in porous rocks. Geophys. 41, 621-645.
C
C Yamakawa, N. 1962. Scattering and attenuation of elastic waves.
C Geophys. Mag. 31, 63-103.
C
C Wu, T.T. 1966. The effect of inclusion shape on the elastic moduli of
C a two-phase material. Int. J. Solids Structures 2, 1-8.
C
C INPUT PARAMETERS:
C
C    IASP:    NUMBER OF ASPECT RATIOS.
C    IFASE:   NUMBER OF PHASES (INCLUDING MATRIX).
C    POR:     TOTAL POROSITY (FRACTIONAL VOLUME OF THE INCLUSION-MATERIALs).
C    BULK(IFASE): VECTOR CONTAINING THE BULK MODULI OF THE CONSTITUENTS.
C    SHEAR(IFASE):VECTOR CONTAINING THE SHEAR MODULI OF THE CONSTITUENTS.
C    RHO(IFASE):  VECTOR CONTAINING THE DENSITIES OF THE CONSTITUENTS.
C    VISKP(IFASE):VECTOR CONTAINING THE VISCOSITIES OF THE CONSTITUENTS.
C    WFREQ:         ANGULAR FREQUENCY OF SEISMIC WAVE.
C    ALPHA(IASP): VECTOR CONTAINING THE ASPECT RATIOS OF THE INCLUSIONS.
C    C(IASP): VECTOR CONTAINING THE FRACTION OF TOTAL POROSITY OCCUPIED
C          BY PORES OF EACH ASPECT RATIO.
C    IPOREGEO(IASP): VECTOR CONTAINING THE PORE GEOMETRIES:
C         1 -- OBLATE SPHEROID (ELLIPSOID)
C         2 -- PROLATE SPHEROID
C         3 -- PENNY SHAPED
C         4 -- NEEDLE
C         5 -- DISC
C    D(IFASE,IASP): MATRIX DENOTING THE PORE FLUID (MATERIAL) GEOMETRY.
C
C OUTPUT:
C
C    BULKEFFR: EFFECTIVE BULK MODULUS (REAL COMPONENT).
```

```
66 C    BULKEFFI: EFFECTIVE BULK MODULUS (COMPLEX COMPONENT).
67 C    SHEAREFR: EFFECTIVE SHEAR MODULUS (REAL COMPONENT).
68 C    SHEAREFI: EFFECTIVE SHEAR MODULUS (COMPLEX COMPONENT).
69 C    RHOEFF:   AVERAGE DENSITY.
70 C    ISUCCESS: FLAG TELLING IF SOLUTION WAS ESTIMATED ACCORDING
71 C                    TO CRITERIA = 1 (GOOD SOLUTION) = 2 (BAD SOLUTION)
72 C    NGROW:    NUMBER OF INCLUSION EMBEDDINGS
73 C
74 C DECLARATIONS.
75 C
76       IMPLICIT REAL*8 (A-H,O-Z)
77       DIMENSION BULKR(50),SHEARR(50),RHO(50),ALPHA(50),C(50),
78      &  D(50,50),CD(50,50),SG(50),VISKP(50),IPOREGEO(50),E(4)
79       COMPLEX*16 BULK(50),SHEAR(50),
80      &  A,B,A1,A3,B1,B2,B3,C1,C2,C3,F1,F2,F3,F4,F5,F6,F7,F8,F9,
81      &  XM,YM,FM,FI,SUMB1,SUMB2,SUMS1,SUMS2,PMI,QMI,BULKM,SHEARM,UM,
82      &  BULKEFF,SHEAREFF,BULKPREV,SHEARPREV
83       INTEGER IFASE,IASP
84       DATA TOL/1.D+6/
85       LOGICAl ITERATE
86       ITERATE=.TRUE.
87       PI=4.D0*DATAN(1.D0)
88       PRSTY=POR
89       MAXGROW=10000
90 C
91 C PHASE 1 IS ASSOCIATED TO THE MATRIX MATERIAL.
92 C
93 C CONVERT ELASTIC MODULI TO COMPLEX REPRESENTATION.
94 C
95       DO I=1,IFASE
96          BULK(I)=DCMPLX(BULKR(I),0.D0)
97          SHEAR(I)=DCMPLX(SHEARR(I),0.D0)
98          IF (I .GT. 1) THEN
99             DO J=1,IASP
100               CD(I,J)=D(I-1,J)
101            END DO
102         ENDIF
103      END DO
104      IGROW=1
105      NGROW=0
106      NOIT=0
107 C
108 C ITERATE FOR SOLUTION.
109 C
110      DO WHILE (ITERATE .EQV. .TRUE.)
111         BULKEFF=BULK(1)
112         SHEAREFF=SHEAR(1)
113         RHOEFF=RHO(1)
```

```
114           VISKEFF=VISKP(1)
115           NOIT=NOIT+1
116 C
117 C DETERMINE THE NUMBER OF INCLUSION EMBEDDING.
118 C
119           IF (NOIT .EQ. 1) THEN
120             M=IGROW
121           ELSE
122             M=2*NOIT
123           ENDIF
124 C
125 C GROW POROSITY GRADUALLY.
126 C
127           DO K=1,M
128             BULKM=BULKEFF
129             SHEARM=SHEAREFF
130             RHOM=RHOEFF
131             VISKM=VISKEFF
132             POR=PRSTY/(FLOAT(M)-FLOAT(K-1)*PRSTY)
133             SUMB2=0.D0
134             SUMS2=0.D0
135             UM=4.D0*SHEARM/3.D0
136             XM=BULKM+UM
137             FM=SHEARM*(9.D0*BULKM+8.D0*SHEARM)
138      &                /(6.D0*(BULKM+2.D0*SHEARM))
139             YM=SHEARM+FM
140             RHOEFF=(1.D0-POR)*RHOM
141 C
142 C COMPUTE EFFECT OF EACH DISTINCT INCLUSION MATERIAL.
143 C
144             DO I=2,IFASE
145               SUMB1=0.D0
146               SUMS1=0.D0
147               SG(I)=0.D0
148 C
149 C COMPUTE EFFECT OF EACH PORE SHAPE.
150 C
151                 DO J=1,IASP
152 C
153 C COMPUTE PMI AND QMI FOR THE VARIOUS PORE GEOMETRIES.
154 C (SEE BERRYMAN(1980)) TABLE I.
155 C
156 C
157 C SPHERICAL INCLUSIONS.
158 C
159                   IF (ALPHA(J) .EQ. 1) THEN
160                     A1=BULKM+(4.D0/3.D0)*SHEARM
161                     B1=BULK(I)+(4.D0/3.D0)*SHEARM
```

```
                  PMI=3.D0*A1/B1
                  QMI=5.D0*(SHEARM+FM)/(SHEAR(I)+FM)
                ELSE
C
C SPHEROIDS.
C
                IF (IPOREGEO(J) .EQ. 1 .OR. IPOREGEO(J) .EQ. 2) THEN
                  ALPHA2=ALPHA(J)*ALPHA(J)
                  ALPHINV=1.D0/ALPHA(J)
C
C ELLIPSOIDAL (OBLATE SPHEROIDS).
C
                  IF (IPOREGEO(J) .EQ. 1) THEN
                    PHI=(ALPHA(J)/(1.D0-ALPHA2)**1.5D0)
     &                  *(DACOS(ALPHA(J))-ALPHA(J)*DSQRT(1.D0-ALPHA2))
                    G=ALPHA2*(3.D0*PHI-2.D0)/(1.D0-ALPHA2)
C
C PROLATE SPHEROIDS.
C (ARCCOS EXPRESSED BY 4.6.21 PAGE 87 IN ABROMOWITZ AND STEGUN (1970).
C
                  ELSEIF (IPOREGEO(J) .EQ. 2) THEN
                    PHI=ALPHA2/((1.D0-ALPHA2)**1.5D0)
     &                  *(ALPHINV*DSQRT(ALPHINV*ALPHINV-1.D0)
     &                  -DLOG(ALPHINV+DSQRT(ALPHINV**2-1.D0)))
                    G=(2.D0-3.D0*PHI)/(1.D0-ALPHA2)
                  ENDIF
C
C COMPUTE GENERAL EXPRESSIONS FOR SPHEROIDS.
C
C VISCID MATRIX.
C
                  IF (SHEARM .NE. 0.D0 .OR. VISKM .NE. 0.D0) THEN
                    IF (SHEARM .EQ. (0.D0,0.D0)) THEN
                      SHEARM=CMPLX(0.D0,-WFREQ*VISKM)
                    ENDIF
                    A=SHEAR(I)/SHEARM-1.D0
                    B=(BULK(I)/BULKM-SHEAR(I)/SHEARM)/3.D0
                    R=3.D0*SHEARM/(3.D0*BULKM+4.D0*SHEARM)
                    F1=1.D0+A*(1.5D0*(G+PHI)
     &                  -R*(1.5D0*G+2.5D0*PHI-4.D0/3.D0))
                    F2=1.D0+A*(1.D0+1.5D0*(G+PHI)
     &                  -0.5D0*R*(3.D0*G+5.D0*PHI))
     &                  +B*(3.D0-4.D0*R)+0.5D0*A*(A+3.D0*B)
     &                  *(3.D0-4.D0*R)*(G+PHI-R*(G-PHI+2.D0*PHI*PHI))
                    F3=1.D0+0.5D0*A*(R*(2.D0-PHI)
     &                  +((1.D0+ALPHA2)/ALPHA2)*G*(R-1.D0))
                    F4=1.D0+0.25D0*A*(3.D0*PHI+G-R*(G-PHI))
                    F5=A*(R*(G+PHI-4.D0/3.D0)-G)+B*PHI*(3.D0-4.D0*R)
```

```
                        F6=1.0+A*(1.D0+G-R*(G+PHI))
     &                     +B*(1.D0-PHI)*(3.D0-4.D0*R)
                        F7=2.D0+0.25D0*A*(9.D0*PHI+3.D0*G-R
     &                     *(5.D0*PHI+3.D0*G))+B*PHI*(3.D0-4.D0*R)
                        F8=A*(1.D0-2.D0*R+0.5D0*G*(R-1.D0)
     &                     +0.5D0*PHI*(5.D0*R-3.D0))
     &                     +B*(1.D0-PHI)*(3.D0-4.D0*R)
                        F9=A*(G*(R-1.D0)-R*PHI)+B*PHI*(3.D0-4.D0*R)
                        PMI=3.D0*F1/F2
                        QMI=2.D0/F3+1.D0/F4+(F4*F5+F6*F7-F8*F9)/(F2*F4)
C
C INVISCID MATRIX.
C
                      ELSE
                        PMI=0.D0
                        QMI=0.D0
                      ENDIF
C
C PENNY SHAPED INCLUSIONS.
C
                      ELSEIF (IPOREGEO(J) .EQ. 3) THEN
                        BETAM=SHEARM*(3.D0*BULKM+SHEARM)/
     &                        (3.D0*BULKM+4.D0*SHEARM)
                        A1=BULKM+(4.D0/3.D0)*SHEAR(I)
                        B1=BULK(I)+(4.D0/3.D0)*SHEAR(I)+PI*ALPHA(J)*BETAM
                        PMI=A1/B1
                        B2=4.D0*SHEAR(I)+PI*ALPHA(J)*(SHEARM+2.D0*BETAM)
                        C2=8.D0*SHEARM/B2
                        A3=2.D0*(BULK(I)+(2.D0/3.D0)*SHEAR(I)
     &                        +(2.D0/3.D0)*SHEARM)
                        B3=BULK(I)+(4.D0/3.D0)*SHEAR(I)+PI*ALPHA(J)*BETAM
                        C3=A3/B3
                        QMI=(1.D0+C2+C3)/5.D0
C
C  NEEDLES.
C
                      ELSEIF (IPOREGEO(J) .EQ. 4) THEN
                        GMAM=SHEARM*((3.D0*BULKM+SHEARM)/
     &                        (3.D0*BULKM+7.D0*SHEARM))
                        A=BULKM+SHEARM+SHEAR(I)/3.D0
                        B=BULK(I)+SHEARM+SHEAR(I)/3.D0
                        PMI=A/B
                        C1=4.D0*SHEARM/(SHEARM+SHEAR(I))
                        C2=2.D0*(SHEARM+GMAM)/(SHEAR(I)+GMAM)
                        A3=BULK(I)+(4.D0/3.D0)*SHEARM
                        B3=BULK(I)+SHEARM+SHEAR(I)/3.D0
                        C3=A3/B3
                        QMI=(C1+C2+C3)/5.D0
```

```
C
C DISCS.
C
                    ELSEIF (IPOREGEO(J) .EQ. 5) THEN
                      FI=SHEAR(I)*(9.D0*BULK(I)+8.D0*SHEAR(I))/
     &                   (6.D0*(BULK(I)+2.D0*SHEAR(I)))
                      PMI=(BULKM+(4.D0/3.D0)*SHEAR(I))/
     &                    (BULK(I)+(4.D0/3.D0)*SHEAR(I))
                      IF (FI .NE. 0.D0) THEN
                        QMI=(SHEARM+FI)/(SHEAR(I)+FI)
                      ELSE
                        QMI=1.0D10
                      ENDIF
                    ENDIF
                  ENDIF
                  SIJ=C(J)*CD(I,J)
                  PMI=PMI/3.D0
                  QMI=QMI/5.D0
                  SUMB1=SUMB1+SIJ*PMI
                  SUMS1=SUMS1+SIJ*QMI
                  SG(I)=SG(I)+SIJ
                END DO
                RHOEFF=RHOEFF+POR*SG(I)*RHO(I)
                SUMB2=SUMB2+POR*(BULKM-BULK(I))*SUMB1
                SUMS2=SUMS2+POR*(SHEARM-SHEAR(I))*SUMS1
              END DO
              BULKEFF=(XM*BULKM-UM*SUMB2)/(XM+SUMB2)
              SHEAREFF=(YM*SHEARM-FM*SUMS2)/(YM+SUMS2)
            END DO
C
C CHECK FOR CONVERGENCE.
C
            NGROW=NGROW+1
            IF (NGROW .GT. 1) THEN
              E(1)=DABS(DREAL(BULKEFF)-DREAL(BULKPREV))
              E(2)=DABS(DIMAG(BULKEFF)-DIMAG(BULKPREV))
              E(3)=DABS(DREAL(SHEAREFF)-DREAL(SHEARPREV))
              E(4)=DABS(DIMAG(SHEAREFF)-DIMAG(SHEARPREV))
              DIFF=0.D0
              DO L=1,4
                DIFF=DIFF+E(L)
              END DO
C
C STOP ITERATION IF THE SOLUTIONS CONVERGE.
C
              IF (DIFF .LE. TOL) THEN
                ITERATE=.FALSE.
                ISUCCESS=1
```

```
306               ENDIF
307             ENDIF
308             BULKPREV=BULKEFF
309             SHEARPREV=SHEAREFF
310   C
311   C STOP ITERATION IF MAXIMUM NUMBER OF ITERATIONS IS EXCEEDED,
312   C AND FLAG SOLUTION.
313   C
314             IF (NGROW .GE. MAXGROW) THEN
315               ITERATE=.FALSE.
316               ISUCCESS=2
317             ENDIF
318           END DO
319           BULKEFFR=DREAL(BULKEFF)
320           BULKEFFI=DIMAG(BULKEFF)
321           SHEAREFR=DREAL(SHEAREFF)
322           SHEAREFI=DIMAG(SHEAREFF)
323   C
324   C AVOID NEGATIVE ELASTIC MODULI.
325   C
326           IF (BULKEFFR .LT. 0.D0) BULKEFFR=0.D0
327           IF (SHEAREFR .LT. 0.D0) SHEAREFR=0.D0
328           RETURN
329           END
```

Appendix B

Script to plot elastic properties from DEM model using MATLAB R2017b

Script to plot the elastic properties calculated from the DEM model using MATLAB R2017b, for the clay-water mix, e.g. see figure 3.4. This script could be used as an example for other solid-water mixes, e.g. by changing the input files. This script is specifically suited for Linux Ubuntu computers, and reads txt-files my own Home destination at UiB.

```
%================================================================================
%%      MATLAB R2017b script for plotting DEM results for CLAY - WATER mix
%================================================================================
% Script to read and plot .txt files from the results given by DEM
% (Differential Effective Method) model
%
% AUTHOR: ERIK LARSEN
% INSTITUTE OF PHYSICS AND TECHNOLOGY
% UNIVERSITY OG BERGEN
% August-November, 2020
%
%================================================================================
% ABOUT DEM MODEL:
%
% AUTHOR: TOR ARNE JOHANSEN,
% INSTITUTE OF SOLID EARTH PHYSICS,
% SEISMOLOGICAL OBSERVATORY,
% ALLEGT. 41,
% N-5007 BERGEN, NORWAY.
%
% PROGRAM TO COMPUTE THE DYNAMIC ELASTIC MODULI AND AVERAGE DENSITY
% IN A MULTI-PHASE MEDIUM APPLYING THE THEORY OF KUSTER & TOKSOEZ (1974)
% EXTENDED TO INCORPORATE THE EFFECT OF PORE INTERACTION.
%
%================================================================================
% PROCEDURE IN LINUX TERMINAL:
```

```
%
% Example of input-file to the DEM-software:
%
% 21.0     7.0      2.50    # Bulk (GPa), Shear (GPa), Rho(kg/liter) of host medium - clay*
%  2.318   0.0      1.030   # Bulk (GPa), Shear (GPa), Rho(kg/liter) of inclusion - water
%  0.02                     # Aspect ratio of inclusions
%  0.0    100.0   0.1       # First, last, increment for volume concentration (%) for inclusions
%# *Johansen & Ruud (2020), table 1
%#
%# END INPUTFILE
%
% with the following command in Linux Terminal:
%    ./run_dem < dem_clay_water_rat_0_02.inp > dem_clay_water_rat_0_02.txt
%
% The output-files are generated the same way, changing the name and content of the input files.
%
% The output files generated are then formatted to .txt-files, which are
% compatible with MATLAB. The output-file columns consist of the following
% contents:
%
% Col no. - Contents
%    1    - Concentration of inclusions/porosity (%)
%    2    - Bulk modulus (GPa)
%    3    - Shear modulus (GPa)
%    4    - Density (kg/m^3)
%    5    - P-velocity (m/s)
%    6    - S-velocity (m/s)
%================================================================================

clc
close all
clear all

%================================================================================
%%                        READ AND IMPORT DATA FROM .TXT FILES
%================================================================================

disp('Plotting elastic properties from the Differential Effective Medium (DEM) model computations')

formatSpec = '%6f%9f%9f%8f%8f%f%[^\n\r]';  % Specification of formats in txt-file to be read

% specify locations of file names to be read (.txt-file from DEM-results)
```

```
infilename_0_02 = '/Home/siv26/hih005/DEM/DEM_ERIK/clay_water/dem_clay_water_rat_0_02.txt';
infilename_0_03 = '/Home/siv26/hih005/DEM/DEM_ERIK/clay_water/dem_clay_water_rat_0_03.txt';
infilename_0_04 = '/Home/siv26/hih005/DEM/DEM_ERIK/clay_water/dem_clay_water_rat_0_04.txt';
infilename_0_05 = '/Home/siv26/hih005/DEM/DEM_ERIK/clay_water/dem_clay_water_rat_0_05.txt';
infilename_1_0 = '/Home/siv26/hih005/DEM/DEM_ERIK/clay_water/dem_clay_water_rat_1_0.txt';
% open and read the file names chosen
fileID_0_02 = fopen(infilename_0_02,'r');
fileID_0_03 = fopen(infilename_0_03,'r');
fileID_0_04 = fopen(infilename_0_04,'r');
fileID_0_05 = fopen(infilename_0_05,'r');
fileID_1_0 = fopen(infilename_1_0,'r');

% Read columns of data according to the format.
% This call is based on the structure of the file used to generate this
% code. If an error occurs for a different file, try regenerating the code
% from the Import Tool.
dataArray_0_02 = textscan(fileID_0_02, formatSpec, 'Delimiter', '', 'WhiteSpace', '', 'TextType', 'string', 'ReturnOnError', false);
dataArray_0_03 = textscan(fileID_0_03, formatSpec, 'Delimiter', '', 'WhiteSpace', '', 'TextType', 'string', 'ReturnOnError', false);
dataArray_0_04 = textscan(fileID_0_04, formatSpec, 'Delimiter', '', 'WhiteSpace', '', 'TextType', 'string', 'ReturnOnError', false);
dataArray_0_05 = textscan(fileID_0_05, formatSpec, 'Delimiter', '', 'WhiteSpace', '', 'TextType', 'string', 'ReturnOnError', false);
dataArray_1_0 = textscan(fileID_1_0, formatSpec, 'Delimiter', '', 'WhiteSpace', '', 'TextType', 'string', 'ReturnOnError', false);

% Close the text files.
fclose(fileID_0_02);
fclose(fileID_0_03);
fclose(fileID_0_04);
fclose(fileID_0_05);
fclose(fileID_1_0);

% Create output variables
dem_clay_water_rat_0_02 = table(dataArray_0_02{1:end-1}, 'VariableNames', {'VarName1','VarName2','VarName3','VarName4','VarName5','VarName6'});
dem_clay_water_rat_0_03 = table(dataArray_0_03{1:end-1}, 'VariableNames', {'VarName1','VarName2','VarName3','VarName4','VarName5','VarName6'});
dem_clay_water_rat_0_04 = table(dataArray_0_04{1:end-1}, 'VariableNames', {'VarName1','VarName2','VarName3','VarName4','VarName5','VarName6'});
dem_clay_water_rat_0_05 = table(dataArray_0_05{1:end-1}, 'VariableNames', {'VarName1','VarName2','VarName3','VarName4','VarName5','VarName6'});
```

```
dem_clay_water_rat_1_0 = table(dataArray_1_0{1:end-1}, 'VariableNames', {'VarName1','VarName2','VarName3','VarName4','VarName5','VarName6'});

% Clear temporary variables
clearvars infilename_0_02 formatSpec fileID_0_02 dataArray_0_02 ans
clearvars infilename_0_03 formatSpec fileID_0_03 dataArray_0_03 ans
clearvars infilename_0_04 formatSpec fileID_0_04 dataArray_0_04 ans
clearvars infilename_0_05 formatSpec fileID_0_05 dataArray_0_05 ans
clearvars infilename_1_0 formatSpec fileID_1_0 dataArray_1_0 ans

%%=========================================================================
%% PLOTTING OF RESULTS
%%=========================================================================

%%=========================================================================
% POROSITY
%%=========================================================================

% Ask for user specified inputs for host medium and inclusion
dlgtitle = 'Specify host medium and inclusion from DEM';
prompt = {'Host medium: ','Inclusion:'};
dims = [1 65];
defaultanswer= {'clay','water'};
answer = inputdlg(prompt,dlgtitle,dims,defaultanswer);

% NB: 'cell2str.m' is used to convert cell data from 'answer' (inputdlg) to
% string data (see  Per-Anders Ekstrom (2020). cell2str
% (https://www.mathworks.com/matlabcentral/fileexchange/13999-cell2str),
% MATLAB Central File Exchange. Retrieved September 22, 2020.)
host = cell2str(answer(1))     % get host name from answer using 'cell2str.m'
inclus = cell2str(answer(2))   % get inclusion name from answer using 'cell2str.m'

fig = figure(1);               % create figure window
set(fig, 'units','normalized','outerposition',[0 0 0.5 0.6]); % Enlarge figure

% Read porosity data located in first coloumn
data_por_0_02 = dem_clay_water_rat_0_02{:,1};
data_por_0_03 = dem_clay_water_rat_0_03{:,1};
data_por_0_04 = dem_clay_water_rat_0_04{:,1};
data_por_0_05 = dem_clay_water_rat_0_05{:,1};
data_por_1_0 = dem_clay_water_rat_1_0{:,1};

% Create legend listing the five water aspect ratios alpha_w
legends = {' 0.02',' 0.03',' 0.04',' 0.05',' 1.0'};

xlim_data = [0 100];    % limit x-axis from 0-100 on all plots (i.e. porosity: 0-100 %)
xdelim_data = ([0 10 20 30 40 50 60 70 80 90 100]);     % set delimiter x-axis
```

```
149 set(fig,'units','normalized');            % set constant window size
150 set(fig, 'Position', [0.5 0.5 0.5 0.5]); % set constant window size
151
152 %=========================================================================
153 %                                  BULK MODULUS
154 %=========================================================================
155 % Read bulk modulus data located in second coloumn
156 data_bulk_rat_0_02 = dem_clay_water_rat_0_02{:,2};
157 data_bulk_rat_0_03 = dem_clay_water_rat_0_03{:,2};
158 data_bulk_rat_0_04 = dem_clay_water_rat_0_04{:,2};
159 data_bulk_rat_0_05 = dem_clay_water_rat_0_05{:,2};
160 data_bulk_rat_1_0 = dem_clay_water_rat_1_0{:,2};
161
162 % Plot porosity vs. bulk modulus data for all five water aspect ratios in same subplot
163 subplot(3,2,1)
164 plot(data_por_0_02,data_bulk_rat_0_02); hold on; % Plot porosity vs. bulk modolus for
        alpha_w = 0.02
165 plot(data_por_0_03,data_bulk_rat_0_03); hold on; % Plot porosity vs. bulk modolus for
        alpha_w = 0.03
166 plot(data_por_0_04,data_bulk_rat_0_04); hold on; % Plot porosity vs. bulk modolus for
        alpha_w = 0.04
167 plot(data_por_0_05,data_bulk_rat_0_05); hold on; % Plot porosity vs. bulk modolus for
        alpha_w = 0.05
168 plot(data_por_1_0,data_bulk_rat_1_0); hold off;  % Plot porosity vs. bulk modolus for
        alpha_w = 1.0
169 grid on; xlabel('Porosity (%)'); ylabel('Bulk modulus (GPa)'); xlim(xlim_data); xticks
        (xdelim_data);
170
171 % Create  and place the '(a)' title heading
172 ta = title('(a)');
173 set(ta, 'horizontalAlignment', 'left');
174 set(ta, 'units', 'normalized');
175 ha = get(ta, 'position');
176 set(ta, 'position', [0 ha(2) ha(3)]);
177
178 % Define y-ticks for this specific plot
179 yticks(0:5:30)
180
181
182 %=========================================================================
183 %%                                  SHEAR MODULUS
184 %=========================================================================
185 % Read shear modulus data located in third coloumn
186 data_shear_rat_0_02 = dem_clay_water_rat_0_02{:,3};
187 data_shear_rat_0_03 = dem_clay_water_rat_0_03{:,3};
188 data_shear_rat_0_04 = dem_clay_water_rat_0_04{:,3};
189 data_shear_rat_0_05 = dem_clay_water_rat_0_05{:,3};
190 data_shear_rat_1_0 = dem_clay_water_rat_1_0{:,3};
```

```
191
192 % Plot porosity vs. shear modulus data for all five water aspect ratios in same
    subplot
193 subplot(3,2,3)
194 plot(data_por_0_02,data_shear_rat_0_02); hold on; % Plot porosity vs. shear modolus
    for alpha_w = 0.02
195 plot(data_por_0_03,data_shear_rat_0_03); hold on; % Plot porosity vs. shear modolus
    for alpha_w = 0.03
196 plot(data_por_0_04,data_shear_rat_0_04); hold on; % Plot porosity vs. shear modolus
    for alpha_w = 0.04
197 plot(data_por_0_05,data_shear_rat_0_05); hold on; % Plot porosity vs. shear modolus
    for alpha_w = 0.05
198 plot(data_por_1_0,data_shear_rat_1_0); hold off;  % Plot porosity vs. shear modolus
    for alpha_w = 1.0
199 grid on; xlabel('Porosity (%)'); ylabel('Shear modulus (GPa)'); xlim(xlim_data);
    xticks(xdelim_data);
200
201 % Create  and place the '(c)' title heading
202 tc = title('(c)');
203 set(tc, 'horizontalAlignment', 'left');
204 set(tc, 'units', 'normalized');
205 hc = get(tc, 'position');
206 set(tc, 'position', [0 hc(2) hc(3)]);
207
208 % Define y-ticks for this specific plot
209 yticks(0:1:8)
210
211 %================================================================================
212 %%                                    DENSITY
213 %================================================================================
214 % Read density data located in fourth coloumn
215 data_dens_rat_0_02 = dem_clay_water_rat_0_02{:,4};
216 data_dens_rat_0_03 = dem_clay_water_rat_0_03{:,4};
217 data_dens_rat_0_04 = dem_clay_water_rat_0_04{:,4};
218 data_dens_rat_0_05 = dem_clay_water_rat_0_05{:,4};
219 data_dens_rat_1_0 = dem_clay_water_rat_1_0{:,4};
220
221 % Plot porosity vs. density data for all five water aspect ratios in same subplot
222 subplot(3,2,5)
223 plot(data_por_0_02,data_dens_rat_0_02); hold on; % Plot porosity vs. density for
    alpha_w = 0.02
224 plot(data_por_0_03,data_dens_rat_0_03); hold on; % Plot porosity vs. density for
    alpha_w = 0.03
225 plot(data_por_0_04,data_dens_rat_0_04); hold on; % Plot porosity vs. density for
    alpha_w = 0.04
226 plot(data_por_0_05,data_dens_rat_0_05); hold on; % Plot porosity vs. density for
    alpha_w = 0.05
```

```
227 plot(data_por_1_0,data_dens_rat_1_0); hold off;  % Plot porosity vs. density for
        alpha_w = 1.0
228 grid on; xlabel('Porosity (%)'); ylabel('Density (kg/m^3)'); xlim(xlim_data); xticks(
        xdelim_data);
229
230 % Create and place the '(e)' title heading
231 te = title('(e)');
232 set(te, 'horizontalAlignment', 'left');
233 set(te, 'units', 'normalized');
234 he = get(te, 'position');
235 set(te, 'position', [0 he(2) he(3)]);
236
237 % Define y-ticks for this specific plot
238 yticks(1000:250:2500)
239
240 %=========================================================================================
241 %%                          COMPRESSIONAL VELOCITY (P-VELOCITY)
242 %=========================================================================================
243 % Read compressional velocity data located in fifth coloumn (P-vel data)
244 data_pvel_rat_0_02 = dem_clay_water_rat_0_02{:,5};
245 data_pvel_rat_0_03 = dem_clay_water_rat_0_03{:,5};
246 data_pvel_rat_0_04 = dem_clay_water_rat_0_04{:,5};
247 data_pvel_rat_0_05 = dem_clay_water_rat_0_05{:,5};
248 data_pvel_rat_1_0 = dem_clay_water_rat_1_0{:,5};
249
250 % Plot porosity vs. compressional velocity data for all five water aspect ratios in
        same subplot
251 subplot(3,2,2)
252 plot(data_por_0_02,data_pvel_rat_0_02); hold on; % Plot porosity vs. compressional
        velocity for alpha_w = 0.02
253 plot(data_por_0_03,data_pvel_rat_0_03); hold on; % Plot porosity vs. compressional
        velocity for alpha_w = 0.03
254 plot(data_por_0_04,data_pvel_rat_0_04); hold on; % Plot porosity vs. compressional
        velocity for alpha_w = 0.04
255 plot(data_por_0_05,data_pvel_rat_0_05); hold on; % Plot porosity vs. compressional
        velocity for alpha_w = 0.05
256 plot(data_por_1_0,data_pvel_rat_1_0); hold off;  % Plot porosity vs. compressional
        velocity for alpha_w = 1.0
257 grid on; xlabel('Porosity (%)'); ylabel('Compr. velocity (m/s)'); xlim(xlim_data);
        xticks(xdelim_data)
258
259 % Create and place the '(b)' title heading
260 tb = title('(b)');
261 set(tb, 'horizontalAlignment', 'left');
262 set(tb, 'units', 'normalized');
263 hb = get(tb, 'position');
264 set(tb, 'position', [0 hb(2) hb(3)]);
265
```

```
% Define y-ticks for this specific plot
yticks(1000:500:4000)

%=========================================================================================
%%                          SHEAR VELOCITY (S-VELOCITY)
%=========================================================================================
% Read shear velocity data located in sixth coloumn (S-vel data)
data_svel_rat_0_02 = dem_clay_water_rat_0_02{:,6};
data_svel_rat_0_03 = dem_clay_water_rat_0_03{:,6};
data_svel_rat_0_04 = dem_clay_water_rat_0_04{:,6};
data_svel_rat_0_05 = dem_clay_water_rat_0_05{:,6};
data_svel_rat_1_0 = dem_clay_water_rat_1_0{:,6};

% Account for an error in 'run_dem.f' for when por. -> 100 % then vs must ->
% 0, which causes the vs plot to be inconsistent for higher porosity values.
% If an index is zero, make the next index zero.
k1=[];l1=[];m1=[];n1=[];p1=[]; % create empty vectors
% Check and adjust the S-velocities for the alpha_w = 0.02 file
for k1=1:length(data_svel_rat_0_02)-1
    if all(data_svel_rat_0_02(k1)) == 0
        disp('For data_vpvs_rat_0_02:')
        data_svel_rat_0_02(k1+1)=0;
        disp('Accounting for that when por -> 100 % => vs -> 0')
    end
end
% Check and adjust the S-velocities for the alpha_w = 0.03 file
for l1=1:length(data_svel_rat_0_03)-1
    if all(data_svel_rat_0_03(l1)) == 0
        disp('For data_vpvs_rat_0_03:')
        data_svel_rat_0_03(l1+1)=0;
        disp('Accounting for that when por -> 100 % => vs -> 0')
    end
end
% Check and adjust the S-velocities for the alpha_w = 0.04 file
for m1=1:length(data_svel_rat_0_04)-1
    if all(data_svel_rat_0_04(m1)) == 0
        disp('For data_vpvs_rat_0_04:')
        data_svel_rat_0_04(m1+1)=0;
        disp('Accounting for that when por -> 100 % => vs -> 0')
    end
end
% Check and adjust the S-velocities for the alpha_w = 0.05 file
for n1=1:length(data_svel_rat_0_05)-1
    if all(data_svel_rat_0_05(n1)) == 0
        disp('For data_vpvs_rat_0_05:')
        data_svel_rat_0_05(n1+1)=0;
        disp('Accounting for that when por -> 100 % => vs -> 0')
    end
```

```
end
% Check and adjust the S-velocities for the alpha_w = 1.0 file
for p1=1:length(data_svel_rat_1_0)-1
    if all(data_svel_rat_1_0(p1)) == 0
        disp('For data_svel_rat_1_0:')
        data_svel_rat_1_0(p1+1) = 0;
        disp('Accounting for that when por -> 100 % => vs -> 0')
    end
end

% Plot porosity vs. shear velocity (modified) data for all five water aspect ratios in
    same subplot
subplot(3,2,4)
plot(data_por_0_02,data_svel_rat_0_02); hold on; % Plot porosity vs. compressional
    velocity for alpha_w = 0.02
plot(data_por_0_03,data_svel_rat_0_03); hold on; % Plot porosity vs. compressional
    velocity for alpha_w = 0.03
plot(data_por_0_04,data_svel_rat_0_04); hold on; % Plot porosity vs. compressional
    velocity for alpha_w = 0.04
plot(data_por_0_05,data_svel_rat_0_05); hold on; % Plot porosity vs. compressional
    velocity for alpha_w = 0.05
plot(data_por_1_0,data_svel_rat_1_0); hold off;  % Plot porosity vs. compressional
    velocity for alpha_w = 1.0
grid on; xlabel('Porosity (%)'); ylabel('Shear velocity (m/s)'); xlim(xlim_data);
    xticks(xdelim_data)

% Create and place the '(d)' title heading
td = title('(d)');
set(td, 'horizontalAlignment', 'left');
set(td, 'units', 'normalized');
hd = get(td, 'position');
set(td, 'position', [0 hd(2) hd(3)]);

% Define y-ticks for this specific plot
yticks(0:250:2000)

%=========================================================================================
%%              COMPRESSIONAL-/SHEAR VELOCITY-RATIO (Vp/Vs-RATIO)
%=========================================================================================
% Calculate Vp/Vs-ratios based on vp and vs data
data_vpvs_rat_0_02 = data_pvel_rat_0_02./data_svel_rat_0_02;
data_vpvs_rat_0_03 = data_pvel_rat_0_03./data_svel_rat_0_03;
data_vpvs_rat_0_04 = data_pvel_rat_0_04./data_svel_rat_0_04;
data_vpvs_rat_0_05 = data_pvel_rat_0_05./data_svel_rat_0_05;
data_vpvs_rat_1_0 = data_pvel_rat_1_0./data_svel_rat_1_0;

% Plot porosity vs. Vp/Vs-ratios (Vs modified) for all five water aspect ratios in
    same subplot
```

```
354 subplot(3,2,6)
355 plot(data_por_0_02,data_vpvs_rat_0_02); hold on; % Plot porosity vs. compressional
        velocity for alpha_w = 0.02
356 plot(data_por_0_03,data_vpvs_rat_0_03); hold on; % Plot porosity vs. compressional
        velocity for alpha_w = 0.03
357 plot(data_por_0_04,data_vpvs_rat_0_04); hold on; % Plot porosity vs. compressional
        velocity for alpha_w = 0.04
358 plot(data_por_0_05,data_vpvs_rat_0_05); hold on; % Plot porosity vs. compressional
        velocity for alpha_w = 0.05
359 plot(data_por_1_0,data_vpvs_rat_1_0); hold off;  % Plot porosity vs. compressional
        velocity for alpha_w = 1.0
360 grid on; xlabel('Porosity (%)'); ylabel('\nu_{\itp} / \nu_{\its}'); xlim(xlim_data);
        xticks(xdelim_data)
361 ylim([0 100]); % Limit the y-axis to 100
362
363 % Create and place the '(f)' title heading
364 tf = title('(f)');
365 set(tf, 'horizontalAlignment', 'left');
366 set(tf, 'units', 'normalized');
367 hf = get(tf, 'position');
368 set(tf, 'position', [0 hf(2) hf(3)]);
369
370 % Define y-ticks for this specific plot
371 yticks(0:20:100)
372
373 %=========================================================================
374 %%                                ADD LEGENDS
375 %=========================================================================
376 hL = legend(legends,'Box', 'off','Location','East')
377 % Programatically move the Legend
378 newPosition = [0.86 0.40 0.2 0.17];
379 newUnits = 'normalized';
380 set(hL,'Position', newPosition,'Units', newUnits);
381
382 %=========================================================================
383 %%                                END OF SCRIPT
384 %=========================================================================
```

Appendix C

Copies of technical documents following the Svea 2016 raw datasets

In appendix C.1 we find information about how the raw data SEG-Y files from the Svea 2018 seismic experiment are formatted, including some information about receiver intervals and depths. In appendix C.2 we find some information about the receiver instrumentation used in the Svea 2018 seismic experiment, e.g. sensitivity and uncertainties for the receivers.

C.1 Copy of 'README.txt' file

Svea 2018 SEG-Y files

SEG-Y trace header fields:
Byte 9-12: field record number (FFID)
Byte 13-16: Receiver position/number
Byte 17-18: Shot position/number
Byte 73-88: UTM coordinates (m), Zone 33X

All files are with 1 ms sampling interval and 8000 samples per trace.

The acquisition was carried out in several stages:

Table C.1: Information about the SEG-Y files raw datasets' channel specifications. FFID: Field File Identification Number (channel specifications), pos.: shot position number, trilobite: 4C ocean-bottom node, Hydrophone: hydrophones submerged in water, geo.strings: gimballed geophone strings, 3C-geophone: three component geophones placed on top of the sea ice.

FFID	Source	Pos.	Trilobit	Hydrophone	Geo.strings	3C-geophone
2394-2401	DC	94-101	1-41	1-60	1-180	1-90
2404-2423	DC	121-102	1-41	1-60	1-180	1-90
2430-2554	AG	101-120	1-41	1-60	1-180	1-90
2556-2575	DC	141-122	21-60	1-60	1-180	1-90
2576-2695	AG	121-140	21-60	1-60	1-180	1-90
2697-2717	DC	161-142	41-80	21-80	1-180	1-90
2727-2767	AG	141-146	41-80	21-80	1-180	-
2768-2803	DC	161-194	41-80	21-80	19-190	-
2804-2842	DC	140-103	41-80	21-80	19-190	-
2844-2945	AG2	147-164	41-80	21-80	19-190	-
2950-2967	AG2	182-183	41-80	21-80	19-190	-

Note that some parts of the line are shot with decreasing shot numbers.
Not all FFIDs are present in the files since records for bad shot have been removed.

Source type:
DC=detonating cord, two in parallel (2 m apart) 25 m length (2 kg explosives)
AG=air gun (Sercel Mini G, 12 cu.in., 2000 psi)
AG2=air gun (Bolt LLX 1900, 40 cu.in., 2000 psi)

Trilobits (4C OBN) and hydrophones (single, 5 m depth) are placed at node positions (25 m intervals).

Source position numbers: source N+100 lays between node N-1 and N.

Geophone strings have group length 12.5 m and the midpoints are shifted 6.25 m relative to the node positions. The receiver numbers can be converted to node numbers by dividing by 2. Node N lays between string 2N-1 and 2N. Each string consists of 8 vertical gimbal mounted geophones.

The 3C-geophones recorded only up to FFID 2717. There are 30 3C geophones deployed at 12.5 intervals, recording to 90 channels. The first 3C geophone is placed at node 41. Channel numbers increase with 3 for each 3C geophone. Components are identified with byte 29-30 in the traces header according to SEG standard (12=Z, 13=T, 14=R).

Files with name ending with:
-strings: geophone strings
-hydro: single hydrophones (5 m depth)

-3c: single 3-component geophones
-obn: ocean bottom nodes (Trilobits)
-nearfield: hydrophone 2 m below airgun

Files with named containg 'dc' are with detonating cord as source.
Shot coordinates refer to the midpoint of the line source.

Files with named containg 'dc2' are also with detonating cord as source.
These files contain some duplicate shots (same positions as in 'dc' files).

Files with names containing 'ag' are with an air gun (Mini G) as source.
There are 6 shots in each position with depths 4,4,3,3,2,2 m.

Files with names containing 'ag2' are with an other air gun (Bolt LLX 1900) as source (due to problems with the Mini G airgun).
There are 3 shots in each position, all at 4 m depths.

C.2 Copy of 'README_instrumentation.txt' file

Recording nodes used for geophone strings and single hydrophones: Sercel UNITE RAU3. Conversion factor at 0 dB gain: 2.697e-4 mV/count, at 12 dB gain: 6.742e-5 mV/count. Gain was set to 0 dB in 2013 and to 12 dB for 2016, 2017, and 2018. The SEG-Y files recorded with the Unite system are organized in shot gather (sorted by FFID).

Geophone strings consist of SM-4 14 Hz elements, each with a 453 Ohm shunt, connnected in series of 8. The effective string sensitivity is 126 V/(m/s) and the damping is 0.70.

3C geophones: DT-Solo 10 Hz (1 Vertical and 2 Horizontal components). Effective sensitivity 78.7 V/(m/s) and damping 0.70 for all components. Components are identified by byte 29-30 in the SEG-Y trace header: 12=vertical comp., 13=transverse (cross-line) comp., 14=radial (in-line) comp.

Hydrophones: transformer coupled with an instrument response similar to a 10 Hz geophone. Sensitivity 13.3 V/Bar with 0.70 damping.

Nearfield hydrophone: for the airgun shots in 2017 and 2018 a hydrophone was deployed 2 m below the airgun. This hydrophone had a different (lower) sensitivity and respons than the other hydrophones, but this has been corrected for. The FFIDs are exactly the same as in the other files.

Trilobits (ocean bottom nodes) contain 1 hydrophone and 3 geophones in a Galperin configuration. Hydrophone sensitivity 2.81e-4 uBar/count, response (low cut) -3dB at 3.6 Hz, -6 dB/oct. Geophone sensitivity 8.97e-6 (um/s)/count, response (low cut) -3dB at 14 Hz, -12 dB/oct. To compute the vertical component, one can stack the 3 geophones and multiply with 0.577. To convert to radial and transverse components, it is necessary to first find the orientation of the OBN (from shots at known location). See EBCDIC header for the meaning

of SEG-Y header words (FFID in byte 139-140, source position in byte 17-20, and receiver position in byte 9-12). The OBN files for 2016 are organized in a different way than the 2017 and 2018 files. See the README file in the 2016/Trilobits folder. The OBN SEG-Y files are recorded as receiver gathers (all other SEG-Y files are shot gathers).

Appendix D

Instrumentation specifications for sources and receivers

Table D.1: Specifications for the sources used in the Svea 2018 experiment.

Source	Model / type	Specification	Unit	Value
Detonating cords	Nobelcord[1]	Mass	kg	2
		Length	m	25
Airgun	Sercel Mini G 12[2]	Volume	cu. in.	12
		Length/width	mm	390/200
		Weight	kg	25.4
		Air pressure	Bar	130
Airgun 2	Bolt LLX 1900[3]	Volume	cu. in.	40
		Length/width	mm	-
		Weight	kg	-
		Air pressure	Bar	130

Source manufacturers: (1): Orica Mining Services, (2): Sercel (3): Teledyne Marine.

Table D.2: Specifications for the receivers used in the Svea 2018 experiment.

Reciever	**Model / type**	**Specification**	**Unit**	**Value**
Recording nodes	Sercel UNITE RAU3[(1)]	Conv. factor @ 12 dB	mV/count	$6.742 \cdot 10^{-5}$
Geophone strings	SM-4[(2)]	Center frequency	Hz	14
		DC resistance	Ohm	453
		Effective sensitivity	V/(m/s)	126
		Damping		0.70
3C geophone	DT-Solo[(3)]	Center frequency	Hz	10
		Effective sensitivity	V/(m/s)	78.7
		Damping		0.70
Hydrophone	T-coupled[(4)]	Center frequency	Hz	10
		Effective sensitivity	V/bar	13.3
		Damping		0.70
OBN (hydrophone)	Trilobite[(5)]	Center frequency	Hz	-
		Effective sensitivity	μBar/count	$2.81 \cdot 10^{-4}$
		Response @ 3.6 Hz	dB	- 3
			dB/oct.	-6
OBN (geophone)	Trilobite[(5)]	Center frequency	Hz	-
		Effective sensitivity	(μm/s)/count	$8.97 \cdot 10^{-6}$
		Response @ 14 Hz	dB	- 3
			dB/oct.	- 12

Receiver manufacturers: (1): Sercel, (2): , (3): , (4): , (5): Seabed Geosolutions.

Appendix E

Example of input file to OASES-OASP

	Block	Input	Description
I	Title	input_OASES_OASP_Svea_2018	Title of run
II	Output options	V	Vertical particle velocity calculated
		H	Horizontal particle velocity calculated
		N	Normal stress/negative pressure in fluids
		0	Complex frequency integration contour
		f	Full Hankel transform integration scheme
III	Source freq.	10	Center frequency of source (Hz)
		0	Integration contour offset (dB/λ)
IV	Environmental model	7	Number of layers, including halfspaces
	Layer I (air upper halfsp.)	0.0 325.0 0.0 0.0 0.0 0.0013 0.0	z_m v_p v_s α_p α_s ρ $N_v(\Delta\underline{r})$
	Layer II (Ice top layer)	0.0 3000.0 1500.0 0.1 0.1 0.920 0.0	..
	Layer III (Ice bottom layer)	0.1 1600.0 800.0 0.1 0.1 0.920 0.0	..
	Layer IV (water)	0.3 1500.0 0.0 0.1 0.1 1.030 0.0	..
	⋮	⋮	..
V	Sources	4.00	Source depth (m)
VI	Receiver depths	19.4	Depth of first receiver (m)
		19.4	Depth of last receiver (m)
		1	Number of receiver depths
VII	Wavenumber	-1 (auto)	Number of wavenumber samples
	sampling	10	Minimum phase velocity (m/s)
		1E8	Maximum phase velocity (m/s)
		0	Freq. sample incr. for kernels
VIII	Frequency and	10000	Number of time samples (2^n)
	range sampling	1.0	Lower limit freq. band (Hz)
		40.0	Upper limit freq. band (Hz)
		0.001	Time sampling increment (s)
		0.0	First range (m)
		0.001	Range increment (m)
		501	Number of ranges

Appendix F

'run_OASES_model.csh'

The script 'run_model.csh' is a C shell script which runs the OASES-OASP with a given input environmental model, see an example of input in appendix E. The 'run_model.csh' calls up an 'asc2su'-script, which calls upon an 'writesu'-script, which converts output ASCII-file from OASES-OASP to SU-compatible file.

```
#!/bin/csh

#=============================================================================
#                          RUN OASES-OASP MODEL
#
# Example of script to run the OASES-OASP model.
#
# AUTHOR: ERIK LARSEN
# INSTITUTE OF PHYSICS AND TECHNOLOGY
# UNIVERSITY OG BERGEN
# August-November, 2020
#
#=============================================================================

set model = OASES_Svea_AG2_OBN_hydro_shot_183    # name input model
set input = input_$model.dat                     # convert input model to DAT-file
set inp_trf = input.trf                          # set input file for transfer
    functions to be calculated (recommended to be named ''input.trf'')

# Direct to executable directory path where OASES is built
setenv OASES_SH ${HOME}/oases-build/bin      # OASES scripts
setenv OASES_BIN ${HOME}/oases-build/bin     # OASES executables
setenv OASES_LIB ${HOME}/oases-build/lib     # OASES libraries
set path = ($OASES_SH $OASES_BIN $path)      # set path to OASES scripts
setenv USRTERMTYPE x                         # set display environment variable
rehash                                       # recomputes the internal hash table of
    the contents of directories listed in the path environmental variable to account
    for new commands added.

```

```
rm -f input.* fort.*        # force remove files with names 'input.*' and 'fort.*', where '*' indicates arbitrary format
cp -f $input input.dat      # force copy of the input file to DAT-format
oasp input                  # start OASES-OASP script

# Inputs to the Post Processor (PP) in OASES
pp input << EOF             # Input the list to the PP
1
$inp_trf
2
1
11
18
$model
19
22
EOF

# Description of the input options to PP
#1                         # choose inp. file to OASES (standard)
#$inp_trf                  # name inp. file to OASES (standard)
#2                         # source type:
#1                         # source type: 1: Explosive (omnidirectional) sources.
#11                        # Range stacked:
#18                        # Range stacked: Trace file
#$model                    # Range stacked: Trace file: "OASES_Svea_AG2_OBN_hydro_shot_183" (ASCII file)
#19                        # Return (PP main menu)
#22                        # Exit PP:


#chmod +x asc2su.f         # change the mode of each FILE to MODE (if the '*.csh' file does not want to run
./asc2su << EOF            # call the 'asc2su' script to convert from asc file to SU-compatible file
$model                     # name the file to 'asc2su' script
EOF

exit
```

Appendix G

'asc2su.f'

The 'asc2su.f' and 'writesu.f' scripts were created and handed out by senior engineer Bent Ole Ruud (UiB).

```
      parameter (nrmax=300, ntmax=10000)
      real trc(ntmax,nrmax), offset(nrmax), depth(nrmax),
     +     azi(nrmax), t0(nrmax)
      character*40 filename
      character*1 comp

      write(*,*)'Name of ascii file (without .asc-ending):'
      read(*,*) filename
      open(unit=7,file=trim(filename)//'.asc',status='old')
      read(7,*)
      read(7,'(a)') comp
      read(7,*) npl
      read(7,*) nr
      read(7,*) nt
      read(7,*) srate

      do j=1,nr
        read(7,*)
        read(7,*) offset(j)
        read(7,*) depth(j)
        read(7,*) azi(j)
        read(7,*) t0(j)
        read(7,*)(trc(i,j),i=1,nt)
      enddo
      close(7)

      call writesu(trc,ntmax,nt,nr,1/srate,offset,trim(filename)//'.su')

      end
```

Appendix H

'writesu.f'

```
1             subroutine writesu(trace,maxsmp,nsamp,nchan,smpint,offset,filen)
2       real trace(maxsmp,*), offset(*)
3       character*(*) filen
4 c-------------------------------------------------------------------------
5 c     Write a shot gather in Seismic Unix format
6 c
7 c     trace(nsamp,nchan) - traces
8 c     maxsmp - declared maximum number of samples per trace
9 c     nsamp - actual number of samples per trace
10 c     nchan - number of traces
11 c     smpint - sample interval (s)
12 c     offset(nchan) - offset of traces (m)
13 c     filen - filename
14 c
15 c                                    Author: Bent O. Ruud
16 c                                    Institute of Solid Earth Physic
17 c                                    University of Bergen
18 c                                    e-mail: BentOle.Ruud@ifjf.uib.no
19 c-------------------------------------------------------------------------
20       integer*4 trchead4(60)
21       integer*2 trchead2(120)
22       equivalence (trchead2(1),trchead4(1))
23       logical lopen,lexist
24       data shotx,shoty,shotz/0.,0.,0./
25       data chany,chanz/0.,0./
26       data isrc,idtrc,iscalev,iscaleh,imeasu/1,1,0,0,1/
27       data iunit/20/
28 c
29 c  open su trace data file as a fortran direct access file
30 c
31       lrec = 240 + 4*nsamp
32 c  find a free unit number
33  10   iunit = iunit + 1
34       inquire(unit=iunit,opened=lopen)
```

```
35       if (lopen) goto 10
36 c  delete old file with same name if it exists
37       inquire(file=filen,exist=lexist)
38       if (lexist) then
39         open(iunit,file=filen,status='old',access='direct',
40      +    form='unformatted',recl=lrec)
41         close(iunit,status='delete')
42       endif
43 c  open new file
44       open(iunit,file=filen,status='new',access='direct',
45      + form='unformatted',recl=lrec)
46 c
47 c  initiate trace header
48 c
49       do 30 i=1,60
50  30   trchead4(i) = 0
51 c
52 c  set some parameters in trace header
53 c
54       trchead4(3) = isrc
55       trchead4(5) = isrc
56       trchead4(11) = chanz
57       trchead4(13) = shotz
58       trchead2(15) = idtrc
59       trchead2(35) = iscalev
60       trchead2(36) = iscaleh
61       trchead4(19) = shotx
62       trchead4(20) = shoty
63       trchead4(22) = chany
64       trchead2(45) = imeasu
65       trchead2(58) = nsamp
66       trchead2(59) = int(smpint*1000000+0.5)
67 c
68 c  write trace records
69 c
70       do 300 k=1,nchan
71          trchead4(1) = k
72          trchead4(2) = k
73          trchead4(4) = k
74          trchead4(10) = int(offset(k)+0.5)
75          trchead4(21) = int(shotx+offset(k)+0.5)
76          write(iunit,rec=k)
77      +      (trchead4(i),i=1,60),(trace(i,k),i=1,nsamp)
78  300  continue
79       close(iunit,status='keep')
80       return
81       end
```

Appendix I

'plot_seis_OASES.sh'

Script for plotting seismograms, $f-k$ and $f-v$ spectra of results from OASES-OASP

```
#!/bin/sh

#=============================================================================
#                    PLOT RESULTS FROM OASES-OASP USING SEISMIC UNIX (SU)
#
# Example of script to plot seismograms (supswigp), F-K (suspecfk) and F-V (suphasevel)
# spectra for results from OASES-OASP.
#
# Some useful Seimic Unix codes used
#  -> SEGYREAD - read an SEG-Y tape
#  -> SUWIND - window traces by key word
#  -> SUPSWIGP - PostScript Polygon-filled WIGgle plot of a segy data set
#  -> SUSPECFK - F-K Fourier SPECtrum of data set
#  -> SUPSIMAGE - PostScript IMAGE plot of a segy data set
#  -> SUSPECFX - Fourier SPECtrum (T -> F) of traces
#  -> SUPHASEVEL - Multi-mode PHASE VELocity dispersion map computed from shots
#
# AUTHOR: ERIK LARSEN
# INSTITUTE OF PHYSICS AND TECHNOLOGY
# UNIVERSITY OG BERGEN
# August-November, 2020
#
#=============================================================================
#                              DEFINE INPUT DATA
#=============================================================================

representative_model=OASES_Svea_AG2_OBN_hydro_shot_183  # name the model
sufile_model=$representative_model.su             # name a SU file of the model
surange < OASES_Svea_AG2_OBN_hydro_shot_183.su >
    surange_OASES_Svea_AG2_OBN_hydro_shot_183.txt # create a TXT-file with the max and
     min values for header entries
```

```
shot=183     # representable shot number to measurement results
filt=1,2,20,40  # frequency filter coefficients
minOffset=50     # set minimum offset to be plotted
maxOffset=350    # set maximin offset to be plotted
widthbox=5.0     # set width of window size
heightbox=6.0    # set height of window size
tpower=1     # gain control: t^tpow
timeMax=6    # max time to be plotted in seismogram
jth=5        # pass over every j-th trace, choose interval for traces (1: dx=2m, 2: dx=4m, dx = 2.5m, 2dx = 5m, 3d = 7.5m)
sth=0        # pass over every j-th trace... based at s, choose odd traces with s=1
fmax=20.5    # max frequency to be plotted in f-k and f-v domains
title="OASES A: dx = $jth m, normal stress" # title of plots

#=============================================================================
#                              SEISMOGRAM PLOT
#=============================================================================

# name output PostScript (PS)-file for seismogram
psfile_model_seis=out_OASES_AG2_OBN_hydro_seis_shot_183.ps

# make a window with keyword tracl (Trace sequence number within line), and add to output seismogram PS-file
suwind key=tracl < $sufile_model |

# Processing
suwind key=tracl min=$minOffset max=$maxOffset tmax=$timeMax s=$sth j=$jth |    # Set wanted min and max offset and t_max, and receiver interval dx
sugain mbal=1 |          # gain control mbal: balance traces by subtracting the mean
sugain tpow=$tpower |    # gain control tow: multiply data by t^tpow
sufilter f=$filt |       # apply a zero-phase, sine-squared tapered filter: Ormsby BP filter

# Ploting
supswigp key=tracl perc=99.9 wbox=$widthbox hbox=$heightbox d2num=50 n2tic=2 n1tic=2 d1num=1 label1="Time (s)"\ label2="Offset (m)" title="$title" titlesize=18 verbose=1 > $psfile_model_seis # PostScript IMAGE plot of a segy data set, printed as a PostScript file formatted ".ps"

#=============================================================================
#                          F-K (FREQUENCY-WAVENUMBER) PLOT
#=============================================================================

# name output PostScript (PS)-file for F-K spectrum
psfile_model_FK=out_OASES_AG2_OBN_hydro_FK_shot_183.ps

# Color smoothing factors
```

```
d1sFK=0.250      # 0.25 factor by which to scale d1 (sampling interval in 1st (fast) dimension) before imaging
d2sFK=0.125      # 0.125 factor by which to scale d2 (sampling interval in 2nd (slow) dimension) before imaging

# make a window with keyword tracl (Trace sequence number within line), and add to output F-K PS-file
suwind key=tracl < $sufile_model |

# Processing
suwind key=tracl s=$sth j=$jth min=$minOffset max=$maxOffset tmax=$timeMax | # Set wanted min and max offset and t_max, and the receiver spacing dx
sugain mbal=1 |          # gain control mbal: balance traces by subtracting the max
sugain tpow=$tpower |    # gain control tpow: multiply data by t^tpow
sufilter f=$filt |       # apply a zero-phase, sine-squared tapered filter: Ormsby BP filter
suspecfk dx=$jth verbose=1 |    # F-K Fourier SPECtrum of data set, dx: spatial sampling interval

# Define color map - HLS definitions (H: hue, L:Luminance, S:Saturation) for better intermediate color interpolation. Example of definitions: bhls=0.666666,.5,1: blue, ghls=0.333333,.5,1: green, whls=0,.5,1: red
# Imaging
supsimage style=seismic d1s=$d1sFK d2s=$d2sFK width=$widthbox height=$heightbox x1beg=0 x1end=$fmax n1tic=5 n2tic=5 bps=24 bhls=0,0.5,1 ghls = 0.5,0.5,1 whls=0.66666,0.15,1 perc=99.9 verbose=1 legend=1 lnice=1 units="|Amplitude| (Pa)" title="F-K $title" titlesize=18 label1="Frequency (Hz)" label2="Wavenumber (1/m)" > $psfile_model_FK # PostScript IMAGE plot of a segy data set, printed at a PostScript file formatted ".ps"

#=============================================================================
#                        F-V (FREQUENCY-PHASE VELOCITY) PLOT
#=============================================================================

# name output PostScript (PS)-file for F-V spectrum
psfile_model_FV=out_OASES_AG2_OBN_hydro_FV_shot_183.ps
# Resolution limit TXT-file for spatial aliasing (v_max = dx * f_max): (0,0 - 40,200)
spat_alias_AG2_OBN_model=AG2_OBN_spatial_aliasing_coord_model.asc

# Color smoothening factors
d1sFV=0.250      # 0.25 factor by which to scale d1 (sampling interval in 1st (fast) dimension) before imaging
d2sFV=0.125      # 0.125 factor by which to scale d2 (sampling interval in 2nd (slow) dimension) before imaging

# make a window with keyword tracl (Trace sequence number within line), and add to F-V PS-file
suwind key=tracl < $sufile_model |
```

```
102
103 # Processing
104 suwind key=tracl s=$sth j=$jth min=$minOffset max=$maxOffset tmax=$timeMax |     # Set
    wanted min and max offset and t_max, and the receiver spacing dx
105 sugain mbal=1 |          # gain control mbal: balance traces by subtracting the max
106 sugain tpow=$tpower |    # gain control tpow: multiply data by t^tpow
107 sufilter f=$filt |       # apply a zero-phase, sine-squared tapered filter: Ormsby BP
    filter
108 suphasevel fv=0 nv=500 dv=1 fmax=$fmax norm=0 | # Multi-mode PHASE VELocity dispersion
     map computed from shot record(s), fv: min phase velocity (m/s), nv: number of
    phase velocities, dv: phase velocity step (m/s), fmax: maximum frequency in
    process (Hz), norm: normalize by amplitude spectrum
109 suamp | # output amp, phase, real or imag trace from (frequency, x) domain data
110
111 # Define color map - HLS definitions (H: hue, L:Luminance, S:Saturation) for better
    intermediate color interpolation
112 # Example of definitions: bhls=0.666666,.5,1: blue, ghls=0.333333,.5,1: green, whls
    =0,.5,1: red
113 # Imaging
114 supsimage style=normal d1s=$d1sFV d2s=$d2sFV width=$widthbox height=$heightbox x1beg=0
     x1end=$fmax n1tic=5 n2tic=5 perc=99.5 curve=$spat_alias_AG2_OBN_model curvewidth
    =2 curvecolor=white npair=2 curvedash=4 label1="Frequency (Hz)" label2="Phase
    velocity (m/s)" bps=24 bhls=0,0.5,1 ghls=0.5,0.5,1 whls=0.66666,0.15,1 legend=1
    lnice=1 units="Complex amplitude (Pa)" title="F-V $title" titlesize=18 >
    $psfile_model_FV  # PostScript IMAGE plot of a segy data set, printes at a
    PostScript file formatted ".ps"
115
116 #=============================================================================
117 #                                END OF SCRIPT
118 #=============================================================================
119
120 exit            # THIS MUST BE THE LAST COMMAND
```

Appendix J

'plot_shot_OBN_AG2_hydro.sh'

Shell script for plotting seismograms, $f-k$ and $f-v$ spectra of results from Svea 2018 seismic experiment. This script is for source: AG2: Bolt LLX 1900 airgun and receivers: OBNs (trilobites) - hydrophones (normal stress). To plot the AG2-OBN - 3C geophones results, one should change the trace identification codes *'key=trid min=11 max=11'* (Seismic pressure sensor), to *'key=trid min=12 max=14'* (Multi component seismic sensor) [23], to read the data from the OBN three component geophones instead of from the hydrophone data.

```
#!/bin/sh
#=============================================================================
#   PLOT SEISMOGRAMS, F-K & F-V SPECTRA OF SVEA 2018
#                       SEISMIC DATASETS
#
#                 AIRGUN2: BOLT LLX 1900
#
#              TRILOBITE (4C OBN) - HYDROPHONES
#
fname=plot_shot_obn_ag2_hydro.sh     # name of this file
#
# Script which reads seismic shot data (generated by AG2: air gun (Bolt LLX 1900)
# recorded by trilobits (4C OBN)) from the Svea 2018 seismic recordings. This script
# processes the data and plots the resulting seismogram, F-K and F-V spectra of the
# chosen shot and node station numbers in two separate PostScript files at the folder
# where it runs the script. The user must choose which shot- and node station numbers
# to process, and the resulting plots are named "..._hydro_..." and # "..._vertC_..."
# to differ between normal stress (hydrophones) and particle velocity components (3C
# geophones) results. This script plots the neg. pressure (hydrophones) amplitude
# data. Additionally the user can plot estimated group velocity lines on the
# seismogram. The P-velocities for the direct P-wave (generated by the airgun, wave
# traveling in water) is plotted in blue, the first wave packet (Scholte wave) is
# plotted in red and the second (Scholte wave) is plotted in green. The coordinates
# for the velocity-lines are read by SU from three different ASCII-formatted files,
# with start (x1, y1) and end coordinates (x2, y2) sorted as:
#
```

```
# x1, y1
# x2, y2
#
# The user can choose whether to i) not include the group velocity estimated lines
# (plain shot gather), ii) include the group velocity estimated lines (mean velocity
# estimate) and iii) include three group velocity estimated lines with different
# colors.
#
# Some useful Seimic Unix codes used:
#  -> SEGYREAD - read an SEG-Y tape
#  -> SUWIND - window traces by key word
#  -> SUPSWIGP - PostScript Polygon-filled WIGgle plot of a segy data set
#  -> SUSPECFK - F-K Fourier SPECtrum of data set
#  -> SUPSIMAGE - PostScript IMAGE of a segy data set
#  -> SUSPECFX - Fourier SPECtrum (T -> F) of traces
#  -> SUPHASEVEL - Multi-mode PHASE VELocity dispersion map computed from shots
#
# AUTHOR:
#
# Erik Larsen
# Institute of Physics and Technology
# University of Bergen
# Allegt. 55
# N-5007 Bergen, Norway
# EMAIL: Erik.L@uib.no
# August-November 2020
#
#============================================================================================

#--------------------------------------------------------------------------------------------
#                DEFINE INPUT DATA
#--------------------------------------------------------------------------------------------

SEG-Y file=svea_2018_ag2_obn.segy   # Name of SEG-Y file containing measurement data
shot=183          # choose shot number
rmin=65           # Define min node station number
rmax=80           # Define max node station number
tmax=8            # Define max record length (on time-axis) plotted (sec)
filt=1,2,20,40  # frequency filter coeff.; a zero phase, sine-squared tapered filter:
    Ormsby bandpass filter
fmax=20.5         # max freq. in F-K & F-V to be plotted
tpower=1          # gain control: multiply data by t^tpow
labelsized=24   # Define label size (default = 18)

# Pre-defined curve files for group velocity estimations by curvefitting
c_dirP=coord_dirP_shot_$shot.asc    # direct P-wave vel. curve
c_dirP_above=coord_dirP_above_shot_$shot.asc    # direct P-wave vel. curve above
c_dirP_below=coord_dirP_below_shot_$shot.asc    # direct P-wave vel. curve below
```

```
c_first=coord_first_shot_$shot.asc          # 1st group vel. curve
c_first_above=coord_first_above_shot_$shot.asc  # 1st group vel. curve above
c_first_below=coord_first_below_shot_$shot.asc  # 1st group vel. curve below
c_second=coord_second_shot_$shot.asc            # 2nd group vel. curve
c_second_above=coord_second_above_shot_$shot.asc    # 2nd group vel. curve above
c_second_below=coord_second_below_shot_$shot.asc    # 2nd group vel. curve below

title="Shot $shot: dx = 25 m, OBN - normal stress"      # title heading output files
#
#-------------------------------------------------------------------------------
#               SEISMOGRAM (X-T DOMAIN) PLOT
#-------------------------------------------------------------------------------
# NAME OUTPUT FILENAMES FOR THREE SEISMOGRAMS
psfileWhydro=out_svea_2018_ag2_obn_hydro_seis_shot_$shot.ps      # seismogram
psfileWhydro_vel=out_svea_2018_ag2_obn_hydro_seis_vel_shot_$shot.ps      # seismogram group vel. lines 1
psfileWhydro_vel_approx=out_svea_2018_ag2_obn_hydro_seis_vel_approx_shot_$shot.ps   # seismogram group vel. lines 2
#-------------------------------------------------------------------------------
# READ data from SEG-Y file
segyread tape=$SEG-Y_file |                 # read SEG-Y file
suwind key=ep min=$shot max=$shot tmax=$tmax |  # read shot point numbers
suwind key=fldr min=$rmin max=$rmax |       # read node station number
suwind key=trid min=11 max=11 |             # use this for normal stress (hydrophones)
#suwind key=trid min=12 max=14 | # use this for vertical particle velocity components
#                               (12: vertical, 13: cross-line, 14: in-line)
# PROCESSING
sugain mbal=1 |         # gain control: 1 = balance traces by subtracting the max
sustack key=offset |    # stack adjacent traces having header word = offset
sugain tpow=$tpower |   # gain control: multiply data by t^tpow
sufilter f=$filt |      # applies a zero-phase, sine-squared tapered filter: Ormsby BP filter

# PLOTTING NORMAL STRESS AMPLTITUDES, NO GROUP VEL. LINES
suwind key=offset tmax=$tmax |  # Choose max travel time (s) to be plotted
supswigp style=seismic key=offset perc=99.9 verbose=1 label1="Time (s)" n1tic=2 d1num=1 n2tic=2 d2num=50 x2end=365 label2="Offset (m)" title="$title"  > $psfileWhydro &    # PostScript Polygon-filled WIGgle plot of a segy data set, converted to a PostScript file formatted ".ps" - Normal stress, NO GROUP VEL. LINES

# READ data from SEG-Y file
segyread tape=$SEG-Y_file |                 # read SEG-Y file
suwind key=ep min=$shot max=$shot tmax=$tmax |  # read Shot point number
suwind key=fldr min=$rmin max=$rmax |       # read node station number
suwind key=trid min=11 max=11 |             # use this for normal stress (hydrophones)
#suwind key=trid min=12 max=14 | # use this for vertical particle velocity components
#                               (12: vertical, 13: cross-line, 14: in-line)
# PROCESSING
```

```
116 sugain mbal=1 |       # gain control: 1 = balance traces by subtracting the max
117 sustack key=offset |  # stack adjacent traces having key header word = offset
118 sugain tpow=$tpower | # gain control: multiply data by t^tpow
119 sufilter f=$filt |    # applies a zero-phase, sine-squared tapered filter: Ormsby BP
        filter
120
121 # PLOTTING NORMAL STRESS AMPLITUDES, GROUP VELOCITY ESTIMATIONS LARGEST AMPLITUDES
122 suwind key=offset tmax=$tmax |  # Choose max travel time (s) to be plotted
123 supswigp style=seismic key=offset perc=99.9 verbose=1 label1="Time (s)" n1tic=2 dlnum
        =1 n2tic=2 d2num=50 x2end=365 label2="Offset (m)" title="$title"  curve=$c_dirP,
        $c_first,$c_second curvewidth=2,2,2 curvecolor=blue,red,green npair=2,2,2
        curvedash=0,0,0 > $psfileWhydro_vel &     # PostScript Polygon-filled WIGgle plot
        of a segy data set, converted to a PostScript file formatted ".ps" - Normal stress
        , GROUP VELOCITY ESTIMATIONS LARGEST AMPLITUDES
124
125 # READ data from SEG-Y file
126 segyread tape=$SEG-Y file |                 # read SEG-Y file
127 suwind key=ep min=$shot max=$shot tmax=$tmax |  # read shot point numbers
128 suwind key=fldr min=$rmin max=$rmax |       # read node station number
129 suwind key=trid min=11 max=11 |             # use this for normal stress (hydrophones)
130 #suwind key=trid min=12 max=14 | # use this for vertical particle velocity components
131 #                               (12: vertical, 13: cross-line, 14: in-line)
132 # PROCESSING
133 sugain mbal=1 |         # gain control: 1 = balance traces by subtracting the max
134 sustack key=offset |    # stack adjacent traces having header word = offset
135 sugain tpow=$tpower |   # gain control: multiply data by t^tpow
136 sufilter f=$filt |      # applies a zero-phase, sine-squared tapered filter: Ormsby BP
        filter
137
138 # PLOTTING NORMAL STRESS AMPLITUDES, GROUP VELOCITY ESTIMATIONS THREE LINES LARGEST
        AMPLITUDES
139 suwind key=offset tmax=$tmax |  # Choose max travel time (s) to be plotted
140 supswigp style=seismic key=offset perc=99.9 verbose=1 label1="Time (s)" n1tic=2 dlnum
        =1 n2tic=2 d2num=50 x2end=365 label2="Offset (m)" title="$title"  curve=$c_dirP,
        $c_dirP_above,$c_dirP_below,$c_first,$c_first_above,$c_first_below,$c_second,
        $c_second_above,$c_second_below curvewidth=2,1,1,2,1,1,2,1,1 curvecolor=blue,blue,
        blue,red,red,red,green,green,green npair=2,2,2,2,2,2,2,2,2 curvedash
        =0,0,0,0,0,0,0,0,0 > $psfileWhydro_vel_approx      # PostScript Polygon-filled
        WIGgle plot of a segy data set, converted to a PostScript file formatted ".ps" -
        Normal stress, GROUP VELOCITY ESTIMATIONS THREE LINES LARGEST AMPLITUDES
141
142 #-------------------------------------------------------------------------------
143 #               F-K (FREQUENCY-WAVENUMBER DOMAIN) SPECTRUM
144 #-------------------------------------------------------------------------------
145 # NAME postscript output file for F-K spectrum
146 psfileFKhydro=out_svea_2018_ag2_obn_hydro_fk_shot_$shot.ps
147
148 # color smoothing factors
```

```
d1sFK=0.250  # 0.25 factor by which to scale d1 (sampling interval in 1st (fast) dimension) before imaging
d2sFK=0.125  # 0.125 factor by which to scale d2 (sampling interval in 2nd (slow) dimension) before imaging

# READ data from SEG-Y file
segyread tape=$SEG-Y_file |                  # read SEG-Y file
suwind key=ep min=$shot max=$shot tmax=$tmax |  # read shot point numbers
suwind key=fldr min=$rmin max=$rmax |        # read node station number
suwind key=trid min=11 max=11 |              # use this for normal stress (hydrophones)
#suwind key=trid min=12 max=14 | # use this for vertical particle velocity components
#                                (12: vertical, 13: cross-line, 14: in-line)
# PROCESSING
sugain mbal=1 |          # gain control: 1 = balance traces by subtracting the max
sustack key=offset |     # stack adjacent traces having header word = offset
sugain tpow=$tpower |    # gain control: multiply data by t^tpow
sufilter f=$filt |       # applies a zero-phase, sine-squared tapered filter: Ormsby BP filter

# IMAGING
suwind tmax=$fmax |              # max frequency to plot
# Define color map - HLS definitions (H: hue, L:Luminance, S:Saturation) for better
# intermediate color interpolation. Example of definitions:
#       bhls=0.666666,.5,1: blue, ghls=0.333333,.5,1: green, whls=0,.5,1: red
supsimage style=seismic d1s=$d1sFK d2s=$d2sFK x1beg=0 x1end=$fmax n1tic=5 n2tic=4 bps=24 bhls=0,0.5,1 ghls=0.5,0.5,1 whls=0.66666,0.15,1 perc=99.9 verbose=1  legend=1 lnice=1 units="|Amplitude|" title="F-K $title" labelsize=$labelsized label1="Frequency (Hz)" label2="Wavenumber (1/m)" > $psfileFKhydro  # PostScript image of a segy data set, printes at a PostScript file formatted ".ps"  - normal stress

#-------------------------------------------------------------------------------
#                    F-V (FREQUENCY-PHASE VELOCITY) SPECTRUM
#-------------------------------------------------------------------------------
# NAME PostScript file for F-V spectrum
psfilePHOBNAG2=out_svea_2018_ag2_obn_hydro_PhaseVel_shot_$shot.ps
# Resolution limit file for spatial aliasing
spat_alias_AG2_OBN=AG2_OBN_spatial_aliasing_coord.asc

# color smoothing factors
d1sFV=0.250  # factor by which to scale d1 (sampling interval in 1st (fast) dimension) before imaging
d2sFV=0.125  # factor by which to scale d2 (sampling interval in 2nd (slow) dimension) before imaging

# READ data from SEG-Y file
segyread tape=$SEG-Y_file |                  # read SEG-Y file
suwind key=ep min=$shot max=$shot tmax=$tmax |  # read shot point numbers
suwind key=fldr min=$rmin max=$rmax |        # read node station number
```

```
suwind key=trid min=11 max=11 |             # use this for normal stress (hydrophones)
#suwind key=trid min=12 max=14 | # use this for vertical particle velocity components
#                                (12: vertical, 13: cross-line, 14: in-line)
# PROCESSING
sugain mbal=1 |          # gain control: 1 = balance traces by subtracting the max
sustack key=offset |     # stack adjacent traces having header word = offset
sugain tpow=$tpower |    # gain control: multiply data by t^tpow
sufilter f=$filt |       # applies a zero-phase, sine-squared tapered filter: Ormsby BP
    filter
suphasevel fv=0 nv=500 dv=1 fmax=$fmax norm=0 | # Multi-mode PHASE VELocity dispersion
    map computed from shot record(s), fv: min phase velocity (m/s), nv: number of
    phase velocities, dv: phase velocity step (m/s), fmax: maximum frequency in
    process (Hz), norm: normalize by amplitude spectrum
suamp |                                  # output amp, phase, real or imag trace
    from (frequency, x) domain data

# IMAGING
# Define color map - HLS definitions (H: hue, L:Luminance, S:Saturation) for better
# intermediate color interpolation. Example of definitions:
#       bhls=0.666666,.5,1: blue, ghls=0.333333,.5,1: green, whls=0,.5,1: red
supsimage style=normal d1s=$d1sFV d2s=$d2sFV x1beg=0 x1end=$fmax n1tic=5 d1num=5 n2tic
    =5 d2num=100 perc=99.5 curve=$spat_alias_AG2_OBN curvewidth=2  curvecolor=white
    npair=2 curvedash=4 label1="Frequency (Hz)" label2="Phase velocity (m/s)"
    labelsize=$labelsized bps=24 bhls=0,0.5,1 ghls=0.5,0.5,1 whls=0.66666,0.15,1 hbox
    =600 wbox=900 legend=1 lnice=1 units="|Amplitude|" title="F-V $title" >
    $psfilePHOBNAG2     # PostScript image of a segy data set, printes at a PostScript
     file formatted ".ps" - normal stress

#-------------------------------------------------------------------------------
#   NORMALIZED F-V (PHASE VELOCITY) SPECTRUM (NORMALIZED NORMAL STRESS AMPLITUDES)
#-------------------------------------------------------------------------------
# NAME PostScript file for normalized F-V spectrum
psfilePHOBNAG2_norm=out_svea_2018_ag2_obn_hydro_PhaseVel_norm_shot_$shot.ps
# Resolution limit file for spatial aliasing
spat_alias_AG2_OBN=AG2_OBN_spatial_aliasing_coord.asc

# color smoothing factors
d1sFV=0.250  # factor by which to scale d1 (sampling interval in 1st (fast) dimension)
     before imaging
d2sFV=0.125  # factor by which to scale d2 (sampling interval in 2nd (slow) dimension)
     before imaging

# READ data from SEG-Y file
segyread tape=$SEG-Y file |              # read SEG-Y file
suwind key=ep min=$shot max=$shot tmax=$tmax |  # read shot point numbers
suwind key=fldr min=$rmin max=$rmax |    # read node station number
suwind key=trid min=11 max=11 |          # use this for normal stress (hydrophones)
#suwind key=trid min=12 max=14 | # use this for vertical particle velocity components
```

```
223 #                                   (12: vertical, 13: cross-line, 14: in-line)
224 # PROCESSING
225 sugain mbal=1 |          # gain control: 1 = balance traces by subtracting the max
226 sustack key=offset |     # stack adjacent traces having header word = offset
227 sugain tpow=$tpower |    # gain control: multiply data by t^tpow
228 sufilter f=$filt |       # applies a zero-phase, sine-squared tapered filter: Ormsby BP
        filter
229 suphasevel fv=0 nv=500 dv=1 fmax=$fmax norm=1 |          # Multi-mode PHASE VELocity
    dispersion map computed from shot record(s), fv: min phase velocity (m/s), nv:
    number of phase velocities, dv: phase velocity step (m/s), fmax: maximum frequency
     in process (Hz), norm: normalize by amplitude spectrum
230 suamp |                                  # output amp, phase, real or imag trace from (
    frequency, x) domain data
231
232 # IMAGING
233 # Define color map - HLS definitions (H: hue, L:Luminance, S:Saturation) for better
    intermediate color interpolation
234 # Example of definitions: bhls=0.666666,.5,1: blue, ghls=0.333333,.5,1: green, whls
    =0,.5,1: red
235 supsimage style=normal d1s=$d1sFV d2s=$d2sFV x1beg=0 x1end=$fmax n1tic=5 d2num=5 n2tic
    =5 d2num=100 perc=99.5 curve=$spat_alias_AG2_OBN curvewidth=2  curvecolor=white
    npair=2 curvedash=4 label1="Frequency (Hz)" label2="Phase velocity (m/s)"
    labelsize=$labelsized bps=24 bhls=0,0.5,1 ghls=0.5,0.5,1 whls=0.66666,0.15,1 hbox
    =600 wbox=900 legend=1 lnice=1 units="|Amplitude|" title="F-V $title" >
    $psfilePHOBNAG2_norm      # PostScript image of a segy data set, printes at a
    PostScript file formatted ".ps"
236
237 #-------------------------------------------------------------------------------
238 #               END OF SCRIPT
239 #-------------------------------------------------------------------------------
240 exit         # THIS MUST BE THE LAST COMMAND
```

Appendix K

'plot_shot_AG_3C.sh'

Shell script for plotting seismograms, $f-k$ and $f-v$ spectra of results from Svea 2018 seismic experiment. This script is for source: AG: Sercel Mini G airgun and receivers: 3C geophones (vertical particle velocity).

```
#!/bin/sh
#===============================================================================
#
#  PLOT SEISMOGRAMS, F-K & F-V DOMAIN OF SVEA 2018
#                        SEISMIC DATA
#
#                   AIRGUN: SERCEL MINI G
#
#                        3C GEOPHONES
#

fname=plot_shot_ag_3c.sh        # name of this file

# Script which reads seismic shot data (generated by ag: Sercel Mini G, 12 cu.in.,
# 2000 psi, recorded by 3C geophones DT-Solo 10 Hz (one vertical and two horizontal
# components). Effective sensitivity 78.7 V/(m/s) and damping 0.70 for all components.
# Components are identified by byte 29-30 in the SEGY trace header: 12=vertical
# comp., 13=transverse (cross-line) comp., 14=radial (in-line) comp. This script
# processes the Svea 2018 data set and plots the resulting seismograms, F-K and F-V
# domains of the chosen shot in three separate PostScript files located at the folder
# where running the script. The user chooses which shot numbers to process, and the
# resulting plots are named "out_svea_2018_dc_3c_..._$shot.ps". The F-K and F-V color
# density plots are scaled, by scaling the output factors of F and K/V (respectively
# by "d1s" and "d2s") to get more smooth plots. The factors are decided by trial and
# error, starting from 1 (no scaling) and lowering towards 0. If no scaling, the
# color densities (may) look disturbed and blocky. This script plots the AG-3C
# geophones measurement data from Svea 2018 seismic data-set.
#
# Some useful Seimic Unix codes used
#  -> SEGYREAD - read an SEGY tape
```

```
#  -> SUWIND - window traces by key word
#  -> SUPSWIGP - PostScript Polygon-filled WIGgle plot of a segy data set
#  -> SUSPECFK - F-K Fourier SPECtrum of data set
#  -> SUPSIMAGE - PostScript IMAGE of a segy data set
#  -> SUSPECFX - Fourier SPECtrum (T -> F) of traces
#  -> SUPHASEVEL - Multi-mode PHASE VELocity dispersion map computed from shots
#
# AUTHOR:
#
# Erik Larsen
# Institute of Physics and Technology
# University of Bergen
# Allegt. 55
# N-5007 Bergen, Norway
# EMAIL: Erik.L@uib.no
# August-November 2020
#
# Special thanks to Senior Engineer Bent Ole Rud at Department of Earth Science, University of Bergen, for introducing me
# to this open source seismic utilities package, Seismic Unix.
#
#=============================================================================
#
#-----------------------------------------------------------------------------
#            DEFINE INPUT DATA
#-----------------------------------------------------------------------------

segyfile=svea_2018_ag_3c.segy   # Name of SEGY file containing measurement data
shot=138             # choose shot number to process and plot
filt=1,2,20,40       # frequency filter coeff.: Ormsby bandpass filter
tmax=6               # max time to be plotted
fmax=30.5            # max freq. to be plotted
tpower=1             # tpow in gain control
labelsized=20        # Labelsize (default=18)

title="Shot: $shot dx = 12.5 m, 3C - vertical particle velocity" # title heading output files

#-----------------------------------------------------------------------------
#            SEISMOGRAM (X-T DOMAIN) PLOT
#-----------------------------------------------------------------------------
# NAME postscript output file for seismogram
psfileW3c=out_svea_2018_ag_3c_seis_shot_$shot.ps

# READ data from SEGY file
segyread tape=$segyfile |    # read SEGY file
suwind key=ep min=$shot max=$shot | # read shot point numbers
suwind key=tracf j=3 s=1 |   # read trace number within original field record, j:
```

```
77 #                              pass every j-th trace, s: pass every j-th trace
78 #                              based at s (note: because of the channel setup)
79 suwind count=30 tmax=$tmax | # 'count': max value of key header word (=offset) to
80 #                              pass up to count traces (= 30)
81 # PROCESSING
82 sugain tpow=$tpower |    # gain control: multiply data by t^tpow
83 sufilter f=$filt |       # applies a zero-phase, sine-squared tapered filter: Ormsby BP
       filter
84 sugain pbal=1 |          # flag; 1 = bal traces by dividing by rms value
85 suabshw key=offset |     # replace header key word by its absolute value
86
87 # PLOTTING
88 suwind key=offset min=0 max=365 | # define window length for offset
89 supswigp key=offset perc=99.5 d2num=50 verbose=1 n1tic=2 n2tic=2 label1="Time (s)"
      label2="Offset (m)" title="$title" > $psfileW3c      # PostScript WIGgle plot of a
       SEGY data set, printed as a PostScript file formatted ".ps"
90
91 #-------------------------------------------------------------------------------
92 #               F-K (FREQUENCY-WAVENUMBER DOMAIN) SPECTRUM
93 #-------------------------------------------------------------------------------
94 # NAME postscript output file for F-K spectrum
95 psfileFK3C=out_svea_2018_ag_3c_fk_shot_$shot.ps
96
97 # color smoothing factors
98 d1sFK=0.250  # 0.25 factor by which to scale d1 (sampling interval in 1st (fast)
      dimension) before imaging
99 d2sFK=0.125  # 0.125 factor by which to scale d2 (sampling interval in 2nd (slow)
      dimension) before imaging
100
101 # READ data from SEGY file
102 segyread tape=$segyfile |    # read SEGY file
103 suwind key=ep min=$shot max=$shot | # read shot point numbers
104 suwind key=tracf j=3 s=1 |   # read trace number within original field record, j:
105 #                              pass every j-th trace, s: pass every j-th trace
106 #                              based at s (note: because of the channel setup)
107 suwind count=30 tmax=$tmax | # 'count': max value of key header word (=offset) to
108 #                              pass up to count traces (= 30)
109 # PROCESSING
110 sugain tpow=$tpower |    # gain control: multiply data by t^tpow
111 sufilter f=$filt |       # applies a zero-phase, sine-squared tapered filter: Ormsby BP
       filter
112 sugain pbal=1 |          # flag; 1 = bal traces by dividing by rms value
113 suabshw key=offset |     # replace header key word by its absolute value
114 suspecfk dx=12.5 verbose=1 |        # dx: spatial sampling interval
115
116 # IMAGING
117 suwind tmax=$fmax |                 # max frequency to plot
118 # Define color map - HLS definitions (H: hue, L:Luminance, S:Saturation) for better
```

```
# intermediate color interpolation. Example of definitions:
#       bhls=0.666666,.5,1: blue, ghls=0.333333,.5,1: green, whls=0,.5,1: red
supsimage style=seismic d1s=$d1sFK d2s=$d2sFK x1beg=0 x1end=$fmax d1num=5 n1tic=5
    n2tic=4 bps=24 bhls=0,0.5,1 ghls=0.5,0.5,1 whls=0.66666,0.15,1 perc=99.5 verbose=1
     legend=1 lnice=1 units="|Amplitude|" title="F-K $title" label1="Frequency (Hz)"
    label2="Wavenumber (1/m)" labelsize=$labelsized > $psfileFK3C   # PostScript image
     of a segy data set, printed at a PostScript file formatted ".ps"  - 3C

#-------------------------------------------------------------------------------
#           F-V (PHASE VELOCITY) SPECTRUM
#-------------------------------------------------------------------------------
# NAME postscript output file for F-V spectrum
psfilePH3c=out_svea_2018_ag_3c_PhaseVel_shot_$shot.ps
# Resolution limit file for spatial aliasing
spat_alias_AG_3C=AG_3C_spatial_aliasing_coord.asc

d1sFV=0.250 # factor by which to scale d1 (sampling interval in 1st (fast) dimension)
    before imaging
d2sFV=0.125 # factor by which to scale d2 (sampling interval in 2nd (slow) dimension)
    before imaging

# READ data from SEGY file
segyread tape=$segyfile |    # read SEGY file
suwind key=ep min=$shot max=$shot | # read shot point numbers
suwind key=tracf j=3 s=1 |   # read trace number within original field record, j:
#                              pass every j-th trace, s: pass every j-th trace
#                              based at s (note: because of the channel setup)
suwind count=30 tmax=$tmax | # 'count': max value of key header word (=offset) to
#                              pass up to count traces (= 30)
# PROCESSING
sugain tpow=$tpower |   # gain control: multiply data by t^tpow
sufilter f=$filt |      # applies a zero-phase, sine-squared tapered filter: Ormsby BP
     filter
sugain pbal=1 |         # flag; 1 = bal traces by dividing by rms value
suabshw key=offset |    # replace header key word by its absolute value
suphasevel fv=0 nv=500 dv=1 fmax=$fmax norm=0 | # Multi-mode PHASE VELocity dispersion
#       map computed from shot record(s), fv: min phase velocity (m/s), nv: number of
#       phase velocities, dv: phase velocity step (m/s), fmax: maximum frequency in
#       process (Hz), norm: normalize amplitude spectrum
suamp | # output amp, phase, real or imag trace from (frequency, x) domain data

# IMAGING
# Define color map - HLS definitions (H: hue, L:Luminance, S:Saturation) for better
# intermediate color interpolation. Example of definitions:
#       bhls=0.666666,.5,1: blue, ghls=0.333333,.5,1: green, whls=0,.5,1: red
supsimage style=normal d1s=$d1sFV d2s=$d2sFV x1beg=0 x1end=$fmax n1tic=5 n2tic=5 d2num
    =100 d1num=5 perc=99.5 curve=$spat_alias_AG_3C curvewidth=2 curvecolor=white npair
    =2 curvedash=4 label1="Frequency (Hz)" label2="Phase velocity (m/s)" bps=24 bhls
```

```
    =0,0.5,1 ghls=0.5,0.5,1 whls=0.66666,0.15,1 hbox=600 wbox=900 legend=1 lnice=1
    units="|Amplitude|" title="F-V $title" labelsize=$labelsized > $psfilePH3c #
    PostScript image of a segy data set, printes at a PostScript file formatted ".ps"
158
159 #-------------------------------------------------------------------------------
160 #                    F-V (FREQUENCY-PHASE VELOCITY) SPECTRUM
161 #-------------------------------------------------------------------------------
162 # NAME PostScript file for normalized F-V spectrum
163 psfilePH3c_norm=out_svea_2018_ag_3c_PhaseVel_norm_shot_$shot.ps
164 # Resolution limit file for spatial aliasing
165 spat_alias_AG_3C=AG_3C_spatial_aliasing_coord.asc
166
167 d1sFV=0.250 # factor by which to scale d1 (sampling interval in 1st (fast) dimension)
    before imaging
168 d2sFV=0.125 # factor by which to scale d2 (sampling interval in 2nd (slow) dimension)
    before imaging
169
170 # READ data from SEGY file
171 segyread tape=$segyfile |    # read SEGY file
172 suwind key=ep min=$shot max=$shot | # read shot point numbers
173 suwind key=tracf j=3 s=1 |   # read trace number within original field record, j:
174 #                              pass every j-th trace, s: pass every j-th trace
175 #                              based at s (note: because of the channel setup)
176 suwind count=30 tmax=$tmax | # 'count': max value of key header word (=offset) to
177 #                              pass up to count traces (= 30)
178 # PROCESSING
179 sugain tpow=$tpower |   # gain control: multiply data by t^tpow
180 sufilter f=$filt |      # applies a zero-phase, sine-squared tapered filter: Ormsby BP
     filter
181 sugain pbal=1 |         # flag; 1 = bal traces by dividing by rms value
182 suabshw key=offset |    # replace header key word by its absolute value
183 suphasevel fv=0 nv=500 dv=1 fmax=$fmax norm=1 | # Multi-mode PHASE VELocity dispersion
184 #       map computed from shot record(s), fv: min phase velocity (m/s), nv: number of
185 #       phase velocities, dv: phase velocity step (m/s), fmax: maximum frequency in
186 #       process (Hz), norm: normalize amplitude spectrum
187 suamp | # output amp, phase, real or imag trace from (frequency, x) domain data
188
189 # IMAGING
190 # Define color map - HLS definitions (H: hue, L:Luminance, S:Saturation) for better
191 # intermediate color interpolation. Example of definitions:
192 #       bhls=0.666666,.5,1: blue, ghls=0.333333,.5,1: green, whls=0,.5,1: red
193 supsimage style=normal d1s=$d1sFV d2s=$d2sFV x1beg=0 x1end=$fmax n1tic=5 d1num=5 d2num
    =100 n2tic=5 perc=99.5 curve=$spat_alias_AG_3C curvewidth=2 curvecolor=white npair
    =2 curvedash=4 label1="Frequency (Hz)" label2="Phase velocity (m/s)" bps=24 bhls
    =0,0.5,1 ghls=0.5,0.5,1 whls=0.66666,0.15,1 hbox=600 wbox=900 legend=1 lnice=1
    units="|Normalized amplitude|" title="F-V $title" labelsize=$labelsized >
    $psfilePH3c_norm     # PostScript image of a segy data set, printes at a
    PostScript file formatted ".ps"
```

```
194
195 #-------------------------------------------------------------------------------
196 #               END OF SCRIPT
197 #-------------------------------------------------------------------------------
198 exit                # THIS MUST BE THE LAST COMMAND
```

Appendix L

C-shell, Shell and MATLAB scripts

The following is a list of the Shell and C Shell scripts written specifically for this thesis:

'run_dem_ERIK.sh' - Script for running the DEM model with '.inp' formatted input files.

'run_model.csh' - Run OASES with different '.dat'-fomatted input files (i.e. environment models)

plot_seis.sh - Process and plot shot gathers, $f-k$ and $f-v$ spectra from '.su'-formatted input files from OASES for reproducing the result in [1, figure 8].

'plot_seis_OASES_shot_183.sh' - Process and plot shot gather, $f-k$ and $f-v$ spectra from '.su'-formatted input files from OASES for AG2 OBN hydrophone and vertical component receivers.

'plot_seis_OASES_shot_138.sh - Process and plot shot gather, $f-k$ and $f-v$ spectra from '.su'-formatted input files from OASES for AG 3C vertical component receivers.

'plot_shot_obn_ag2_hydro.sh' - Process and plot shot gather, $f-k$ and $f-v$ spectra from SEG-Y formatted input files for the AG2 OBN hydrophone Svea 2018 dataset

'plot_shot_obn_ag2_vertC.sh' - Process and plot shot gather, $f-k$ and $f-v$ spectra from SEG-Y formatted input files for the AG2 OBN vertical component Svea 2018 dataset

plot_shot_ag_3c.sh - Process and plot shot gather, $f-k$ and $f-v$ spectra from SEG-Y formatted input files for the AG 3C vertical component Svea 2018 dataset

The following is a list of the MATLAB scripts written specifically for this thesis:

'plot_DEM_clay_water.m' - Plotting the macro elastic properties for clay-water mix with different aspect ratios.

'plot_DEM_quartz_water.m' - Plotting the macro elastic properties for quartz-water mix with different aspect ratios.

'plot_DEM_quartzClay_Han_water_phys_prop.m' - Plotting the macro elastic properties for quartz with clay (Han)-water mix with different aspect ratios.

'plot_DEM_silt_water.m' - Plotting the macro elastic properties for silt-water mix with different aspect ratios.

'plot_DEM_quartzClay_Han_water_silt_rat_1_0_phys_prop.m' - Plotting the macro elastic properties for quartz with clay (Han) with water-silt ($\alpha_{silt} = 1$) mix with constant water aspect ratio and different initial porosities.

'plot_DEM_quartzClay_Han_water_silt_rat_1_0_vs.m' - Plotting the macro shear velocities for quartz with clay (Han) with water-silt ($\alpha_{silt} = 1$) mix with constant water aspect ratio and different initial porosities.

Note that some of these MATLAB scripts call upon functions from downloadable packages, such as 'labelpoints.m' and 'NewCallback.m', found at GitHubs.

Any reader interested in obtaining these programs is welcome to send an e-mail to

Erik.L@uib.no or eriklarsen4@hotmail.com.